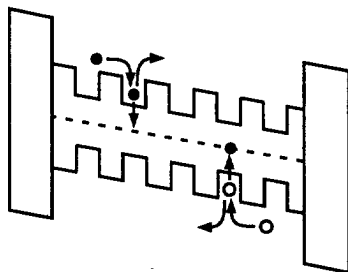


Fourier Optics and Optical Diagnostics Laboratory

Transport Modeling of Multiple-Quantum-Well Optically Addressed Spatial Light Modulators

A Dissertation Submitted to the
Department of Physics
Stanford University



Stephen Lee Smith

December 1996

19981030 046

DISTRIBUTION STATEMENT A

Approved for public release;
Distribution Unlimited

BTIC QUALITY INSPECTED 4

Transport Modeling of Multiple-Quantum-Well Optically Addressed Spatial Light Modulators

A DISSERTATION
SUBMITTED TO THE DEPARTMENT OF PHYSICS
AND THE COMMITTEE ON GRADUATE STUDIES
OF STANFORD UNIVERSITY
IN PARTIAL FULFILLMENT OF THE REQUIREMENTS
FOR THE DEGREE OF
DOCTOR OF PHILOSOPHY

Stephen Lee Smith

December 1996

© Copyright by Stephen Lee Smith 1996
All Rights Reserved

I certify that I have read this dissertation and that in my opinion it is fully adequate, in scope and quality, as a dissertation for the degree of Doctor of Philosophy.



Lambertus Hesselink (Principal Adviser)

I certify that I have read this dissertation and that in my opinion it is fully adequate, in scope and quality, as a dissertation for the degree of Doctor of Philosophy.



Steven Chu

I certify that I have read this dissertation and that in my opinion it is fully adequate, in scope and quality, as a dissertation for the degree of Doctor of Philosophy.



Martin Fejer

Approved for the University Committee on Graduate Studies:

Abstract

Optically addressed spatial light modulators are essential elements in any optical processing system. Applications such as optical image correlation, short pulse auto-correlation, and gated holography require high speed, high resolution devices for use in compact, high throughput systems. Other important device criteria include ease of fabrication and operation. In this work we study the transport dynamics of a new kind of optically addressed spatial light modulator that uses semi-insulating or intrinsic quantum-well material to produce high performance devices without the need for pixellation or complicated device design.

In response to an incident intensity pattern, basic device operation occurs through the screening of an applied voltage via the optical generation, transport, and trapping of photocarriers. A field pattern which mimics the incident intensity pattern is produced by the screening process. This generates strong index and absorption holograms via the quantum confined Stark effect. These holograms can be read out simultaneously with a probe beam to provide dynamic read/write operation.

Overall device performance is determined by the transport of photocarriers during the field screening process. We have developed a transient, two-dimensional drift-diffusion model to describe both free and well-confined carrier transport as well as nonlinear effects such as velocity saturation and field-dependent carrier emission from quantum wells. Various analytical and numerical results for the internal carrier and space charge distributions, different screening regimes, and relative carrier contributions to the screening process are given. An experimental characterization of a GaAs/AlGaAs device using optical

transmission and photocurrent techniques is also presented and used to verify the main results of the transport model.

Analytical and numerical analyses of various transport effects that limit the resolution are also given. We show that, contrary to the results of earlier device models, both the speed response and resolution can be simultaneously optimized using appropriate device design. Using realistic device parameters, frame rates of 100 kHz at 10 mW/cm² intensity with 7 μm device resolution are predicted.

Acknowledgments

First, I would like to thank my advisor, Bert Hesselink, for his support and encouragement over these past several years. He gave me a great deal of freedom not only in choosing this topic, but in determining the course of research. He has allowed me to pursue a number of interests, both directly and not so directly, related to this project. It is an opportunity that I have greatly appreciated. I would also like to thank two researchers from AT&T Bell Laboratories who have been of great help: William Coughran who got me started on semiconductor device modeling, and Afshin Partovi who fabricated and generously provided the samples used in our experiments.

One of the great things about being in a group as large as ours is that there are always interesting and useful people around. I would especially like to thank Jeff Wilde who first showed me around the lab during my first year in the group, and Lew Aronson who pointed me towards this project. I would also like to thank Elizabeth Downing for her aid in getting a Ti:S laser system up and running. As this research involved intensive computer simulations, it would not have been possible without the help of the following very generous and very good computer people: Jim Helman, Paul Ning, Mark Peercy, Thierry Delmarcelle, Yuval Levy, and Raj Batra. I would also like to thank some of my lab and office mates for their friendship and good conversations over the years, especially Muthu Jeganathan, John "Q-function" Heanue, and Raymond DeVre. Special thanks goes to our group secretary, Lilyan Sequeria, for her great efficiency and friendly dealings as she battled the Stanford paperwork jungle.

Finally, I would like to thank my family for their support and encouragement of my work and interest in science- not only here at Stanford, but all during secondary school, through the science fair projects, and at Florida. I would also like to thank my Swedish clan for their support and sometimes overly zealous, but very much appreciated, interest in my work.

Last (but really first!), I would like to thank my wife Monica who has been extremely supportive, and who has graciously put up with too many late nights and too many absent Sundays.

This research has been partially supported by the Office of Naval Research, and the Advanced Research Projects Agency through the CNOM program.

Contents

Abstract	iv
Acknowledgments	vi
List of Tables	xii
List of Figures	xiii
1 Introduction	1
1.1 Background on the MQW-OASLM2
1.2 Thesis Overview4
2 Optically Addressed Spatial Light Modulators	6
2.1 Basic Device Designs7
2.1.1 Photoconductive/Electro-optic Devices7
2.1.2 PROM8
2.1.3 Quantum-Well Modulators9
2.2 MQW-OASLM11
2.3 Diffraction13
2.3.1 Raman-Nath Diffraction14
2.3.2 Holography16
2.4 Application Example: Optical Correlator18
2.5 Performance Comparison21

2.6	Summary	22
3	Optical and Transport Properties of Multiple-Quantum-Wells	25
3.1	Electronic Structure	26
3.2	Optical Properties	30
3.2.1	Excitons	30
3.2.2	Quantum Confined Stark Effect	32
3.2.3	Electro-optic Effect	34
3.3	Transport Properties	35
3.3.1	Vertical vs. In-plane	35
3.3.2	Escape Mechanisms	37
3.3.3	Shallow Trap Model	41
3.4	Summary	43
4	Electric Field Screening	44
4.1	Device Model	45
4.2	Carrier Distributions	49
4.3	Injection Model	53
4.4	Field Screening	54
4.4.1	Short Drift Lengths	55
4.4.2	Long Drift Lengths	56
4.4.3	Initial Rate	58
4.5	Numerical Results	59
4.6	Semiconductor and Quantum-Well Effects	61
4.7	Summary	65
5	Transmission and Photocurrent Response	66
5.1	Experiment	67
5.1.1	Setup	68
5.1.2	Transmission Results	70

5.1.3	Photocurrent Results	73
5.2	Simulation	75
5.2.1	Device Model	75
5.2.2	Field Screening Results	77
5.2.3	Photocurrent Results	78
5.3	Summary	83
5.4	Appendix	83
6	Grating Formation	86
6.1	Device Model	87
6.2	Small Signal Injection Model	90
6.2.1	Electrostatics	91
6.2.2	Carrier Distributions	93
6.2.3	Grating Formation	96
6.3	Numerical Results	99
6.3.1	Field Uniformity	99
6.3.2	Intensity Modulation Dependence	100
6.3.3	Transverse Transport	103
6.4	Summary	104
7	Resolution Performance	106
7.1	Transverse Transport	107
7.1.1	Interior Transport	108
7.1.2	Surface Transport	112
7.1.3	Resolution Estimates	113
7.1.4	Intensity Modulation Dependence	113
7.2	Semiconductor and Quantum-Well Effects	115
7.3	Optimization Example	117
7.4	Summary	120

8	Conclusions	122
8.1	Summary of Contributions	122
8.2	Suggestions for Future Research	124
A	Numerical Methods	126
B	Publications	131
	Bibliography	132

List of Tables

2-1	OASLM performance parameters.	22
4-1	Device parameters for 1D simulations	59
4-2	Velocity saturation model.	62
5-1	Simulation parameters for comparison with experiments	76
7-1	Estimated resolution limits	114
7-2	Optimization parameters	117

List of Figures

1-1	Device technology leading to the MQW-OASLM	2
2-1	Photoconductive/electro-optic modulator design	8
2-2	Pockels readout optical modulator design	9
2-3	Quantum-well modulators	10
2-4	MQW-OASLM design	12
2-5	AT&T device structure	13
2-6	Raman-Nath diffraction	14
2-7	Holography in a MQW-OASLM	17
2-8	Optical correlator	19
2-9	OASLM bit rate and intensity comparison	23
3-1	Band diagram of GaAs	27
3-2	Quantum-well band edges.	28
3-3	Quantum-well subbands.	29
3-4	Absorption spectrum of a GaAs/AlGaAs MQW device	31
3-5	Quantum confined Stark effect	33
3-6	The electro-optic effect produced by the QCSE	34
3-7	Vertical and in-plane quantum-well transport	36
3-8	Thermionic and tunneling escape from a quantum well	37
3-9	Escape rates for electrons and holes	40
3-10	Shallow trap model for quantum wells	42

4-1	1D device geometry	46
4-2	Quasi-steady state carrier distributions	52
4-3	Injection model of screening	53
4-4	Screening of the internal field.	57
4-5	Initial screening rate.	58
4-6	Interior field distribution	60
4-7	Comparison of the injection model and full numerical solutions.	61
4-8	Field screening for constant and velocity-saturated mobilities	63
5-1	Experimental setup for measuring transmission and photocurrent	69
5-2	QCSE transmission	71
5-3	Measured screening of the electric field	72
5-4	Measured photocurrent for various applied voltages	74
5-5	Measured photocurrent for both polarities	75
5-6	Simulated field screening using constant mobilities	78
5-7	Simulated photocurrent using constant mobilities	79
5-8	Simulated photocurrent for both polarities using constant mobilities	80
5-9	Simulated photocurrent using velocity-saturated mobilities	81
5-10	Simulated photocurrent for both polarities using velocity-saturated mobilities	82
5-11	Amplifier schematics	84
6-1	2D device geometry	88
6-2	Grating formation	90
6-3	Dynamics of the first-order field component	98
6-4	Interior distribution of the first-order field component..	100
6-5	Grating dependence on the intensity modulation	101
6-6	Geometric and nominal resolution curves	104
7-1	Resolution limit imposed by transverse interior diffusion	110
7-2	Resolution limit imposed by transverse interior drift.	111

7-3	Resolution limit imposed by transverse surface diffusion and drift	112
7-4	Resolution dependence on the intensity modulation	115
7-5	Optimized and non-optimized resolution curves	119
7-6	Resolution limits for various transport mechanisms	120
A-1	Simulation grid	127
A-2	Adaptive time step control	129

Chapter 1

Introduction

Optical processing systems combine the inherent parallelism of optics with the square-law intensity response of optically addressed spatial light modulators to perform high speed, page-based computations. Applications include optical image correlation [1], short pulse auto-correlation [2], and gated holography [3]. Compact, high speed systems require optically addressed spatial light modulators with high spatial resolution and fast frame rates. Many devices, such as the Pockels Readout Optical Modulator (PROM) [4] and the liquid crystal light valve [5], have been developed over the years. However, none of these devices has simultaneously demonstrated the following requirements that are needed in most applications: high speed, high resolution, gray scale response, low power operation, low applied voltage, convenient operating wavelength, and easy fabrication.

The insulator/multiple-quantum-well/insulator devices first developed at AT&T Bell Laboratories in 1991 have the potential to meet many of these requirements [6]. These devices are commonly referred to as multiple quantum well optically addressed spatial light modulators (**MQW-OASLM**) or Stark-geometry photorefractive quantum well devices. They combine the fast carrier transport and large electro-optic response of quantum wells with a thin, layered structure to produce many of the properties described above. The optimization of both the speed and resolution performance, however, has been hampered by a lack of understanding of the details of device operation, and, specifically, the

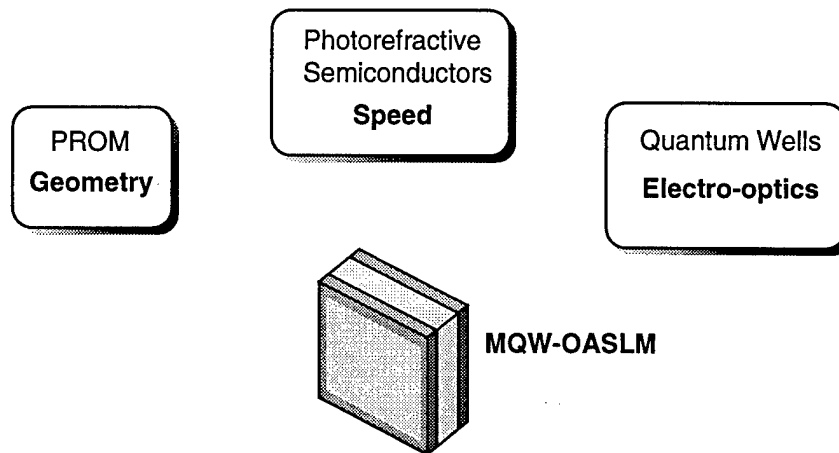


Figure 1-1 Three device technologies led to the development of the MQW-OASLM. The sandwich style geometry was taken from the PROM. The use of semiconductor material to obtain fast photoconductive response rates was taken from photorefractive research. Large, resonant electro-optic effects are obtained by using semiconductor quantum wells. The sketch of the device structure shows the interior photoconductive layer surrounded by insulating layers and transparent electrodes.

role of the quantum wells. Addressing these issues is one of the main motivations for this work.

1.1 Background on the MQW-OASLM

As diagrammed in Fig. 1-1, the development of the multiple-quantum-well optically addressed spatial light modulator originated from three different device technologies over three decades. The basic device structure was taken from the PROM, one of the first optically addressed spatial light modulators developed in the 1970's [4]. This device uses a photorefractive crystal of bismuth-silicon-oxide (BSO) sandwiched between two insulating parylene layers. The BSO layer acts both as a photoconductor and as an electro-optic modulator. A uniform voltage is applied by transparent electrodes. Device operation proceeds via the transport of photogenerated carriers created by a writing intensity pattern. The trapping of photogenerated carriers in midgap traps produces a space charge that screens the applied voltage in a pattern that mimics the writing image. Subsequent

electro-optic modulation by the linear Pockels effect creates a corresponding phase pattern that can be read out with another optical beam.

A number of device models were developed to analyze the resolution performance of various assumed space-charge distributions, and some simple transport models were even constructed [7-10]. The overall device performance was fairly modest, and the applied voltage requirements were quite high, ~ 1 kV. The advent of liquid crystal devices in the early 1980's with equivalent frame rates and much lower voltage requirements quickly doomed the PROM.

Some of the performance limitations of the PROM arose from the use of a thick (~ 300 μm) oxide photorefractive material. This thickness was required to produce significant phase modulation from the relatively weak linear electro-optic effect. The long device length combined with the inherently poor transport properties of oxide materials to produce slow response rates. In addition, the electrostatics of the extended space charge limited the resolution to a poor ~ 10 lp/mm, and convenient, IR wavelengths could not be used.

In the 1980's, work began on using resonant electro-optic effects in bulk semiconducting photorefractives as a way of combining a stronger electro-optic effect with the fast transport properties of semiconductors [11]. This work was primarily aimed at improving photorefractive phase conjugators, but it soon became apparent that large, resonant electro-optic effects could be used to replace the relatively weak Pockels effect in semiconductors for various types of photorefractive applications. Device operation was also compatible with diode lasers.

Around the same time, independent developments were being made in using quantum-well structures as electro-optic modulators [12]. By 1985, Miller *et al.* at AT&T Bell Laboratories established the quantum confined Stark effect as a very effective, although quadratic, electro-optic effect [13]. To take advantage of this electro-optic effect, however, the electric field had to be applied perpendicular to the layers- exactly the same geometry as in the PROM. In 1991, Partovi *et al.* revived the PROM geometry and began using multiple-quantum-wells as the active photoconductive and electro-optic layer [6]. Due to the very

large index of refraction and absorption changes produced by the quantum confined Stark effect, large phase and amplitude modulation can be produced in thin ($\sim 2 \mu\text{m}$) quantum-well layers. This allows the construction of very compact structures that offer low voltage operation and suppressed electrostatic limitations on the resolution. In fact, in the MQW-OASLM the two fundamental aspects of device performance, speed and resolution, are determined primarily by carrier transport during the screening of the applied field.

Since the initial demonstration of a MQW-OASLM in 1991, only a handful of device models have been developed to describe basic device operation and simple image formation [14, 15, 16]. Typically, ad hoc or highly restrictive assumptions are invoked to allow simple analytical or numerical solutions. At a minimum, a two-dimensional, transient device model that is capable of handling highly nonlinear and dynamic carrier transport is required. To date, no such model has been presented. In addition, no model has explicitly considered bipolar transport or the role of quantum wells in determining the resolution and speed performance.

1.2 Thesis Overview

The bulk of this thesis involves the development, solution, and understanding of a complete, two-dimensional device model to describe device operation and establish the performance limits of a MQW-OASLM. Before addressing these topics directly, however, we begin in Chapter 2 with a general description of optically addressed spatial light modulators including examples of different types of devices and applications. A comparison of the performance of various photoconductive OASLM's indicates that the MQW-OASLM has the potential to have the best combination of speed and resolution performance within its class. One of the reasons for this success is the very large, resonant electro-optic effect produced by quantum confinement in the quantum wells. This effect, known as the quantum confined Stark effect, is reviewed in Chapter 3. Carrier transport in quantum wells is also discussed, and a shallow trap model that allows the inclusion of quantum wells in standard semiconductor transport models is presented.

The discussion of carrier transport modeling begins in Chapter 4 where a drift-diffusion model is developed to describe device operation under uniform illumination. This one-dimensional device model is used to construct a detailed description of the screening process and to identify basic operating regimes. Techniques for optimizing the speed response are also given. Frame rates of 100 kHz at 10 mW/cm^2 intensity are predicted. The experimental characterization of a GaAs/AlGaAs device is then described in Chapter 5. Optical transmission and photocurrent measurements are used to probe the basic screening behavior under uniform illumination. The photocurrent measurement in particular is shown to provide a sensitive probe of the screening dynamics. A comparison of the measured screening behavior with the transport model developed in Chapter 4 shows very good agreement.

A simple case of image formation using sinusoidal gratings is then studied in Chapters 6 and 7 using a 2D device model which incorporates both free and quantum-well transport. The dynamics of grating formation, the role of vertical and transverse carrier transport in limiting the resolution, and some nonlinear transport effects in semiconductors and quantum wells are discussed. An optimization example which describes techniques to simultaneously optimize both the speed and resolution performance is also given. Device resolutions of $7 \text{ }\mu\text{m}$ are obtained using realistic device parameters while maintaining a 100 kHz frame rate at 10 mW/cm^2 intensity.

Chapter 2

Optically Addressed Spatial Light Modulators

The primary function of an optically addressed spatial light modulator (OASLM) is to convert an input image into a corresponding refractive index and absorption pattern. Subsequent readout by another optical beam transfers the optical modulation pattern onto the amplitude and phase of the readout beam. The square-law intensity response of most OASLM's, combined with optical readout, produces devices suitable for many optical processing applications such as optical correlation and spatial filtering. OASLM's can also replace standard film in general holographic systems.

The OASLM label is usually reserved for so-called dynamic devices. Unlike photographic film, these devices are reusable, and the optical modulation patterns develop in real time during the writing exposure. In this chapter, a few of the more widespread OASLM designs, as well as the basic design and operation of the device studied in this thesis, are described. A comparison of performance criteria such as speed, resolution, and sensitivity is made. In addition, a review of thin film diffraction is presented, and the operation of an optical correlator is described to highlight the impact of various OASLM performance characteristics on overall system performance.

2.1 Basic Device Designs

Many different types of OASLM's have been developed over the years using a variety of materials such as semiconductors [12], liquid crystals [5], polymers [17], proteins [18], and even atomic vapor [19]. A very good review of the most widely used designs can be found in Efron [20]. In this section, we describe some of the more widespread devices that operate similarly to the MQW-OASLM devices treated in this thesis. All of these devices are photoconductive in nature, relying on the transport of photogenerated carriers to modulate the voltage drop across an electro-optic region.

2.1.1 Photoconductive/Electro-optic Devices

One of the seminal devices in the OASLM field was the so-called Hughes liquid crystal light valve (LCLV) [5] which combined a cadmium sulfide (CdS) photosensor and a nematic liquid crystal. Its name derives from the gating effect on polarized light produced by nematic liquid crystals when switched between on and off states. It belongs to a general class of devices that incorporates a photoconductive layer for light sensitivity and a separate electro-optic layer for optical modulation. A cross-section of the basic design is shown in Fig. 2-1. The photoconductive and electro-optic layers are separated by a light blocking layer on the write side and a dielectric mirror on the readout side. An incident image on the write side is converted into a surface charge pattern near the edge of the photoconductor. This creates a spatially varying field pattern in the electro-optic region, which is typically either a liquid crystal or an electro-optic crystal. Readout of the resulting electro-optic pattern is performed from the read side in reflection off of the mirror. The use of nematic liquid crystals allows for low voltage operation with good contrast ratios. The switching time of nematic liquid crystals, however, can be relatively slow (~10 ms) which limits the frame rate.

Recent improvements have been made by replacing the photoconductor and/or the nematic liquid crystals with higher performance material. Armitage *et al.* demonstrated much faster response using ferroelectric liquid crystals, however, the response was limited

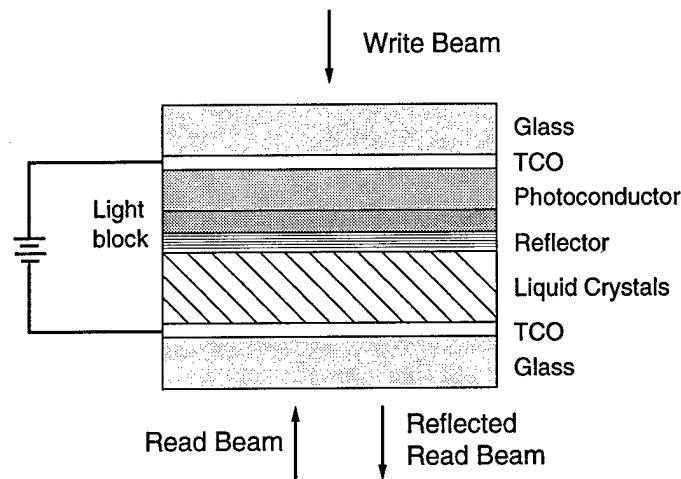


Figure 2-1 An example of a photoconductive/electro-optic modulator that uses liquid crystals as the modulating layer. The photoconductor and liquid crystals are separated by a light blocking layer and a reflector. This allows the writing and reading processes to be isolated from each other. Voltage is applied through transparent conducting oxide (TCO) electrodes.

to binary operation by the two-state switching of the ferroelectric liquid crystals [21]. Li *et al.* have demonstrated improved sensitivity and resolution performance by replacing the CdS photoconductor with amorphous hydrogenated silicon [22].

2.1.2 PROM

One of the first OASLM's to be developed was the Pockels Readout Optical Modulator or PROM [4]. In this device, the same layer acts as both the photoconductor and the electro-optic medium. Figure 2-2 shows the basic design which consists of an interior photorefractive crystal surrounded by insulating layers and transparent electrodes. Typical devices used $\sim 300 \mu\text{m}$ thick photorefractive bismuth silicon oxide, $\text{Bi}_{12}\text{SiO}_{20}$ (BSO), $5 \mu\text{m}$ thick insulating parylene layers, and indium tin oxide (ITO) transparent electrodes [23]. Device operation occurs through the application of a $\sim 1 \text{ kV}$ applied voltage and an incident intensity pattern. Photogenerated electrons in the light regions drift in the applied field toward the back electrode (holes are relatively immobile in BSO). The accumulation of carriers in midgap traps throughout the interior creates a space charge that screens the applied

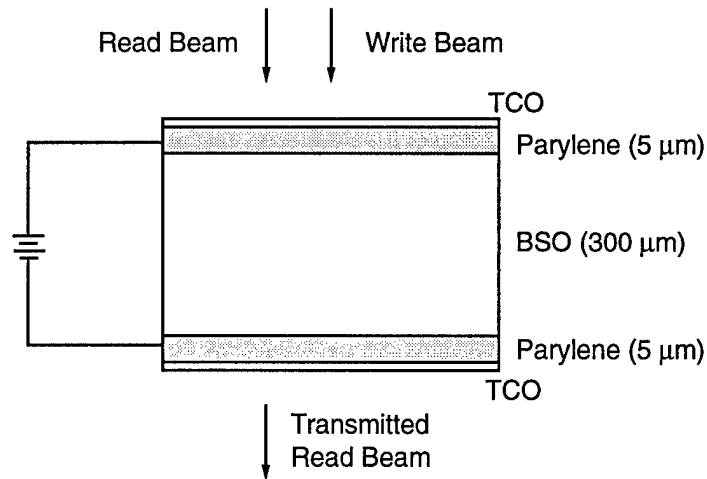


Figure 2-2 A Pockels Readout Optical Modulator (PROM) consisting of an interior BSO layer that acts as both a photoconductor and optical modulator. Insulating parylene layers isolate the BSO layer from the transparent conducting oxide (TCO) electrodes. Readout is in transmission.

voltage, producing a spatially varying voltage drop across the interior that mimics the input image. This voltage pattern then modulates the refractive index through the linear electro-optic effect, producing a phase pattern of the original input image.

One of the nice features of this design is that it is relatively simple, requiring only a few different layers and no photolithographically defined pixellation. The use of BSO, however, imposed several performance limitations. Due to the weak linear electro-optic effect, it was necessary to use a relatively thick BSO layer (300 μm). This created several problems, including large applied voltages (1 kV), long carrier transit times leading to low sensitivity (100 mW/cm²), and poor resolution (10 lp/mm) due to electrostatic effects of the extended bulk charge. The BSO devices were also not sensitive at convenient diode laser wavelengths. The PROM enjoyed about five years of serious interest, but essentially vanished after the development of the liquid crystal devices described above.

2.1.3 Quantum-Well Modulators

In an attempt to increase speed and provide IR sensitivity, several efforts have been made to use semiconducting multiple-quantum-well (MQW) materials as the photoconductive and electro-optic medium [20]. Quantum wells combine very good carrier transport

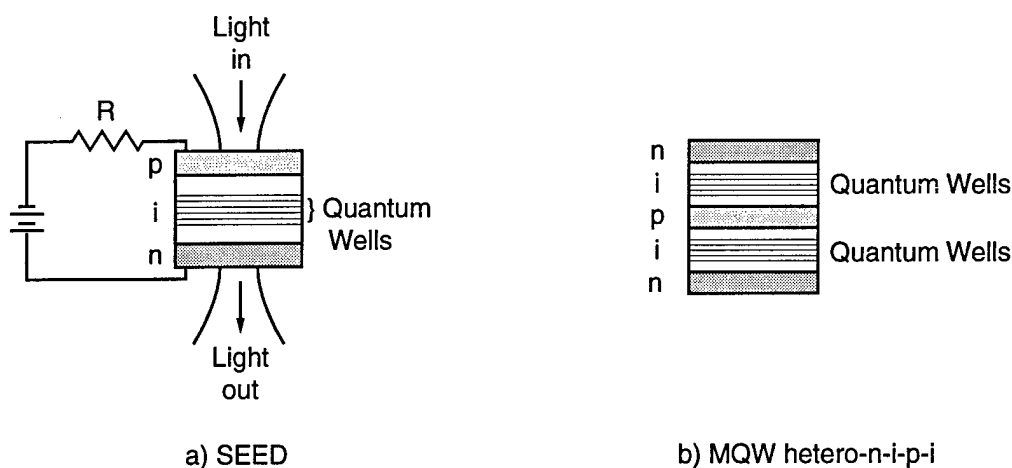


Figure 2-3 a) Self electro-optic effect device or SEED. The voltage drop across the quantum wells in the intrinsic region of a p-i-n diode is determined through feedback of the photocurrent generated by the diode. b) The basic structure of a multiple-quantum-well hetero-n-i-p-i device in which modulation doping is used to create back-to-back p-i-n devices throughout the device interior. Photoconductive screening of the built-in voltage modulates the voltage drop across the quantum wells.

properties with large, resonant electro-optic effects. We will review the optical and transport properties of quantum wells in detail in Chapter 3. While many device designs have been created, in this section we describe only two of the more popular and promising designs. These designs typically involve pixellated arrays of discrete modulators.

One of the first all-optical modulators developed using quantum wells was the self electro-optic effect device, or SEED, developed by Miller *et al.* at AT&T Bell Laboratories [12]. As shown in Fig. 2-3a, this device consists of a p-i-n diode structure in which the MQW's are placed in the intrinsic region. Biasing through a resistor allows for feedback during illumination as the voltage drop across the quantum-well region varies due to photoconduction. This voltage drop varies the transmission via a resonant electro-optic effect known as the quantum confined Stark effect [13] which produces very large changes in the absorption. Appropriate biasing and operating wavelengths can produce a gray scale response as well as binary, bistable behavior [24]. Arrays as large as 64x32 pixels have been fabricated and demonstrated to run at 100 MHz under 10 W/cm^2

intensity [25]. Running very large SEED arrays at very high frame rates may be difficult, however, due to large electrical power dissipation [20].

A somewhat different approach to modulator design using MQW's is shown in Fig. 2-3b. This structure uses modulation doping during growth of the quantum wells to achieve multiple periods of p-i-n regions throughout the interior. This device is known as a MQW hetero-n-i-p-i structure and operates through the screening of the built-in potential created by the modulation doping [26, 27]. The basic operating principle is somewhat similar to that of the PROM, except that screening is produced by free, not trapped carriers, and screening occurs across multiple p-i-n periods throughout the device interior [28]. This design offers much larger electro-optic effects at lower applied voltages due to the built-in voltage pattern. Although pixellation has been suggested to produce arrays [27], large arrays of pixellated devices have not yet been fabricated.

2.2 MQW-OASLM

The multiple-quantum-well optically addressed spatial light modulator (MQW-OASLM) devices analyzed in this thesis are in some sense hybrids of the PROM and MQW devices described above. They were first developed by Partovi *et al.* at AT&T Bell Laboratories in 1991 [6]. As shown in Fig. 2-4, the basic geometry is a PROM with the interior region made of a 2 μm thick MQW stack rather than a 300 μm BSO layer. Device operation is similar to that of the PROM, with the transport and trapping of photogenerated carriers. As we will show in later chapters, the collection of screening charge occurs primarily at the MQW-insulator interfaces. This is in contrast to the PROM device in which charge accumulates throughout the interior. In addition, carrier transport in semiconductors is bipolar.

Figure 2-4 illustrates the response of a MQW-OASLM to a simple intensity pattern consisting of light and dark fringes. Photogenerated carriers in the light regions are separated by the applied voltage and drift toward the semiconductor-insulator interfaces. For example, for positive applied voltage in Fig. 2-4, electrons are drawn to the top and holes to the bottom. Once the carriers reach the interfaces, they are stopped by the large bandgap

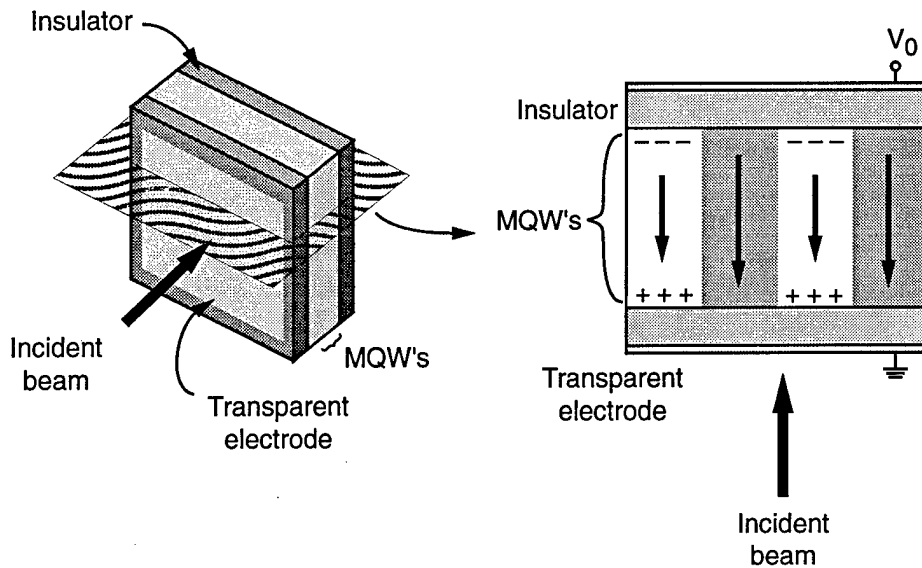


Figure 2-4 The sketch on the left shows the structure of a multiple-quantum-well optically addressed spatial light modulator (MQW-OASLM). A quantum-well region is sandwiched between two insulating layers and transparent electrodes. The indicated cross-section shown at the right resembles the PROM geometry. The response to a simple intensity pattern consisting of light and dark fringes is shown in the interior MQW region. Photocarriers in the light regions collect near the quantum well-insulator interfaces and screen the applied voltage. The resulting field pattern indicated by the arrows mimics the intensity pattern.

insulating layers and become trapped in midgap defect or impurity levels that are either intrinsic or engineered into the device. As this process continues, a screening charge develops in the light regions at the interfaces. In the dark regions, the screening process is slower. A surface charge pattern is thus created that mimics the intensity pattern. This surface charge screens the applied voltage, producing a field pattern that also mimics the intensity pattern. This field then modulates the index and absorption through the quantum confined Stark effect.

The use of MQW's combines the simple design of the PROM structure with the good carrier transport and electro-optic effects of quantum wells. Due to a strong electro-optic effect, thin MQW regions that give good diffraction efficiency ($\sim 1\%$) can be used, allowing low voltage operation (15 V) as well as improved resolution. In addition, these devices can be fabricated out of the same materials as laser diodes and thus provide a natural wavelength match.

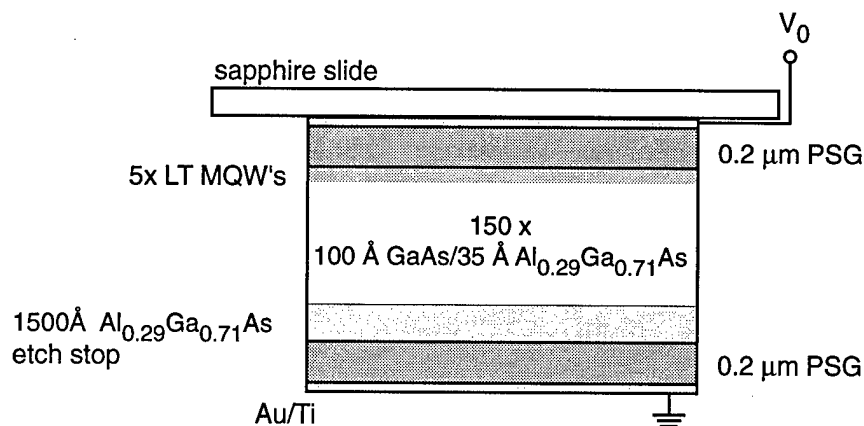


Figure 2-5 Sketch of an AT&T device used in our experiments. The interior consists of a 2 μm GaAs/AlGaAs quantum-well region surrounded by phosphate-silica-glass (PSG) insulating layers and gold semi-transparent electrodes.

The structure of an actual device is shown in Fig. 2-5. This device was fabricated by Bell Laboratories [29], and we have used it in our experiments discussed in Chapter 5. The MQW's consist of 100 \AA GaAs wells with 35 \AA Al_{0.29}Ga_{0.71}As barriers. A total of 155 periods were grown Cr-doped at 10^{16} cm^{-3} using molecular beam epitaxy (MBE). The last five quantum-well periods were grown at low temperature to induce defects and thereby improve resolution performance. The quantum wells were grown on top of a 1500 \AA Al_{0.29}Ga_{0.29}As etch stop which in turn was grown on a GaAs wafer. After MBE growth, 2000 \AA of phosphate-silica-glass (PSG) was evaporated on the top followed by the evaporation of 20 \AA Ti and 90 \AA Au to act as the transparent electrode. The device was then mounted top-down on a sapphire slide, and the GaAs substrate was removed using a selective etch. The evaporation steps were then repeated. Samples with apertures of 5 mm x 5 mm were produced.

2.3 Diffraction

As indicated above, the function of an OASLM is to convert a writing intensity pattern into a corresponding index and absorption pattern. In this section, we review the readout of such index and absorption patterns as would be produced by a MQW-OASLM device

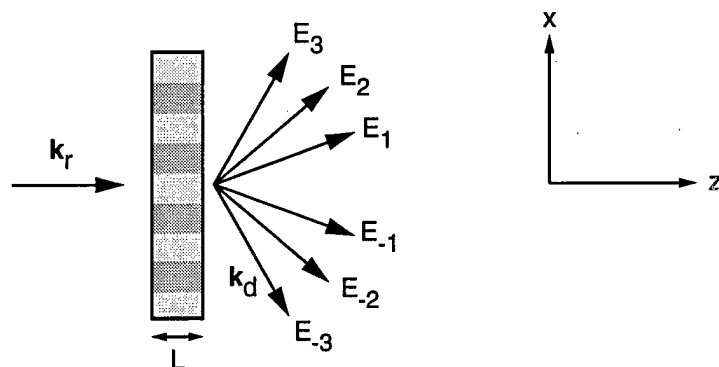


Figure 2-6 Raman-Nath diffraction from a thin hologram showing the many diffracted orders.

which is only a few microns in thickness. First, we consider the case of a thin, elementary sinusoidal grating which produces Raman-Nath diffraction. Standard holography is then considered, and the effects of the various grating formation steps on hologram fidelity are outlined.

2.3.1 Raman-Nath Diffraction

For simplicity, we first consider the diffraction from a polarization independent, sinusoidal grating. Diffraction from such a grating forms the basis of holography, and a sinusoidal intensity pattern is convenient for use in device simulations. Figure 2-6 diagrams the diffraction from a thin slab with thickness L and a mixed type of grating formed from both index and absorption modulation. The complex index of refraction is given by

$$n = n'_0 + \Delta n' \cos Kx \quad (2-1)$$

where $K = 2\pi/\Lambda$ is the magnitude of the grating vector, \mathbf{K} , which characterizes the orientation and frequency of the grating. The grating spacing, or period, is given by Λ , and the refractive index components are given by

$$n'_0 = n_0 + i\frac{\lambda}{4\pi}\alpha_0 \quad (2-2)$$

$$\Delta n' = \Delta n + i \frac{\lambda}{4\pi} \Delta \alpha \quad (2-3)$$

For $L \ll \Lambda$, the slab essentially acts as a complex amplitude transmission filter in which the transmission is given by [30]

$$T = e^{i(\delta_0 + \delta' \cos(Kx))} \quad (2-4)$$

where

$$\delta_0 = \frac{2\pi n'_0 L}{\lambda \cos \theta'} \quad (2-5)$$

and

$$\delta' = \frac{2\pi}{\lambda \cos \theta'} \int_0^L \Delta n'(z) dz \quad (2-6)$$

are the phase shifts, and where θ' is the incident angle inside the slab.

The readout of this grating by a plane wave with k -vector k_r , indicated in Fig. 2-6 produces the following field at the exit face of the slab

$$E_{out} = E_{read} e^{ik_r \cdot x} T = E_{read} e^{i\delta_0} e^{ik_r \cdot x} e^{i\delta' \cos(Kx)} \quad (2-7)$$

A Fourier decomposition of this field gives the far field diffraction pattern which consists of many diffracted beams traveling in directions given by $k_d = k_r + mK$ where m is the diffraction order. This type of diffraction is known as Raman-Nath diffraction, and the input diffraction efficiency in order m , which is the power diffracted into order m divided by the incident power of E_{read} , is given by [31]

$$\eta_m = e^{-\alpha_0 L} J_m^2(|\delta'|) \quad (2-8)$$

where J_m is the m^{th} order Bessel function. Typically, only the first-order diffracted beam is of interest and is given by

$$E_1 = E_{read} e^{i(k_r + K) \cdot x} T_1 \quad (2-9)$$

where T_1 is the transmission for the first-order diffracted beam. For $|\delta| \ll 1$, T_1 is given by

$$T_1 = iJ_1(-\delta) \approx -\frac{i\delta}{2} \quad (2-10)$$

Thus, for small phase shifts, the first-order diffraction is linear in the phase shift and hence linear in the index modulation.

2.3.2 Holography

Following Goodman [30], we now generalize the grating formation process to examine standard holography with an information carrying signal beam, S , and a plane wave reference beam, R , where

$$R = Ae^{ik_R \cdot x} \quad (2-11)$$

$$S = a(x, y)e^{i\varphi_a(x, y)}e^{ik_S \cdot x} \quad (2-12)$$

and $a(x, y)$ is the real amplitude of the image to be stored in the OASLM, and φ_a is the phase. The interference of these two beams inside the OASLM produces the following intensity pattern

$$I = (A^2 + a^2) \left(1 + \frac{2Aa}{A^2 + a^2} \cos(\mathbf{K} \cdot \mathbf{x} + \varphi_a) \right) \quad (2-13)$$

where $\mathbf{K} = \mathbf{k}_s - \mathbf{k}_r$ is the grating vector. For an image with a spatial frequency bandwidth much smaller than the magnitude of the grating vector, the intensity pattern consists of a rapidly varying carrier with spatial frequency $K/2\pi$ modulated by the slowly varying image. In order for the OASLM to faithfully reproduce the image beam upon diffraction, it must provide an amplitude transmission for the first order diffracted beam, T_1 , that has an amplitude that is linearly proportional to $a(x, y)$ and a phase given by φ_a . During the various steps of the grating formation processes, however, there are many nonlinear effects that can produce distortions in the transmission.

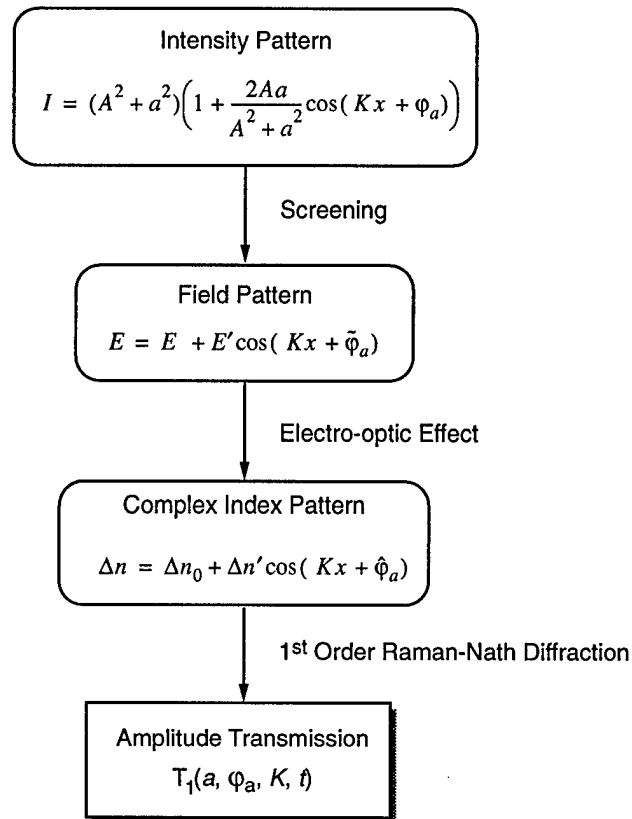


Figure 2-7 The steps that produce a hologram in a MQW-OASLM. An incident intensity pattern consisting of the interference between a plane wave reference and a signal beam drives the photoconductive screening process to produce a mimicing field pattern. Subsequent electro-optic modulation and diffraction lead to a first-order diffracted beam characterized by the first-order transmission. Nonlinear transport and electro-optic response as well as other effects can lead to distortions in the hologram fidelity. These distortions can arise in both the amplitude and phase of the field and index grating. The phase of the field and index gratings are denoted by $\tilde{\phi}_a$ and $\hat{\phi}_a$, respectively.

Figure 2-7 shows the sequence of grating formation steps for a photoconductive OASLM such as the MQW-OASLM. The first step involves the creation of the screening charge and subsequent field pattern by the photoconductive screening process. Due to carrier transport, this process is nonlinear, and the amplitude transmission can be distorted in two ways: higher order Fourier components of the screening field can be created, and the first-order field component can be distorted. Higher order gratings will diffract into higher

diffraction orders which are generally of no concern. Distortions of the first order field component, however, lead to distortions in the image in the first diffraction order.

The next step in the hologram formation process involves the creation of the index and absorption modulations from the field pattern. This step can also induce nonlinearities. For example, to lowest order the electro-optic effect in quantum wells is second order in the field; this can again lead to higher order Fourier components in the complex index pattern as well as distort the first-order amplitude. Finally, the field amplitude that is diffracted into the first order is, for large phase modulation, nonlinear in the index as given by Eq. (2-10). However, for small index modulation the response is linear in the index modulation.

The results of the above processes on the first-order transmission can be summarized by the functional dependence of the first-order transmission on the image amplitude a , the image phase ϕ_a , the grating vector K , and the time t

$$T_1 = T_1(a, \phi_a, K, t) \quad (2-14)$$

The dependence of T_1 on a and ϕ_a gives the linearity of the hologram formation process. The K dependence of T_1 is referred to as the Modulation Transfer Function (MTF) and characterizes the effect of the resolution performance of the OASLM on the image transfer process. The time dependence essentially gives the exposure dependence which may also affect the linearity. The response of some devices is linear for short exposures but then becomes nonlinear for long exposures. We will return to these issues in detail for the MQW-OASLM in the following chapters.

2.4 Application Example: Optical Correlator

There are many applications for dynamic OASLM's including optical processing and display [32]. Several applications using a MQW-OASLM have been demonstrated including a joint transform correlator [1], a short pulse auto-correlator [2], and a time-gated

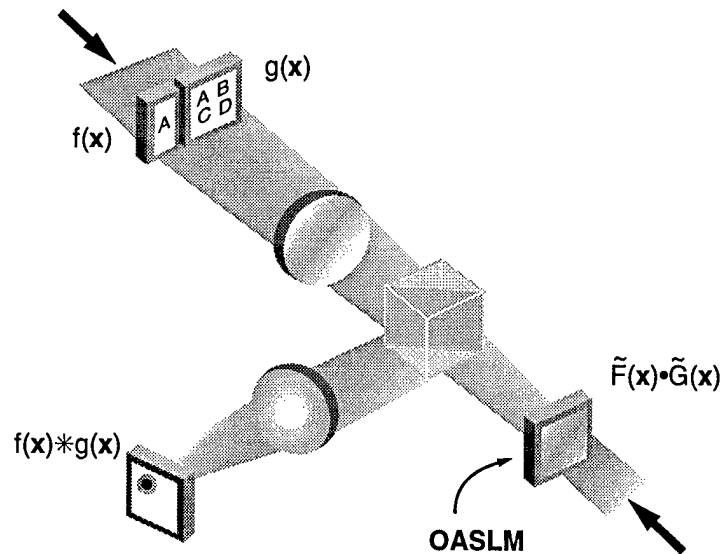


Figure 2-8 A joint transform optical correlator which computes in parallel and in real time the spatial correlation between two input images. The two images are Fourier transformed onto the OASLM, producing a hologram that is proportional to the product between the Fourier transforms. A back-illuminating beam then diffracts off of this hologram, reflects off of the beam splitter, and passes through another Fourier transforming lens onto the output plane. The indicated correlation peak shows the location of the “unknown” letter ‘A’ in the reference image.

holographic setup for imaging through turbid media [3]. In this section, the operating principle of a joint transform correlator is explained and used to motivate some of the more important performance criteria of the OASLM.

Figure 2-8 shows a diagram of a joint transform correlator. The function of the correlator is to compute in parallel and in real time the spatial correlation between the two input images and present the result on the output plane. This is accomplished by taking advantage of the Fourier transforming properties of lenses and of the square-law intensity response of the OASLM.

The two images to be compared, usually an unknown image and a reference image, are imprinted onto coherent beams using, perhaps, electrically addressed SLM’s. These beams are Fourier transformed onto the OASLM which is placed in the back focal plane of the first lens. The hologram formed by the interference between the two beams is proportional to the product of the Fourier transforms of the original images. This hologram can be read out by a beam from the back which is reflected by the beam splitter and passed through

another Fourier transforming lens onto the output plane, typically a CCD detector or a photodiode array. As indicated in Fig. 2-8, the resulting output intensity consists of a correlation peak corresponding to the position of the unknown letter 'A' in the reference image.

The overall performance of the system will in part be determined by the performance of the OASLM. For example, the signal-to-noise ratio achieved at the detector plane is determined by the diffraction efficiency of the OASLM. A larger diffraction efficiency increases the intensity in the correlation peak at the detector and improves the recognition accuracy. The number of comparisons per second will in part be determined by the frame rate of the OASLM. The faster the grating can be formed, erased, and reset, the faster the overall system can run. One of the advantages of using such an optical setup for this application is that, even if the system can only run at modest speeds by electrical standards, say 100 kHz, the effective computation rate can be quite high since a whole 2D page is processed at once. For a page with $N \times N$ pixels, the number of equivalent digital computations goes as $N^2 \log_2 N$, giving an equivalent computation rate of over 1 Tflop for 1000×1000 page sizes running at 100 kHz [20]. For this reason alone, interest in optical correlators has remained high since their introduction by Vander Lugt in 1964 [33].

Another very important practical consideration is the compactness of the optical setup. In the Fourier geometry used here, the required focal lengths of the lenses are determined by the size of the input images and by the resolution of the OASLM. With Λ_{res} denoting the smallest spatial feature than can be resolved by the OALSMS, the required focal lengths are given by

$$f = \frac{D_{image} \Lambda_{res}}{\lambda} \quad (2-15)$$

where D_{image} is the width of the input images and λ the wavelength. Better resolution allows a wider field of view to be imaged with smaller focal lengths.

2.5 Performance Comparison

As mentioned above, frame rate, diffraction efficiency, resolution, and linearity are important criteria to study when examining the performance of an OASLM. Other practical considerations include applied voltage requirements, electrical power requirements, and fabrication requirements. For example, PROM's require high voltage but little electrical power, whereas SEED's require small applied voltages but dissipate a lot of electrical power. Of all the devices mentioned, SEED's require the greatest fabrication complexity while PROM's require the least. The fabrication complexity of the MQW-OASLM is a compromise. A summary of various performance related criteria is given in Table 2-1.

To directly compare the performance of the OASLM's mentioned above, we follow Williams and Moddel [34, 20] and examine three criteria: bit rate per area, optical sensitivity, and switching energy per bit. For non-pixelated devices, two effective bits or pixels are assigned to the resolution limit, and the areal bit rate density gives the number of bits in one square centimeter that can be switched in one second. This benchmark represents an effective throughput, and allows slower devices with a large number of pixels to be compared against fast devices with a small number of pixels. The sensitivity is simply measured by the required optical intensity, and the switching energy per bit gives the trade-off between speed and intensity requirements. The areal bit rate density versus sensitivity is shown in Fig. 2-9 for a variety of devices along with a line of constant switching energy at 1 pJ/bit. For devices limited by photoconduction, the indicated points can slide along such constant switching energy lines; for example, a greater bit rate can be achieved at larger intensities. In some devices, the maximum bit rate is not limited by the photoconductive response rate. For example, devices using nematic liquid crystals are limited by the switching time of the liquid crystals, and arrays of SEED devices are limited by heat dissipation.

As indicated in Fig. 2-9, the modified PROM structure using GaAs MQW's (1st GaAs-OASLM) improves the areal bit rate density by three orders of magnitude. This is due to improvements in both the frame rate and the resolution. As the "Modeled MQW-OASLM" point shows, the optimization techniques developed in this work indicate that the

Device	Resolution 50% MTF (lp/mm)	Frame Rate (Hz)	Sensitivity (W/cm ²)	Voltage (V)
Hughes LCLV	40	67	4×10^{-4}	10
PROM	12	1×10^4	5×10^{-2}	1000
α -Si/nematic	82	50	6×10^{-5}	5
α -Si/smectic	70	1×10^3	2.5×10^{-4}	10
SEED	(20 μ m)	1×10^8	10	15
1 st GaAs MQW-OASLM	50	3×10^5	0.3	30
Modeled MQW-OASLM	140	1×10^5	1×10^{-2}	20

Table 2-1 Performance comparison of the optically addressed spatial light modulators discussed in this chapter. The resolution column gives, in line-pairs per millimeter, the point at which the MTF drops by 50%. For the SEED the pixel size is given. The frame rate and sensitivity give the frequency at which the devices can be run at the indicated optical intensity levels. The applied voltage requirements are also given. The results for the first six devices are from typical experimental operating conditions. The parameters for the first four devices are from [34], the SEED parameters are from [25], the 1st GaAs MQW-OASLM parameters are from [29], and the modeled MQW-OASLM parameters are from this work.

sensitivity can be improved as well, producing a device with the lowest overall switching energy per bit. These optimization techniques are described in Chapter 7.

2.6 Summary

The search for the ideal modulator from which to produce an optically addressed spatial light modulator involves many trade-offs, some of which are intrinsic to the materials themselves. These trade-offs could be, for example, speed for electro-optic effect, or electro-optic effect for fabrication complexity or spectral bandwidth. For example, while

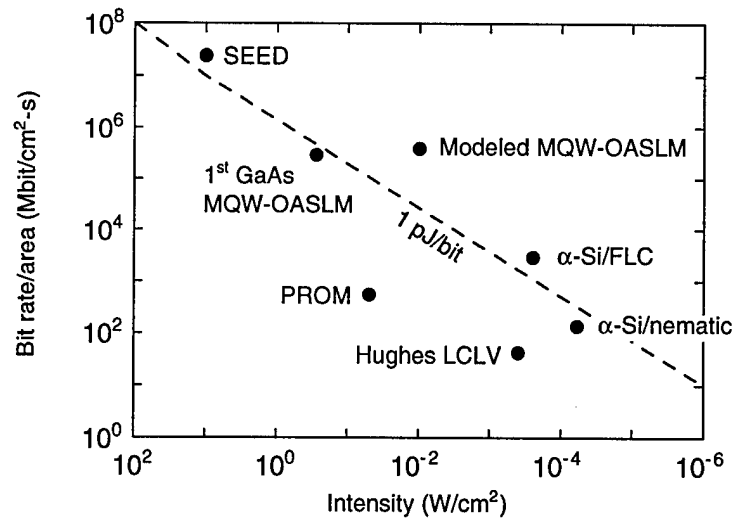


Figure 2-9 Comparison of the bit rate per area and intensity requirements for the OASLM's discussed in this chapter. The 1pJ/bit switching energy per bit line gives the trade-off between bit rate and intensity for photoconductive-limited devices. The modeling of the MQW-OASLM performance in this work indicates that this device can have the lowest switching energy per bit of all the illustrated devices.

nematic liquid crystals display large electro-optic effects, they are intrinsically slow due to the physical effect of having to rotate an entire molecule during the modulation process. Ferroelectric liquid crystals overcome this limitation, but at the expense of only being able to produce a binary response. Other limitations occur in electro-optic materials used in PROM type geometries which rely on the carrier transport and linear electro-optic material properties. In these materials, these two processes are linked via the lattice polarizability [35]. Thus, for example, materials with good lattice polarizability such as Lithium Niobate (LiNbO_3) tend to have large electro-optic effects but poor carrier transport behavior due to large phonon scattering. On the other hand, materials such as GaAs with low lattice polarizability have very good transport behavior but weak linear electro-optic effects. The MQW-OASLM overcomes this limitation in the PROM geometry by decoupling the source of the transport behavior from the source of the electro-optic effect. The trade-off here is in increased fabrication complexity, and a quadratic and wavelength-resonant electro-optic response. Compared to other devices such as the SEED, however,

the MQW-OASLM fabrication is much simpler, and overall it provides a nice compromise among the various trade-offs, producing a device with very good resolution, bit rate, and, as we shall see in Chapter 6, linearity.

Chapter 3

Optical and Transport Properties of Multiple-Quantum-Wells

As discussed in the previous chapter, the success of the MQW-OASLM depends on the combination of the fast carrier transport and the sensitive electro-optic properties of quantum wells. This combination arises from quantum confinement which creates a very large, resonant electro-optic effect while retaining the good carrier mobilities of gallium arsenide. This electro-optic effect, known as the quantum confined Stark effect, is more than three orders of magnitude stronger than the intrinsic Pockels effect in GaAs. While the carrier mobilities remain high in MQW structures, carrier transport is not completely unaffected by quantum confinement. Two types of carriers with very different transport characteristics are created: confined carriers in the well subbands, and free carriers in the transport bands above the barriers. One of the main challenges in modeling such a system is finding a way to include quantum wells in standard semiconductor device models so that practical simulation-related issues such as boundary conditions and multiple time scales can be realistically addressed.

This chapter begins with a brief review of the electronic structure of bulk gallium arsenide, followed by a discussion of the confined states in a GaAs/AlGaAs quantum well. A summary of the main optical properties of GaAs/AlGaAs quantum wells is presented, including a discussion of excitonic absorption, the quantum confined Stark effect, and the use of quantum wells as the source of a very large, resonant electro-optic effect. The

impact of quantum confinement on carrier transport, including a detailed calculation of the escape rates of confined carriers, is then presented. Finally, a shallow trap model which allows the inclusion of quantum wells in the standard semiconductor drift-diffusion model is described.

3.1 Electronic Structure

Gallium arsenide (GaAs) is a very versatile and high performance semiconductor that is used in a variety of opto-electronic applications such as photo-detectors, light emitting diodes, and diode lasers. Its material and electronic properties have been studied and optimized over the last several decades, and, along with aluminum-gallium-arsenide (AlGaAs), it is one of the most reliable and popular materials used in fabricating quantum-well devices. As this materials system is the basis for the devices studied in this thesis, we shall use it as an example throughout this chapter.

GaAs is a III-V compound semiconductor that crystallizes into a zinc-blende type unit cell. As in all crystalline solids, the periodic potential induced by the repeating unit cells produces a one-electron Hamiltonian with translational symmetry along the lattice. The corresponding electron eigenstates are known as Bloch functions and consist of the product of a periodic function, u_{nk} , with the same periodicity of the lattice and a more slowly varying plane wave envelope function [36]. These eigenstates are written in the form

$$\langle \mathbf{r} | nk \rangle = \psi_{nk}(\mathbf{r}) = e^{i\mathbf{k} \cdot \mathbf{r}} u_{nk}(\mathbf{r}) \quad (3-1)$$

The space coordinate is given by \mathbf{r} . The eigenstates are characterized by the band index, n , and the Bloch wavevector, \mathbf{k} . Figure 3-1 shows a plot of the band diagram for GaAs along various lines in k -space. Each curve, or band, corresponds to a different value of n . The band energies are plotted between special symmetry points of the zinc-blende Brillouin zone. The room temperature GaAs bandgap of 1.42 eV occurs at $\Gamma(\mathbf{k}=0)$ in the Brillouin zone, separating the lower and upper bands into valence and conduction bands, respectively. Optical and thermal excitation of electrons from the valence to conduction bands

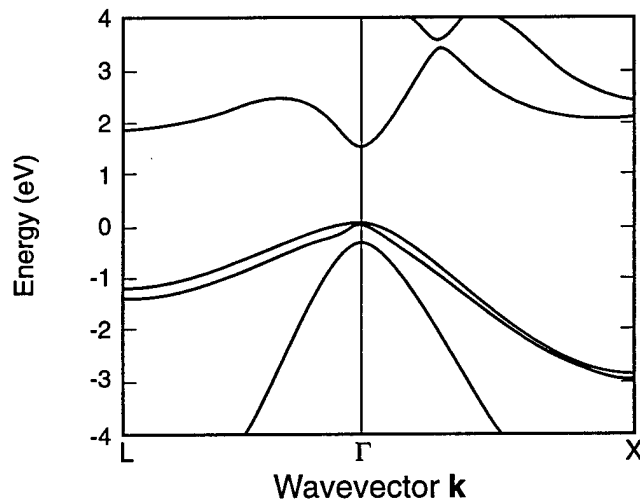


Figure 3-1 Band diagram of bulk GaAs showing the direct bandgap and degenerate hole bands at Γ . Other conduction band minima, or valleys, at L and X play important roles in carrier transport and carrier escape from quantum wells. After Kittel [37].

produces vacancies in the valence bands known as holes. An important feature of the bands near $k=0$ is that they are approximately parabolic in k ($k = |\mathbf{k}|$). This is similar to the case of a free electron in which the free space kinetic energy is quadratic in k . Also, as in the free space case, the curvature of the energy vs. k curve can be related to an effective mass of the particle. For example, in the case of GaAs, the two degenerate hole bands at Γ are denoted the light hole (LH) and heavy hole (HH) bands due to their different effective masses.

The conduction band in GaAs displays parabolic local minima, or valleys, at other points in k -space, namely near $L=\pi/a(1,1,1)$ and $X=2\pi/a(0,0,1)$ where a is the lattice constant. These valleys can become occupied through high energy phonon scattering and can greatly affect the carrier transport properties, as well as the escape rates, of carriers in quantum wells. These issues will be discussed below.

Alloys of GaAs such as $\text{Al}_x\text{Ga}_{1-x}\text{As}$ can be formed through suitable fabrication techniques, although they are not truly crystalline but rather a type of solid solution. However, for most basic electronic calculations it has been found that treating the potential as a weighted average over the crystalline potentials of GaAs and AlAs produces acceptable results and allows the retention of the Bloch formalism [36]. The bandgap of $\text{Al}_x\text{Ga}_{1-x}\text{As}$

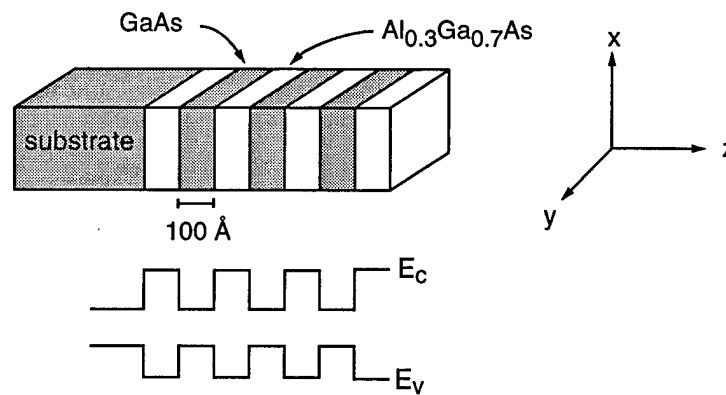


Figure 3-2 Sketch of a GaAs/AlGaAs multiple-quantum-well structure which is typically grown on top of a GaAs substrate wafer. The growth direction is along z , and the corresponding variations of the conduction and valence band edges are shown.

varies linearly with composition from the bandgap of GaAs up to that of $\text{Al}_{0.4}\text{Ga}_{0.6}\text{As}$ (from 1.42eV to 1.92eV) with only a minimal change in lattice constant. This allows the fabrication of high quality heterostructures made of layers of differing compositions. These multi-layer heterostructures are typically fabricated using either molecular beam epitaxy (MBE) or metal organic chemical vapor deposition (MOCVD). In MBE, the layers are grown one atomic layer at a time in ultra high vacuum conditions from the evaporation of solid sources [38]. In MOCVD, the reaction of gaseous group III alkyls and group V hydrides over a heated substrate is used to grow epitaxial layers [39]. Abrupt compositional transitions of a monolayer can be routinely made with these techniques.

A GaAs/AlGaAs multiple-quantum-well structure consists of thin ($\sim 100 \text{ \AA}$) alternating layers of GaAs and $\text{Al}_x\text{Ga}_{1-x}\text{As}$. A diagram of the band edges in a typical GaAs/AlGaAs MQW structure is shown in Fig. 3-2. The alternating energy along z breaks the translational symmetry of the bulk material, and the larger bandgap $\text{Al}_x\text{Ga}_{1-x}\text{As}$ ‘barriers’ confine the lowest lying electron and hole states to the smaller bandgap GaAs ‘well’ regions. To describe this confinement, the plane wave envelope function in the bulk Bloch function, Eq. (3-1), must be replaced with an envelope function of the form

$$\chi(z)e^{ik_{\perp} \cdot r_{\perp}} \quad (3-2)$$

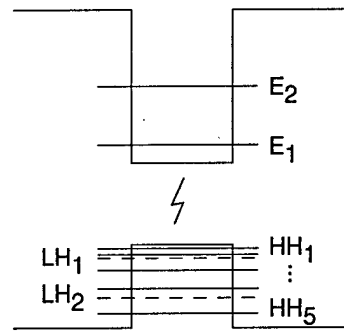


Figure 3-3 Electron(E), heavy hole(HH), and light hole(LH) subbands for an isolated GaAs/Al_{0.29}Ga_{0.71}As quantum well with a well width of 100 Å. The bandgap between the conduction and valence band has been shrunk to highlight the well states. Note the smaller barrier height for the hole states and the large number of subbands for the heavy hole due to its larger effective mass.

where χ is a confined envelope wavefunction and k_{\perp} and r_{\perp} are the components in the x - y plane [36]. The states are thus confined along the growth direction, z , but are free in the x - y plane.

Near $k_{\perp} = 0$, χ solves the envelope Hamiltonian of the form

$$-\frac{\hbar^2}{2} \frac{\partial}{\partial z} \frac{1}{m(z)} \frac{\partial}{\partial z} \chi + V(z)\chi = E\chi \quad (3-3)$$

where $m(z)$ is the effective mass in the different layers, $V(z)$ is the band edge potential energy, and E is the energy eigenvalue [36]. Equation (3-3) is solved along with continuous boundary conditions on χ and $\frac{1}{m} \frac{\partial}{\partial z} \chi$ at the interface between different layers.

The bulk properties of the different layers are encapsulated into the effective electron and hole masses and the confining barrier potential. Equation (3-3) is essentially the problem of a particle in a box. Each bulk band, conduction or valence, produces a corresponding set of solutions to the above Hamiltonian called subbands. For GaAs, the most important subbands are the light and heavy hole subbands in the valence band and the electron subbands in the conduction band. As an example, the energy levels for these subbands are indicated in Fig. 3-3 for an isolated quantum well with the following properties:

well width = 100 Å, $x = 0.29$, and barrier height and effective masses from Moss [40]. In this example, there are two electron subbands, five heavy hole subbands, and two light hole subbands. While the hole energies are degenerate in bulk GaAs, in quantum-well structures this degeneracy is removed in the subbands because of the different hole effective masses.

While the vertical motion of the electrons is confined, the in-plane behavior resembles a 2D electron gas in which the electron momentum is given by $\hbar k_{\perp}$. The above analysis has been for $k_{\perp} = 0$ which, for most of our work, is sufficient for the calculation of χ . For $k_{\perp} \neq 0$, mixing can occur between the different subbands, distorting them from a nominal parabolic shape. For our purposes, however, it will be adequate to approximate subbands as parabolic with appropriate effective masses.

3.2 Optical Properties

The quantum confinement of electrons and holes produces very noticeable effects on the optical properties of quantum-well structures. At special exciton resonances, the absorption increases dramatically, and both the absorption and index of refraction become very sensitive to an applied electric field. From a device perspective, this allows the construction of very low voltage, compact optical modulators.

3.2.1 Excitons

The most obvious optical property affected by quantum confinement is the absorption spectrum. Fig. 3-4 shows the absorption spectrum at zero applied voltage for the 100 Å-GaAs/35 Å-Al_{0.29}Ga_{0.71}As MQW system in the active region of the MQW-OASLM described in Fig. 2-5. This data was taken with a 0.5 m monochromator illuminated with a white light source and with an output FWHM resolution of 1 nm. An AC applied voltage was used to suppress the screening effects described in Chapter 4. Just past the absorption edge at ~850 nm, two prominent peaks are evident. These arise from a many body state called an exciton that is due to the correlated interaction of electrons in the quantum

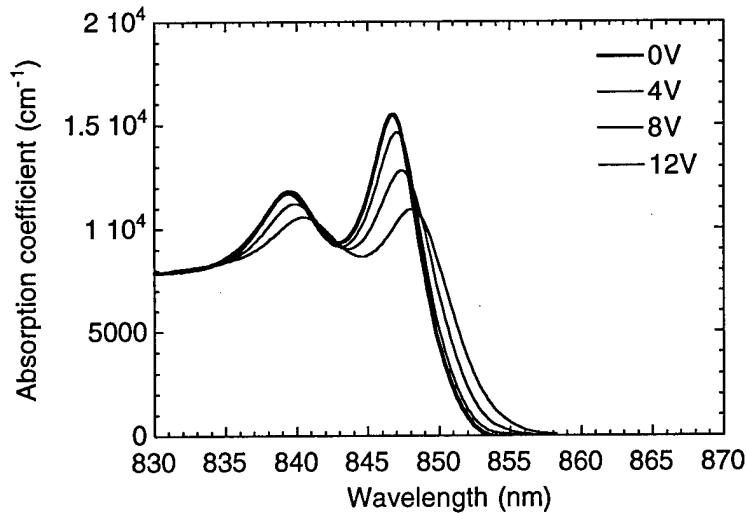


Figure 3-4 Absorption spectrum of a 155 period 100 Å-GaAs/ 35 Å- $\text{Al}_{0.29}\text{Ga}_{0.71}\text{As}$ multiple-quantum-well system for the indicated applied voltages. The corresponding fields are 0, 11.8, 23.6, and 35.4 kV/cm. The two peaks are caused by exciton absorption, and the red shift and decay of the peaks as the field is increased are due to the quantum confined Stark effect.

wells [13]. During absorption of a photon, an electron is promoted from one of the valence subbands to one of the conduction subbands. The resulting vacancy, or hole, and the electron form a bound electron-hole pair which, formally, resembles a 2D hydrogenic state characterized by an effective Bohr radius λ_0 [36]. The quantum confinement provided by the barriers produces a tightly bound exciton state and thereby stabilizes the exciton against field and phonon ionization. The exciton binding energy arises, essentially, from a *reduction* in the electron-electron repulsion in the interacting, many body system. The strongest exciton resonances correspond to the most tightly bound exciton states.

Each valence-conduction subband combination offers the possibility of forming an exciton resonance, though the absorption coefficient of many combinations is suppressed due to polarization and parity considerations [36]. In Fig. 3-4, the peak at 840 nm corresponds to the exciton created between the LH_1 and E_1 subbands, and the peak at 847 nm arises from the HH_1 and E_1 subbands.

Not only does quantum confinement stabilize the exciton, but the enhanced overlap between the electron and hole states produces a larger absorption coefficient. The peak absorption due to the most tightly bound exciton state (1S) can be estimated as [36]

$$\alpha = \frac{4\pi^2 e^2 E_p}{n c m_0 L \omega \lambda_0^2} |\langle \chi^{(h)} | \chi^{(e)} \rangle|^2 \frac{1}{\Gamma \sqrt{2\pi}} \quad (3-4)$$

where E_p is the product of the electron effective mass and the square of the velocity matrix element between valence and conduction band atomic basis functions, n is the index of refraction, c is the speed of light, m_0 is the electron effective mass, L is the device length, ω is the optical frequency, $\chi^{(h)}$ and $\chi^{(e)}$ are the hole and electron envelope wavefunctions, respectively, and Γ is the width of the exciton resonance curve which is typically a Gaussian. The exciton absorption from Eq. (3-4) is typically over an order of magnitude larger than the non-resonant, continuum absorption that occurs at shorter wavelengths [36]. Note the strong dependence on the overlap between the electron and hole envelope wavefunctions.

3.2.2 Quantum Confined Stark Effect

The application of a uniform electric field along the growth direction in a MQW structure drastically alters the absorption spectrum. This is illustrated in Fig. 3-4 for applied voltages from 0 to 12 V, which corresponds to applied fields from 0 to 35 kV/cm. Two obvious trends are evident: a red shift of the resonant wavelength of the excitons to longer wavelengths as the field is increased, and a corresponding reduction in the maximum value of the absorption peaks. The origin of these effects lies in the changes induced by the applied field on the electron and hole envelope wavefunctions. Sketches of the effective potential (band edges) and the resulting envelope wavefunctions are shown in Fig. 3-5 for a GaAs/AlGaAs quantum well in zero applied field and in an applied field of 100 kV/cm. At large fields, the ramping potential polarizes the electron and hole states at opposite corners of the well, reducing the wavefunction overlap. From Eq. (3-4), this reduces the peak value of the absorption. As the wavefunctions polarize at opposite sides of the well, they

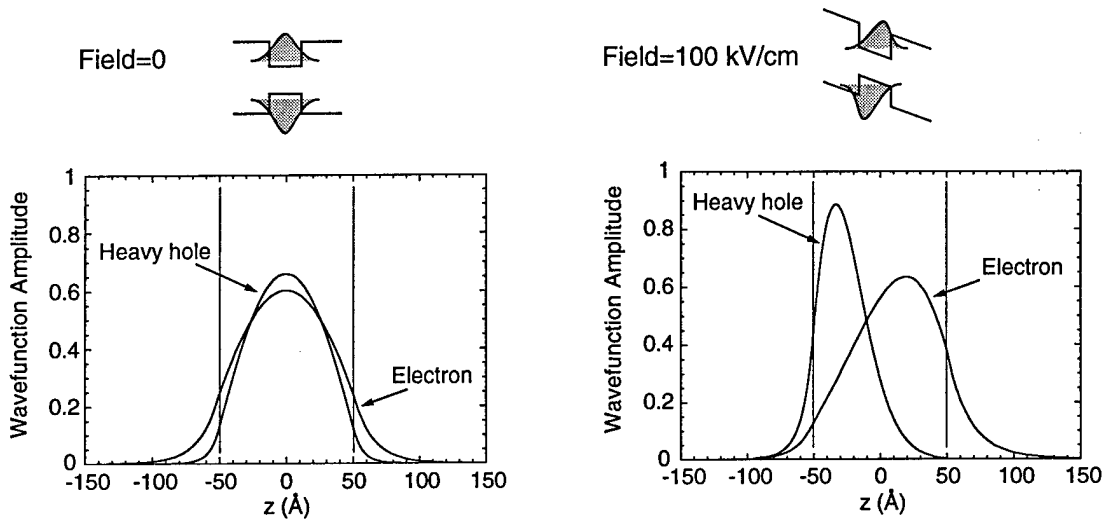


Figure 3-5 Illustration of the changes in the electron and heavy hole wavefunctions due to the quantum confined Stark effect as computed using the transfer matrix method for a single 100 Å-GaAs/Al_{0.29}Ga_{0.71}As quantum well. For zero applied field, as shown on the left, the electron and heavy hole wavefunctions are centered in the well which is indicated by the two vertical lines. For non-zero field, the electrons and holes become polarized at opposite sides of the well.

also “sink” into their respective corners of the well causing a reduction, or red shift, in the resonant energy. This field dependent effect is known as the quantum confined Stark effect (QCSE) and is, to lowest order, quadratic in the applied field [13].

The calculation of the envelope wavefunctions in an applied field requires the solution of the envelope Hamiltonian, Eq. (3-3), with the band edge potential including the linear ramp from the applied field. Approximate results can be obtained with variational treatments [41], but since the carriers can tunnel out of the well on the downstream side the states are actually quasi-bound and are more accurately handled with numerical techniques. One of the most convenient techniques for handling this situation is the transfer matrix technique (TMT) [42, 43]. This technique involves discretizing the band edge potential into small regions of uniform energy which can then be solved with plane wave solutions. Matching boundary conditions across regions allows for a scattering type of treatment in which the occupation probability inside the well is calculated over a range of energies. The peak in this probability vs. energy curve gives the quasi-bound energy, and

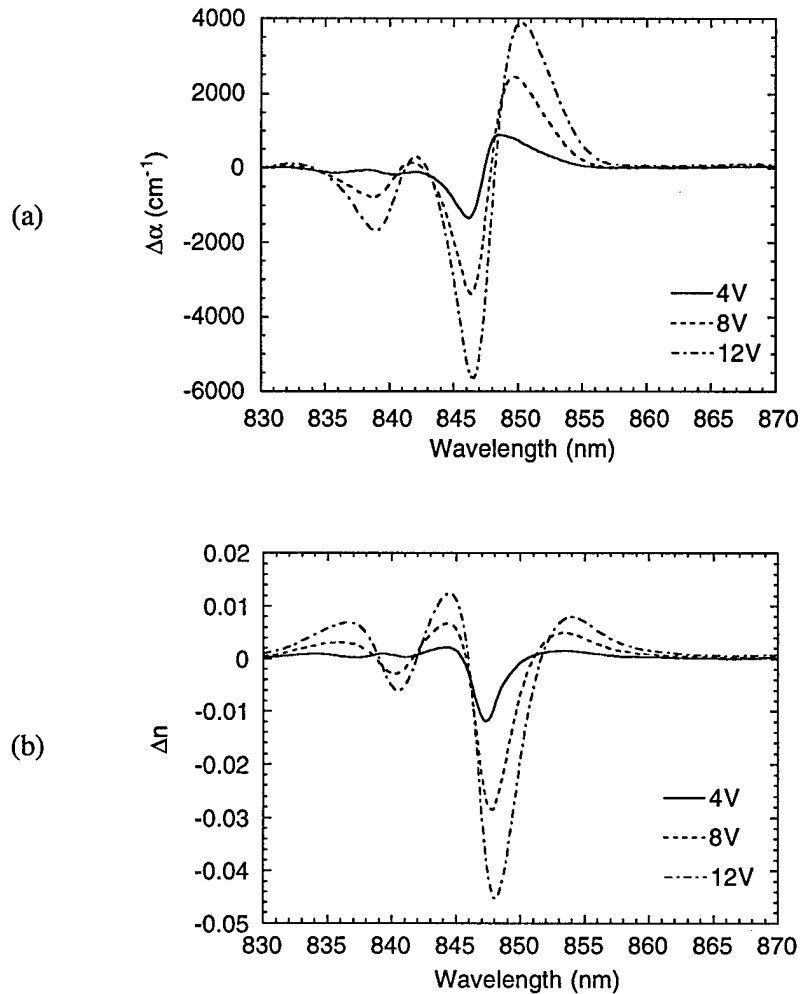


Figure 3-6 a) Absorption change induced by the QCSE. b) Corresponding index change calculated via a Kramers-Kronig transformation of a).

the width of the curve gives the tunneling lifetime of the quasi-bound state [43]. The results in Fig. 3-5 were computed using this technique.

3.2.3 Electro-optic Effect

The large changes in absorption due to the QCSE (greater than 6000 cm⁻¹ at 50 kV/cm) can be exploited to produce a sensitive electro-optic effect that replaces the rather weak linear electro-optic effect in GaAs ($\Delta n \sim 10^{-6}$ at 50 kV/cm). The wavelength dependence of the absorption change for various voltages, i.e. $\alpha(V) - \alpha(0)$, is shown in Fig. 3-6a. Since

there are large wavelength dependent changes in the absorption, there are also large changes in the index of refraction. The result of a Kramers-Kronig transformation on the absorption-change spectrum produces the corresponding index-change spectrum shown in Fig. 3-6b. Index changes as large as 0.05 at 50 kV/cm are produced by the QCSE.

When using the QCSE induced absorption and index modulation as an electro-optic effect, it is important to note two things. First, it is a resonant effect, producing large modulation only for wavelengths near the exciton resonances. The spectral bandwidth is only about 5 nm. Second, to lowest order, the changes are quadratic in the internal field for symmetric wells. This limits the response at low applied fields.

3.3 Transport Properties

Besides giving rise to the quantum confined Stark effect, the quantum confinement of carriers also significantly alters the carrier transport properties of quantum-well devices. Essentially two types of carriers are created: well-confined carriers that only transport in the plane of the wells, and free-carriers which undergo bulk-like transport above the barriers. Carrier exchange between these two types of carriers occurs through various escape and capture events. In this section, a shallow trap model is described which allows these two types of carriers to be straightforwardly included in standard semiconductor transport models. A detailed calculation of the escape rates for both electrons and holes is also presented.

3.3.1 Vertical vs. In-plane

The carrier transport in a MQW structure is highly anisotropic since the carriers in the wells are confined in the growth, or so-called vertical, direction but free in the transverse, or in-plane directions (see Fig. 3-7). Well-confined carriers can also escape into the transport bands above the barriers where they undergo transport in both the vertical and transverse directions. The carrier transport in most devices is usually dominated by only one of these types of transport. For example, the transport in optical modulators and p-i-n

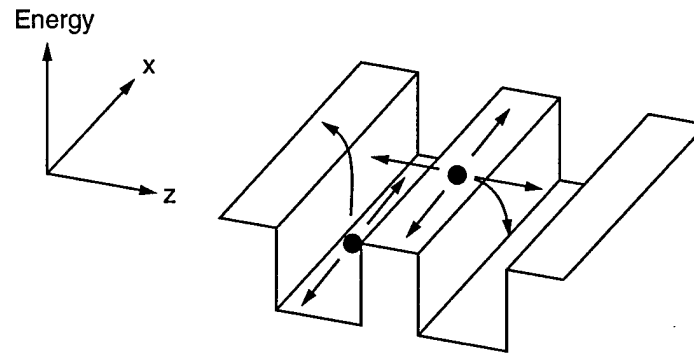


Figure 3-7 A plot of the conduction band energy for a quantum-well system over two spatial dimensions. Carriers in the wells are confined along the growth (z) direction but are free to transport in the plane of the wells (x). Carriers in transport bands above the barriers can transport in both directions. The two types of carriers are connected via escape and capture processes.

photodiodes is exclusively along the vertical direction while the transport in modulation doped field effect transistors is along the in-plane direction. In contrast, in the MQW-OASLM we must consider both types of transport.

The in-plane transport of carriers in a quantum-well can be modeled in a fashion similar to bulk transport by using a drift-diffusion model. The drift-diffusion model considers the change in the carrier concentrations caused by the differential flux of drift and diffusion currents. It can be derived from the first moment of the Boltzmann transport equation and is the standard model for simulating transport in semiconductors [44]. For example, this model has been used to simulate in-plane transport in modulation-doped field effect transistors [45] and photorefractive quantum-well devices [46].

Vertical transport involves the escape of carriers from the wells, transport in bulk-like states above the barriers, and then recapture back into the wells. For typical capture times and transit times, a carrier undergoes many of these escape/transport/capture cycles during transit across the MQW region. As we show below, this process can also be modeled using a drift-diffusion model for transport above the barriers, and appropriate escape and capture rates describing the exchange between well-confined and free carriers.

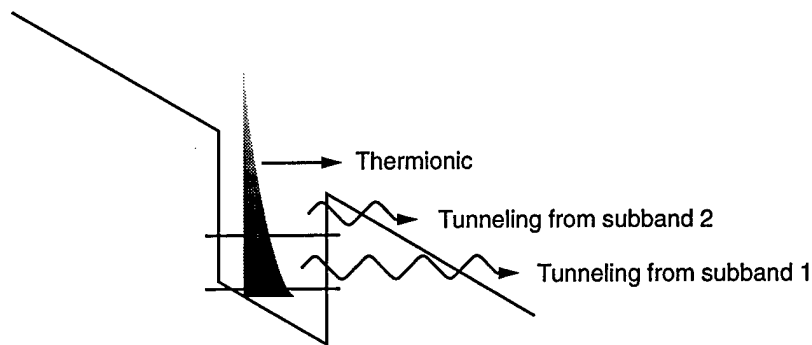


Figure 3-8 The escape of electrons from a quantum well via thermionic emission and tunneling. In the Moss model, carriers with a 3D density of states in the tail of the indicated Boltzmann distribution escape via thermionic emission. Carriers with a 2D density of states in each of the well subbands escape via tunneling through the downstream barrier. The tunneling time for carriers in the second subband is very short due to the smaller barrier height.

3.3.2 Escape Mechanisms

There are many processes by which a carrier confined in a quantum well can escape into the continuum above the barriers or into a neighboring well. Inter-well processes include miniband conduction in Bloch-like states created from the quantum-well superlattice [47], phonon scattering transitions between subbands in neighboring wells [48], and direct, resonant tunneling between neighboring subbands [49]. Continuum-escape processes include thermionic emission and coherent tunneling across neighboring wells [50]. The significance of each process depends strongly on the barrier height, barrier thickness, and temperature.

At room temperature, and for barrier thicknesses greater than 20 \AA , thermionic emission and coherent tunneling are expected to be the dominant escape processes [50]. Thermionic emission is the escape of carriers in the tail of the Boltzmann distribution with energies above the barrier height. Tunneling is the escape of carriers via coherent, quantum mechanical tunneling through a finite barrier. These two processes are in fact linked since the thermal occupation of higher subbands allows for faster escape by tunneling through a smaller barrier height as diagrammed in Fig. 3-8. Several theories which treat these processes separately have been presented in the literature [51, 52]. However, a more

complete model which considers these two processes together has recently been presented by Moss *et al.* [40]. We now briefly outline this model and give some results for a GaAs/AlGaAs quantum-well system.

In the Moss model, the carriers in one quantum-well period are assumed to be of two types: 2D, confined carriers with energies below the top of the barrier, and 3D, bulk-like carriers with energies above the barrier. The escape of carriers out of the well region is described by

$$\frac{dN}{dt} = -\frac{N}{\tau} \quad (3-5)$$

where N is the effective total volumetric density of carriers in one quantum-well period and τ is the escape time given by

$$\frac{1}{\tau} = \frac{1}{\tau_{TE}} + \sum_i \frac{f_i}{\tau_i} \quad (3-6)$$

where $1/\tau_{TE}$ is the escape rate due to the thermionic emission of the 3D carriers with energies above the barrier, and f_i/τ_i is the escape rate of the 2D carriers in the i^{th} subband due to tunneling through the downstream barrier into the continuum. The fractional occupancy of the i^{th} subband in thermal equilibrium is given by f_i , and τ_i is the corresponding tunneling time. The f_i 's are calculated by counting the fractional occupancy of each subband, taking into account the 2D density of states for well-confined carriers and the 3D density of states for unconfined carriers. One subtlety of this calculation is the conversion of the surface density of confined carriers to an effective 3D volumetric density by dividing the surface density by the quantum-well period. The subband tunneling times are calculated using the TMT technique described previously. For the thermionic emission of electrons, Moss considers the escape from both the Γ and L valleys in the wells into the Γ valley in the barriers. The contribution of L-valley electrons can be significant for large barrier heights.

The thermionic emission rate follows an Arrhenius type of behavior:

$$\frac{1}{\tau_{TE}} \sim e^{-\Delta E_b/k_B T} \quad (3-7)$$

where $k_B T$ is the thermal energy and $\Delta E_b = V_b - eFd/2$ is the downstream barrier height that is decreased from the zero field barrier height of V_b by the applied field, F , over the quantum-well width d . The thermionic emission rate thus increases slightly with applied field and is very sensitive to the barrier height V_b .

The tunneling rate of a given subband depends on the thermal occupation of the subband and on the subband lifetime. The occupancy of a subband in thermal equilibrium shows an Arrhenius type dependence on the subband energy, E_i ,

$$f_i \sim e^{-E_i/k_B T} \quad (3-8)$$

and thus decreases significantly for higher subbands. The lifetime also depends strongly on the subband energy. It can be estimated from the Fowler-Nordheim tunneling equation for a particle with mass m and subband energy E_i as [53]

$$\tau_i \propto e^{\frac{4\sqrt{2m}(V_b - E_i)^{3/2}}{3eF\hbar}} \quad (3-9)$$

and decreases strongly for higher subbands. Thus, even though higher subbands may not be significantly populated, at large fields their carrier lifetimes may be short enough to allow them to dominate the escape process.

Using the above model, we now present some calculations of the escape rate for the MQW system used in the MQW-OASLM described in Chapter 2. This system consists of 100 Å-GaAs / 35 Å-Al_{0.29}Ga_{0.71}As quantum wells. The subband energies in Fig. 3-3 are for an isolated well of this system. We first present the electron results. The escape rate is calculated by computing the subband energies and lifetimes using the TMT method. We consider a two well system and calculate for the upstream well. This gives some indication of the effect of downstream wells in a *multi*-quantum-well system. As discussed above, there are two subbands in each well. The resulting escape rate versus applied field is shown in Fig. 3-9. For small fields, thermionic emission dominates the escape process

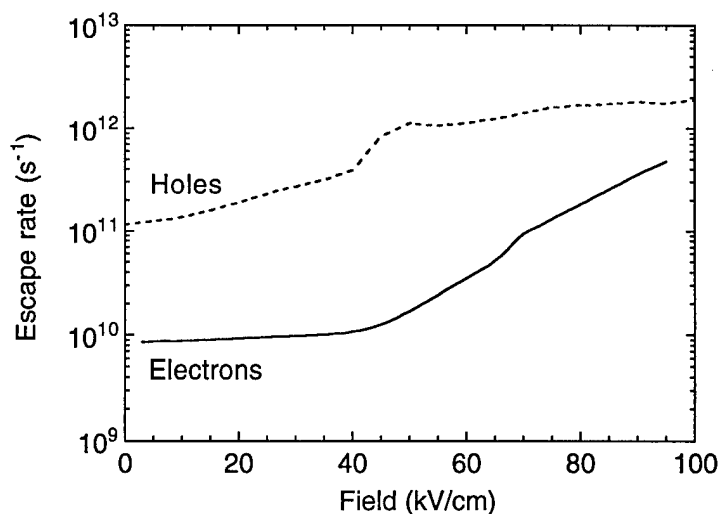


Figure 3-9 Escape rates for electrons and holes computed using the Moss model. The low-field rates are determined by thermionic emission, with the holes demonstrating an order of magnitude faster rate than the electrons due to the much smaller barrier height in the valence band. Tunneling becomes significant at large fields, especially for electrons.

while at larger fields the tunneling of electrons from the thermally occupied second subband dominates.

Similar calculations can be performed for holes. In this case the light holes and heavy holes each produce different thermionic emission and tunneling rates, although only Γ valley emission needs to be considered. As discussed above, there are five heavy hole subbands and two light hole subbands. The net escape rate for both types of holes is also shown in Fig. 3-9. At low fields, thermionic emission dominates the escape as was the case for electrons. The escape rate for holes, however, is much faster than the escape rate for electrons since the valence band barrier height is smaller. As the field increases, the escape rate increases first due to tunneling from the second light hole subband, and then increases again due to tunneling from the first light hole subband. Due to their large effective mass, heavy holes do not tunnel well.

As we shall see in following chapters, fast escape rates are very important to overall device performance. Generally, obtaining fast escape rates requires the use of 'shallow' quantum-well systems in which the barrier heights are very small. Short barriers, however,

weaken the quantum confinement. This can lead to fast exciton ionization and a weakening of the exciton absorption and QCSE. Good electro-optic response, however, has been demonstrated in an $\text{Al}_{0.1}\text{Ga}_{0.9}\text{As}/\text{Al}_{0.16}\text{Ga}_{0.84}\text{As}$ system with a very small electron barrier height of only 50 meV [54]. Repeating the above calculations for such a system gives escape rates for both electrons and holes greater than $1.0 \times 10^{12} \text{ s}^{-1}$, even at low fields.

3.3.3 Shallow Trap Model

The treatment of the escape of carriers out of the wells described above along with free-carrier capture processes is reminiscent of the Shockley-Read-Hall model for traps in bulk material [55]. In fact, this analogy has been used to include quantum wells in above-barrier transport models in a relatively simple way [56, 57]. In particular, Magherefteh *et al.* have developed a conventional drift-diffusion model in which the wells are treated as shallow traps [28]. In this model, the discrete wells are replaced by the effective 3D volumetric density of carriers in each quantum-well region. The carriers in the well regions are coupled to the continuum, or free carriers, by the escape processes described above. As shown in Fig. 3-10, free carriers can also be captured by a well, i.e. a shallow trap, by phonon-scattering or other mechanisms [58]. These capture processes are characterized by capture times τ_n and τ_p for electrons and holes, respectively. Experiments have shown these capture times to be very fast, less than 1 ps [59]. The treatment of quantum wells as shallow traps is sketched in Fig. 3-10. The quantum-well escape and capture processes are treated as emission and capture processes from shallow traps within a bulk material. The relevant escape (emission) rates and capture times are described in the figure caption.

Quantum-well structures also contain intrinsic or intentionally doped midgap impurity or defect sites that can also act as traps. The trapping of carriers by these sites is modeled using the Shockley-Read-Hall recombination model which uses a similar capture/emission picture of trapping [55]. While free-carrier to midgap trap transitions could be considered in this quantum-well shallow trap model, only well to midgap trap transitions are included since the capture of free carriers by the wells is so fast. In Fig. 3-10, the capture of well-carriers by the midgap trap is characterized by the lifetimes τ_N and τ_P for electrons

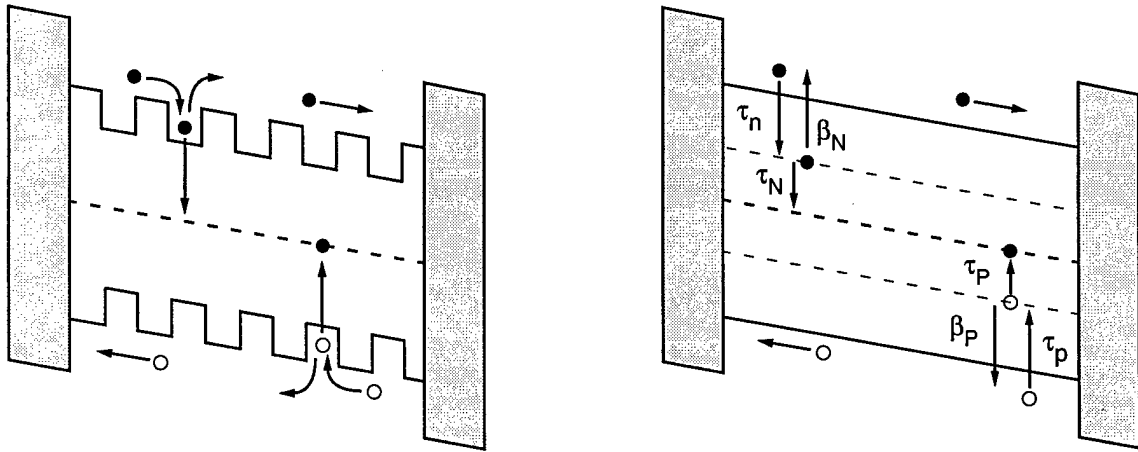


Figure 3-10 Diagram on the left shows escape and capture processes into and out of the quantum wells and trapping into the midgap traps. The diagram on the right shows the shallow trap model of MQW's in which the quantum wells are treated as shallow traps within a bulk material. The indicated escape, capture, and midgap trap rates are: β_N =well-electron escape rate, τ_n =free-electron capture time into the wells, and τ_N =well-electron lifetime for trapping into midgap traps. Hole parameters are similar.

and holes, respectively. For the operating regimes we consider, we neglect the thermal emission from the midgap traps.

In an extension of this basic shallow trap model, we also include the transport of carriers in the plane of the wells by adding a conventional drift-diffusion term to the continuity equations. Denoting the above-barrier, free-carrier densities as n and p , and the well-confined or shallow trap carrier densities as N and P , for electrons and holes, respectively, the well-carrier continuity equations are

$$\frac{\partial N}{\partial t} = \frac{1}{e} \frac{\partial j_N}{\partial x} + \frac{n}{\tau_n} - \left(\beta_N + \frac{1}{\tau_N} \right) N \quad (3-10)$$

$$\frac{\partial P}{\partial t} = -\frac{1}{e} \frac{\partial j_P}{\partial x} + \frac{p}{\tau_p} - \left(\beta_P + \frac{1}{\tau_P} \right) P \quad (3-11)$$

where the capture and emission parameters are described in Fig. 3-10 and where

$$j_N = e \mu_N \left(N E_x + V_T \frac{\partial N}{\partial x} \right) \quad (3-12)$$

$$j_P = e\mu_P \left(PE_x - V_T \frac{\partial P}{\partial x} \right) \quad (3-13)$$

are the drift-diffusion current densities in the plane of the wells. The mobilities for electrons and holes are given by μ_N and μ_P , respectively, $V_T = k_B T / e$ is the thermal voltage, with $k_B T$ the thermal energy, and e the electron charge. The transverse field is given by E_x . These equations will be used in conjunction with continuity equations for free-carrier transport and other equations to construct a full model of device operation in the following chapters.

3.4 Summary

One of the primary motivations for using quantum wells as the optical modulator in optically addressed spatial light modulators is the very strong electro-optic effect produced by the quantum confined Stark effect. This effect is a direct result of the quantum confinement of electronic states and produces index and absorption changes much larger than those which can be obtained in bulk material. The operation of OASLM's such as the MQW-OASLM, however, rely not only on the optical properties of the medium, but on the carrier transport properties as well. Quantum confinement essentially produces two classes of carriers: well-confined carriers that transport in the plane of the wells, and free-carriers that show bulk-like transport above the barriers. To handle these two classes of carriers, a shallow trap model for quantum wells was presented that allows the quantum wells to be included in the standard semiconductor drift-diffusion transport model in a familiar way. As we shall see in subsequent chapters, one of the most important performance related features of this model is the escape of carriers from the wells into the above-barrier bands. A detailed analysis of this process was given using a model that considered both thermionic emission and quantum mechanical tunneling. It was found that attaining fast escape rates at all field values requires the use of shallow quantum wells with very fast thermionic emission rates.

Chapter 4

Electric Field Screening

Device operation in multiple-quantum-well optically addressed spatial light modulators (MQW-OASLM) occurs through the screening of an applied voltage via the transport and trapping of photocarriers. While the most interesting and useful applications involve image formation, it is first necessary to treat the more basic case of uniform illumination in order to understand the screening process. This allows a more direct analysis of many important elements of device operation, such as the distributions of the interior carrier densities and the different types of operating regimes. As a case in point, the often used explanation of device operation describes screening as occurring through the accumulation of surface charges, yet no detailed model has been given to support this picture [29]. The only model presented to date to describe screening has been an equivalent circuit model by Nolte [15] which, as we show below, implicitly assumes dielectric relaxation. There has also been no previous attempt to explicitly include quantum wells in a device model. As we also show, quantum wells play an important role in determining the overall speed response.

In the basic MQW-OASLM design [6, 29, 61], a semi-insulating MQW region is sandwiched between two insulating buffer layers and two transparent electrodes as shown in Fig. 4-1. As discussed in Chapter 2, device operation occurs through the transport and trapping of photogenerated charge. Photogenerated carriers are separated by the applied field and drift toward the semiconductor-insulator interfaces where they are stopped by

the large bandgap insulating layers and accumulate in traps near the interfaces. A spatially varying image input to the device produces a corresponding spatially varying surface charge at the semiconductor-insulator interfaces. This surface charge screens the applied voltage and creates an electric field pattern that mimics the input image. The field pattern then modulates the quantum confined Stark effect (QCSE) to produce an index and absorption pattern. The transport of carriers along the bias field and along the transverse direction determines the speed and resolution performance.

In this chapter, we develop a 1D drift-diffusion model of screening that is appropriate for uniform illumination conditions. The shallow trap model from Chapter 3 is used to describe the carrier occupation of the quantum wells. The carrier distributions are explicitly calculated in the quasi-steady state regime, and an injection model is developed to model screening using simplified numerical solutions. Full numerical solutions of the transport equations are then used to verify the main results of the injection model and to examine the effects of drift velocity saturation. Other properties specific to quantum wells, such as resonant absorption and field dependent carrier emission, are examined with regard to speed performance.

4.1 Device Model

In the original MQW-OASLM design, the MQW region was made semi-insulating through proton implantation or Cr-doping, and the buffer layers were fabricated from insulating phosphate-silica-glass [6, 29]. Subsequent modifications have included substituting semi-insulating material in place of the insulators [60], using only one buffer layer [61], and using intrinsic rather than semi-insulating quantum-well material [62]. In this chapter, we consider a symmetric device structure, as shown in Fig. 4-1, with an interior MQW region of length $2L$ surrounded by large bandgap, insulating layers each of thickness d . Semi-insulating or intrinsic MQW material is modeled using deep, donor-like traps with density N_D , partially compensate by shallow acceptors with density N_A . Throughout most of the interior, the uniform density of donors is denoted N_D^i , while in a thin region of

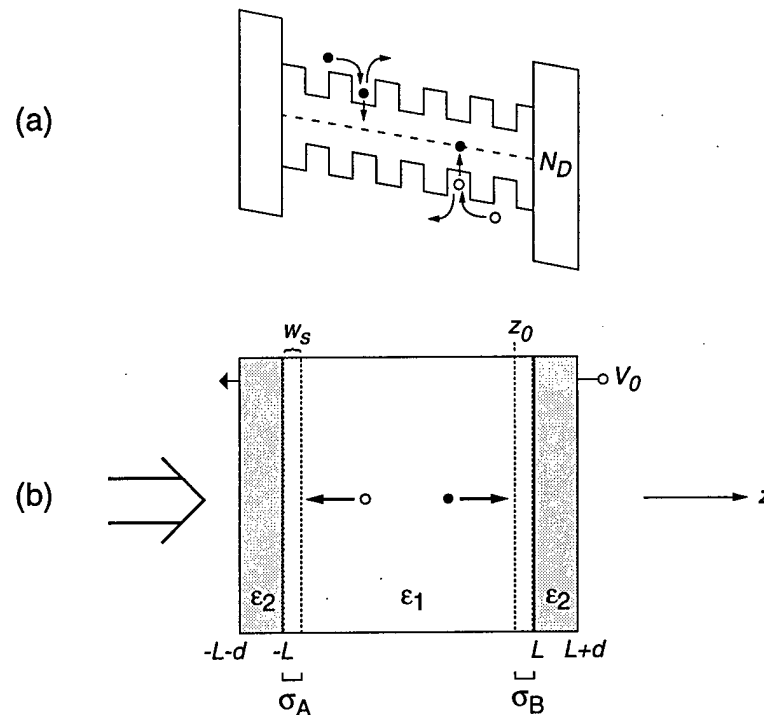


Figure 4-1 a) Band diagram used in device model showing interior quantum-well region surrounded by large bandgap insulating layers. Capture and emission processes for free and well carriers and the trapping of well-carriers in midgap donor-like traps are also shown. b) Device geometry showing interior quantum-well region of thickness $2L$ with dielectric permittivity ϵ_1 and insulating regions of thickness d with dielectric permittivity ϵ_2 . The thin regions of width w_s contain increased trap densities to hold the screening charge, σ_A and σ_B , at the semiconductor-insulator interfaces. Light is incident from the left and only 1D transport along z is considered.

thickness w_s near each of the semiconductor-insulating interfaces, the trap density is increased to N_D^s . These thin ($w_s \sim 50$ nm), high density trap regions are used to model surface traps and devices in which ion implantation or low temperature growth has been used to increase the trap density near the semiconductor-insulator interfaces in an attempt to improve resolution performance [29, 61, 63]. While the diagram in Fig. 4-1b shows a two-dimensional device geometry, for uniform illumination conditions only a one-dimensional device model along the quantum-well growth direction is necessary.

To model the screening process, we consider free electron and hole transport along with carrier transport in the quantum wells. The carriers confined in the wells are modeled

using the shallow trap model developed in Chapter 3. The densities of free carriers above the barriers, denoted by n and p for electrons and holes, respectively, are treated using a conventional drift-diffusion model in which the wells act as shallow traps. The carriers confined in the wells, with effective volumetric densities denoted by N and P , escape through thermionic emission and tunneling or become trapped in the midgap donor-like traps. Thermal excitation from the donor-like traps is neglected, and, for most of this chapter, non-resonant optical generation across the barrier bandgap is considered. The effects of resonant absorption between well subbands and QCSE absorption are briefly discussed in section 4.6. The rate equations for the densities of well carriers and the midgap donor-like traps are

$$\frac{\partial N}{\partial t} = \frac{n}{\tau_n} - (\beta_N + \gamma_N N_D^+) N \quad (4-1)$$

$$\frac{\partial P}{\partial t} = \frac{p}{\tau_p} - (\beta_P + \gamma_P (N_D - N_D^+)) P \quad (4-2)$$

$$\frac{\partial N_D^+}{\partial t} = \gamma_P (N_D - N_D^+) P - \gamma_N N_D^+ N \quad (4-3)$$

where the capture times of free carriers into the wells are given by τ_n and τ_p for electrons and holes, respectively, and the emission rates of confined carriers out of the wells are β_N and β_P for electrons and holes, respectively. As discussed in Chapter 3, the emission rates are field dependent due to the lowering of the barrier heights in large fields. The recombination coefficients for the trapping of well carriers into the donor-like traps for electrons and holes are γ_N and γ_P , respectively, and the density of unoccupied donor-like traps is given by N_D^+ . It should be noted that the donor-like trap recombination in Eqs. (4-1) and (4-2) is written directly in terms of the trap density rather than as a constant lifetime as was done in Chapter 3. In principle, this allows for an investigation of trap saturation, although for the regimes we consider this is not really an issue.

The continuity equations for free carriers are taken from standard semiconductor transport models [44, 64] and are given by

$$\frac{\partial n}{\partial t} = \frac{1}{e} \frac{\partial j_{nz}}{\partial z} + g(z) - \frac{n}{\tau_n} \quad (4-4)$$

$$\frac{\partial p}{\partial t} = -\frac{1}{e} \frac{\partial j_{pz}}{\partial z} + g(z) - \frac{p}{\tau_p} \quad (4-5)$$

where $g(z)$ is the photogeneration rate and

$$j_{nz} = e\mu_{nz} \left(nE_z + V_T \frac{\partial n}{\partial z} \right) \quad (4-6)$$

$$j_{pz} = e\mu_{pz} \left(pE_z - V_T \frac{\partial p}{\partial z} \right) \quad (4-7)$$

are conventional current densities for diffusion and drift in the vertical electric field E_z . The electron and hole mobilities are μ_{nz} and μ_{pz} , respectively. Following common terminology, we use vertical transport to refer to transport along the quantum-well growth and applied field direction (z) [65]. In general, the mobilities are field dependent due to velocity saturation [66].

The above system of transport equations is augmented by the following 1D Poisson equation for the potential, V ,

$$\frac{\partial}{\partial z} \left(\epsilon \frac{\partial V}{\partial z} \right) = -e(N_D^+ - N_A + p - n + P - N) \quad (4-8)$$

where ϵ is the dielectric permittivity.

As boundary conditions, the normal components of the free-carrier current densities are required to vanish at the semiconductor-insulator interfaces, and a voltage boundary condition is used at the edges of the device. The photogeneration term is given for light incident from the left in Fig. 4-1b by

$$g(z) = \frac{\alpha I_0}{h\nu} e^{-\alpha(z+L)} \quad (4-9)$$

where α is the absorption coefficient, I_0 is the incident intensity, and $h\nu$ is the photon energy. Analytical, simplified numerical, and full numerical solutions to the above system

of transport equations are given. For the full numerical solutions, dark, neutral initial conditions are used for the space charge, and the solutions are computed using the finite-difference discretization and second-order-implicit integration techniques described in Appendix A.

4.2 Carrier Distributions

Starting from dark initial conditions under a DC applied voltage and uniform illumination, the carrier densities buildup to a quasi-steady state over time scales given by the effective carrier lifetimes. This time scale is typically on the order of nanoseconds. The screening process, which occurs typically on the time scale of microseconds for CW illumination, begins from the quasi-steady state carrier distributions. Many aspects of screening performance, such as speed and resolution, are determined by the carrier distributions.

As in other shallow trap models [67], the effect of the quantum wells on the free-carrier densities can be described by effective transport and trapping parameters. For example, consider the effect of quantum-well capture and escape on the transport of free electrons. A free electron can drift in a field E_0 for an average time τ_n , and thus a distance $\mu_{nz}\tau_n E_0$, before being captured by a quantum well. Once in the well, it must wait an average time $1/\beta_N$ before escaping and again drifting in the applied field. Over a device of length L , the number of these capture/emission cycles is $L/\mu_{nz}\tau_n E_0$, and the time for each cycle is $(\tau_n + 1/\beta_N)$. The total transit time to traverse the device length is then

$$t_{transit} = \frac{L}{\mu_{nz}\tau_n E_0} (\tau_n + 1/\beta_N) \quad (4-10)$$

If we rewrite this in terms of the effective drift velocity, v_{drift} such that $t_{transit} = L/v_{drift}$ where $v_{drift} = \tilde{\mu}_{nz} E_0$, the effective vertical mobility $\tilde{\mu}_{nz}$ is given by

$$\tilde{\mu}_{nz} = \left(\frac{\beta_N \tau_n}{1 + \beta_N \tau_n} \right) \mu_{nz} \quad (4-11)$$

This is basically the free-carrier mobility weighted by the relative time spent in the conduction band above the barriers. Other effective transport parameters are developed below.

In the quasi-steady state regime, it is assumed that the rate of change of the carrier densities is much slower than the trapping rate, and the time derivatives of the carrier densities in the continuity equations may therefore be neglected [68]. For times short compared to the screening time, the amount of accumulated screening charge will be negligible, leaving the internal field with a uniform profile. This field is denoted $-E_0$. In this regime, the resulting 1D carrier continuity equations can be solved analytically for the free-carrier densities before screening begins. Making use of the quasi-steady state approximation for both captured and free carriers, the free-electron continuity equation can be written as

$$-L_D^2 \frac{\partial^2 n}{\partial z^2} + L_E \frac{\partial n}{\partial z} + n = g_0(z) \tilde{\tau}_{Rn} \quad (4-12)$$

where $\tilde{\tau}_{Rn} = \tau_n(1 + \beta_N \tau_N)$ is an effective recombination time for the trapping of free electrons into midgap traps, and, as will be seen, will determine the midgap trap recombination rate. This recombination time is given in terms of the well-electron trapping time $\tau_N = 1/\gamma_N N_A$. The interior vertical diffusion length is given by $L_D = \sqrt{\tilde{\mu}_{nz} \tilde{\tau}_n V_T}$, and the vertical drift length is given by $L_E = \tilde{\mu}_{nz} \tilde{\tau}_n E_0$. These vertical transport lengths are written in terms of the effective vertical mobility, $\tilde{\mu}_{nz}$, and the effective free-carrier lifetime, $\tilde{\tau}_n$. This lifetime can be found by considering the decay of the free-carrier densities in the dark from Eqs. (4-1) and (4-4) and is given by

$$\tilde{\tau}_n = \tau_N \left(1 + \beta_N \tau_n + \frac{1}{\beta_N \tau_N} + \frac{\tau_n}{\tau_N} \right) \quad (4-13)$$

The photogeneration rate due to the absorbed intensity is given by $g_0 = \frac{\alpha I_0}{h\nu}$. Since the trap parameters differ near the semiconductor-insulator interfaces, the carrier lifetimes vary in a stepwise manner.

Solutions to Eq. (4-12) are found in the drift-dominated regime, $L_D/L_E \ll 1$, which is typical of semiconductor materials under normal applied voltages. Using an upwind

technique [69], the solution to Eq. (4-12) along with the current density boundary conditions is given to first order in L_D/L_E as

$$n(z) = \frac{g_0 \tilde{\tau}_{Rn}^i}{1 - \alpha L_E} \left[(e^{-\alpha(z+L)} - e^{-(z+L)/L_E}) \right. \quad (4-14)$$

$$\left. + \left(\frac{\tilde{\tau}_{Rn}^s}{\tilde{\tau}_{Rn}^i} \right) \left(\frac{L_E}{L_D} \right)^2 (e^{-2\alpha L} - e^{-2L/L_E}) e^{\frac{E_0}{V_T}(z-L)} \right]$$

where $\tilde{\tau}_{Rn}^i$ is the effective electron recombination time in the interior region, and $\tilde{\tau}_{Rn}^s$ is the effective electron recombination time in the high trap density regions near the semiconductor-insulator interfaces. The interior vertical drift and diffusion lengths are given by L_E and L_D , respectively. The quasi-steady state free-hole density in a uniform internal field is similar.

The two terms in Eq. (4-14) describe two separate regions of the device. These two regions can be seen in Fig. 4-2 where the electron and hole densities are plotted for various values of the absorption and drift length. The first term in Eq. (4-14) describes the relaxation of the electron density from the upstream interface as the electrons are drawn into the device interior by the applied field. This relaxation region has a characteristic width of L_E . The second term in Eq. (4-14) describes an accumulation region as electrons collect near the semiconductor-insulator interface. The characteristic width of this accumulation region is given by V_T/E_0 and essentially represents the balance of drift and diffusion at the interface to satisfy the no-flux boundary condition on the electron current density. For positive applied voltage as shown in Fig. 4-2, electrons are pulled by the bias field from the interior and accumulate at the right interface while holes accumulate at the left.

In the relaxation region, the interior carrier distributions depend strongly on the absorption coefficient, the drift length, and the interface to which a carrier is drawn relative to the incident beam. We consider three cases in Fig. 4-2:

- $L_E \ll L$, $\alpha L \ll 1$: For very short drift lengths, the carrier densities quickly rise up from near zero at the upstream interfaces to the values determined solely by the

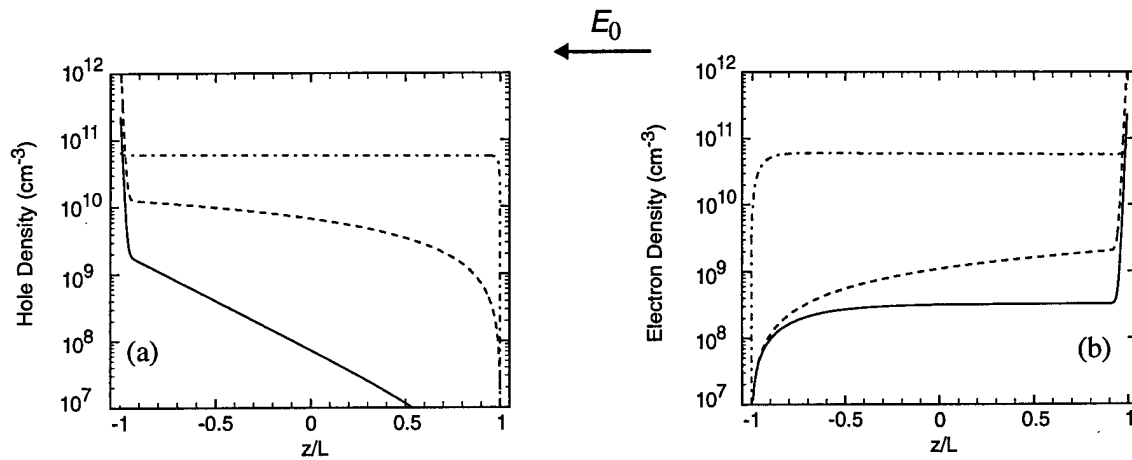


Figure 4-2 Quasi-steady state carrier distributions for (a)holes and (b)electrons at the start of the screening process showing the accumulation regions at the downstream interface and the relaxation regions throughout the interior. (a) holes with the following parameters for the solid, dashed, and dot-dashed lines, respectively: $\alpha L=3.36$, $L_E/L=8.2$; $\alpha L=0.03$, $L_E/L=8.2$; $\alpha L=0.03$, $L_E/L=0.008$. (b) electrons with the following parameters for the solid, dashed, and dot-dashed lines, respectively: $\alpha L=3.36$, $L_E/L=54$; $\alpha L=0.03$, $L_E/L=54$; $\alpha L=0.03$, $L_E/L=0.054$. Common parameters are given by: $g_0\tilde{\tau}_R^i = 6 \times 10^{10} \text{ cm}^{-3}$, $\tilde{\tau}_R^s/\tilde{\tau}_R^i = 0.1$, and $V_T/E_0 = 8.5 \text{ nm}$.

photogeneration rate. For weak absorption these values are uniform and are given by $g_0\tau_{Rn}$ and $g_0\tau_{Rp}$ for electrons and holes, respectively.

- $L_E \gg L$, $\alpha L \ll 1$: For very long drift lengths, the relaxation regions extend throughout the entire device interior. The carrier densities never fully relax to the values determined by the photogeneration rate. For low absorption, the electron and hole distributions are similar, building up throughout the interior. This monotonic buildup is due to a uniform photogeneration rate that constantly supplies new carriers throughout the interior.

- $L_E \gg L$, $\alpha L \gg 1$: For high absorption, carriers are only photogenerated near the front of the device where the photogeneration rate is high, e.g. the left interface in Fig. 4-2. In this case, the distribution of the carriers transporting to the back (electrons) and the distribution of the carriers at the front (holes) are very different. The electron density builds up from near zero at the upstream interface but then saturates in the interior since there is no photogeneration there. The hole density builds up only at the front.

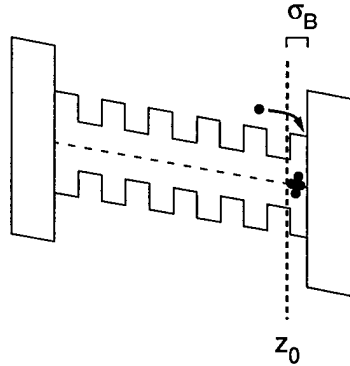


Figure 4-3 Screening in the injection model showing an interior electron injecting into the surface-charge region near the semiconductor-insulator interface where it will be trapped and screen the applied voltage. The interior edge of the surface-charge region is denoted z_0 , and the net surface charge is σ_B .

4.3 Injection Model

A basic picture of device operation can be constructed from the form of the quasi-steady state carrier distributions. As depicted in Fig. 4-3, carriers drifting toward the interfaces are injected into the accumulation regions and become trapped into the midgap traps. It can be shown from Eq. (4-14) that the space charge is dominated by the collection of carriers in traps near the semiconductor-insulator interfaces. Since most of the space charge is confined to the accumulation regions as an effective surface charge, the internal field remains uniform.

The build up of the surface charge is calculated from the trapping of free carriers in the surface-charge regions. For CW illumination, the density of the trapped charge greatly exceeds the free-carrier density. For example, the rate equation for the surface-charge density in the electron surface-charge region is

$$\frac{\partial \sigma_B}{\partial t} \equiv e \int_{z_0}^L \frac{\partial N_D^+}{\partial t} dz = e \int_{z_0}^L \left(\frac{p}{\tilde{\tau}_{Rp}^s} - \frac{n}{\tilde{\tau}_{Rn}^s} \right) dz \quad (4-15)$$

where the integration region is wide enough to include all of the accumulated electrons. From the results of the previous section, this width is several V_T/E_0 . In a properly

designed device, this width will also correspond to the width, w_s , of the surface-charge region with increased trap density. In the analysis that follows, we assume that this is the case and interchangeably refer to the surface-charge regions and the carrier accumulation regions as the same physical regions in the device near the semiconductor-insulator interfaces.

Using the free-carrier continuity equations and current density boundary conditions, Eq. (4-15) can be rewritten as

$$\frac{\partial \sigma_B}{\partial t} = j_{pz}|_{z_0} + j_{nz}|_{z_0} \quad (4-16)$$

where $j_{nz} = e\mu_{nz}nE_z$ and $j_{pz} = e\mu_{pz}pE_z$ are the current densities from the interior, neglecting diffusion. These currents are evaluated at the interior edge of the surface-charge region, z_0 , indicated in Figs. 4-1 and 4-3, and effectively only use the relaxation term of the carrier densities. The buildup of the surface charge thus arises from the net current injection from the interior.

In the above analysis it has been implicitly assumed that the traps remain unsaturated and that the lifetimes remain constant. Practically, this requires that the net trap density in the surface-charge regions be large enough to fully screen the applied voltage. For example, to fully screen 50 kV/cm in a device with the following parameters: $L = 1.0 \mu\text{m}$, $d = 0.2 \mu\text{m}$, $\epsilon_1 = 13\epsilon_0$, and $\epsilon_2 = 5\epsilon_0$, the amount of surface charge required is $1 \times 10^{12} \text{ cm}^{-2}$. In this work, N_D^s is always selected to prevent trap saturation.

4.4 Field Screening

The screening of the internal electric field can now be calculated self-consistently by considering the field produced by the applied voltage and the screening charge. Assuming $\sigma_A = -\sigma_B = \sigma_0$, as dictated by charge neutrality, the internal field, E_z , is given in terms of the unscreened applied field,

$$E_0 = \frac{V_0}{2L\left(1 + \frac{\epsilon_1 L}{\epsilon_2 d}\right)}, \quad (4-17)$$

and the surface charge by

$$E_z = \chi_0 \sigma_0 - E_0 \quad (4-18)$$

where

$$\chi_0 = \left[\epsilon_1 \left(1 + \frac{\epsilon_2 L}{\epsilon_1 d} \right) \right]^{-1} \quad (4-19)$$

From Eq. (4-16), the rate equation for the internal field is

$$\frac{\partial E_z}{\partial t} = -e\chi_0(\mu_{nz}n(z_0) + \mu_{pz}p(z_0))E_z \quad (4-20)$$

The resulting screening response can be characterized in terms of the vertical drift lengths and the absorption coefficient. We consider two regimes: a short drift length regime in which the vertical drift length is shorter than the device length, and a long drift length regime in which the vertical drift length is longer than the device length. For both regimes, the decay of the internal field is computed, and an analytical estimate of the initial screening rate is given.

4.4.1 Short Drift Lengths

For short drift lengths ($L_E \ll L$), the injecting carrier densities are given by the photogeneration term since the relaxation region is so short. We consider only the low absorption case since the combination of high absorption and short drift lengths results in a device with poor screening behavior.

For short drift lengths and low absorption, the interior carrier densities are given by $n|_{z_0} = g_0 \tilde{\tau}_{Rn}$ and $p|_{z_0} = g_0 \tilde{\tau}_{Rp}$. The rate equation for the internal field can then be written as

$$\frac{\partial E_z}{\partial t} = -\frac{E_z}{\tau_0} \quad (4-21)$$

where

$$\tau_0 = [\chi_0(e\tilde{\mu}_{nz}g_0\tilde{\tau}_n + e\tilde{\mu}_{pz}g_0\tilde{\tau}_p)]^{-1} \quad (4-22)$$

With the initial condition $E_z = -E_0$, the solution to Eq. (4-21) is

$$E_z = -E_0 e^{-t/\tau_0} \quad (4-23)$$

This result describes screening as occurring via dielectric relaxation in which the field decays exponentially with a time constant given by τ_0 . This time constant is modified from the standard dielectric relaxation time of $\epsilon_1 / (e\tilde{\mu}_{nz}g_0\tilde{\tau}_n + e\tilde{\mu}_{pz}g_0\tilde{\tau}_p)$ by the capacitive coupling of the applied voltage. Field screening in this regime can also be represented by a simple equivalent circuit made of passive components [15].

4.4.2 Long Drift Lengths

For large vertical drift lengths ($L_E \gg L$), the trapping of a particular carrier, either electron or hole, dominates the space charge in that carrier's accumulation region. For example, the trapping of electrons at the right interface in Fig. 4-2 dominates the space charge there. In addition, the assumption of antisymmetric surface charge used to develop the previous formalism can be shown to be valid for the case of very large drift lengths. Here we examine cases slightly outside of this regime, but still use the previous results to give an indication of the types of screening behavior that can be obtained. Direct numerical solutions to the transport equations can be used to obtain exact results for intermediate regimes.

Assuming the electron and hole responses are the same, the field rate equation is:

$$\frac{\partial E_z}{\partial t} = -e\mu_{nz}\chi_0 n(z_0)E_z \quad (4-24)$$

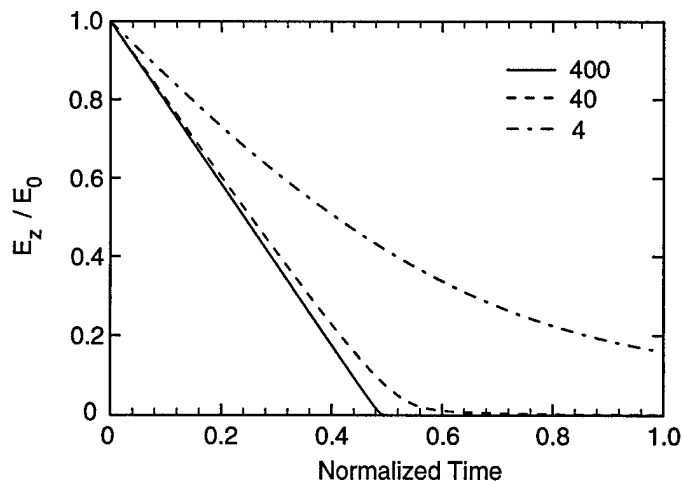


Figure 4-4 Screening of the internal field for three values of the initial vertical drift length: $L_E/L = 4, 40, 400$. Time is normalized to twice the screening time for $L_E/L = 400$.

For large vertical drift lengths, the carrier densities are themselves functions of the field as shown in Eq. (4-14). The resulting nonlinear system must be solved numerically with the following initial condition: $E_z = -E_0$. The solutions can be characterized in terms of the initial vertical drift length, L_E , and absorption coefficient, α .

Solutions to Eq. (4-24) are shown in Fig. 4-4 for various values of the initial vertical drift length at $\alpha = 2.0 \times 10^4 \text{ cm}^{-1}$. To compare time scales, E_0 is held constant and the vertical mobility-lifetime product is varied to obtain different vertical drift lengths. For large vertical drift lengths the field decays at a constant rate. As can be seen from Eqs. (4-14) and (4-24), this is due to saturation of the internal current densities. In this regime, all photogenerated carriers are able to drift to the surface-charge regions without being trapped by midgap traps in the interior, producing a response that is limited only by the photogeneration rate. For smaller vertical drift lengths, the response slows as carriers are trapped multiple times in the interior as they drift to the surface-charge regions. This produces a response that is transport-limited, and at very small vertical drift lengths the response approaches exponential screening through dielectric relaxation as previously discussed. The transition between the photogeneration-limited and transport-limited regimes occurs when the vertical drift length in the interior approaches the device length. This transition can be seen near the end of the screening process for the $L_E/L = 40$ case in Fig. 4-4.

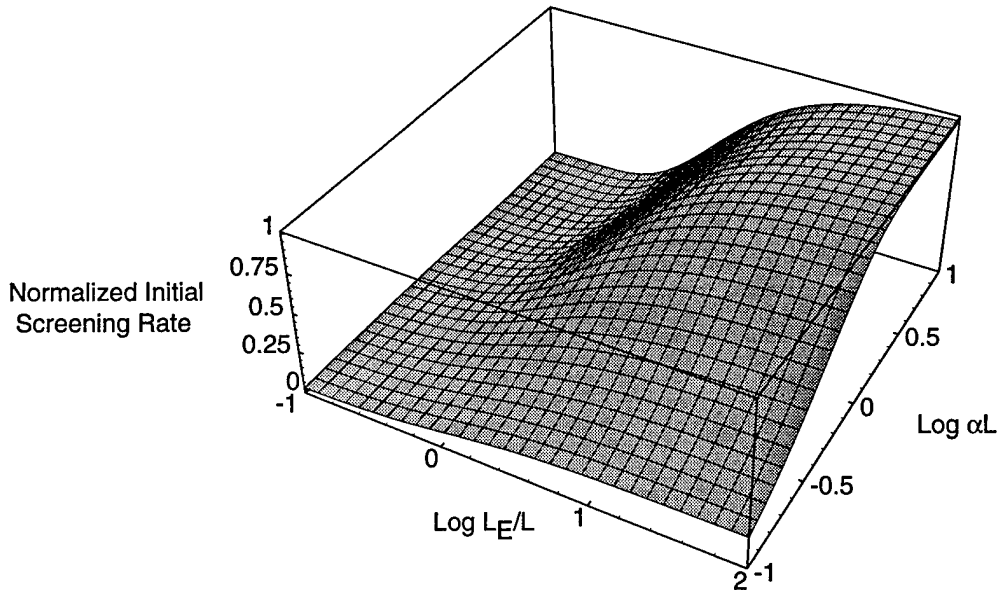


Figure 4-5 Normalized initial screening rate as a function of the vertical drift length and absorption coefficient. Maximum device speed is obtained for large vertical drift lengths and large absorption coefficients.

4.4.3 Initial Rate

The maximum field screening rate from Eq. (4-24) is given by $e\chi_0 I_0/h\nu$. As an example, the maximum screening rate for a device with $L = 1.0 \mu\text{m}$, $d = 0.2 \mu\text{m}$, $\epsilon_1 = 13\epsilon_0$, $\epsilon_2 = 5\epsilon_0$ under an incident intensity of 10 mW/cm^2 at 850 nm is $2 \text{ kV/cm}\cdot\mu\text{s}$. It would thus take $\sim 25 \mu\text{s}$ to screen a typical applied field of 50 kV/cm . The initial screening rate, assuming equal electron and hole contributions, can be calculated for arbitrary L_E and α from Eqs. (4-14) and (4-24) as

$$\left. \frac{\partial E_z}{\partial t} \right|_{t=0} = e\chi_0 \frac{I_0}{h\nu} \left(\frac{\alpha L_E}{1 - \alpha L_E} \right) (e^{-2\alpha L} - e^{-2L/L_E}) \quad (4-25)$$

where $z_0 \approx L$ in the evaluation of the relaxation term of the electron density.

As summarized by the plot of Eq. (4-25) in Fig. 4-5, operating at the maximum screening rate requires large vertical drift lengths and high absorption. This can be achieved by using moderately doped or intrinsic material to obtain long carrier lifetimes, and by using shallow quantum wells to obtain good emission rates and large effective

$L = 1.0 \mu\text{m}$	$d = 0.2 \mu\text{m}$
$\epsilon_1 = 13\epsilon_0$	$\epsilon_2 = 4.5\epsilon_0$
$I_0 = 10 \text{ mW/cm}^2$	$\alpha = 2.0 \times 10^4 \text{ cm}^{-1}$
$N_D^i = 2 \times 10^{16} \text{ cm}^{-3}$	$N_D^s = 2 \times 10^{19} \text{ cm}^{-3}$
$N_A^i = 1 \times 10^{16} \text{ cm}^{-3}$	$N_A^s = 1 \times 10^{19} \text{ cm}^{-3}$
$V_0 = 20 \text{ V}$	$w_s = 50 \text{ nm}$

Table 4-1 Device parameters used in the simulations. Values are typical of MQW-OASLM's like the one described in section 2.2. In particular, note the interior and surface densities of midgap traps which are used to model a moderately doped interior and low-temperature grown interface regions.

mobilities. Operating near the peak of the exciton absorption or in a non-degenerate wavelength configuration to maximize the photogeneration rate is also desirable.

4.5 Numerical Results

In this section we examine some of the details of the screening process using direct numerical solution of the transport equations and assess the validity of the main approximations used in the development of the injection model previously described. The two main approximations used in the development of the injection model are the assumption that the space charge is confined to the semiconductor-insulator interfaces as an effective surface charge and that the electron and hole responses are the same. To investigate the validity of these approximations, field screening was simulated in a device with the parameters listed in Table 4-1 and the following transport parameters: an *effective* electron mobility of $64 \text{ cm}^2/\text{V}\cdot\text{s}$, an *effective* hole mobility of $18 \text{ cm}^2/\text{V}\cdot\text{s}$, *effective* interior free-carrier lifetimes of 3 ns, and an *effective* surface carrier lifetime of 10 ps. As described in section 4.2, these *effective* parameters describe carrier transport in the shallow trap model

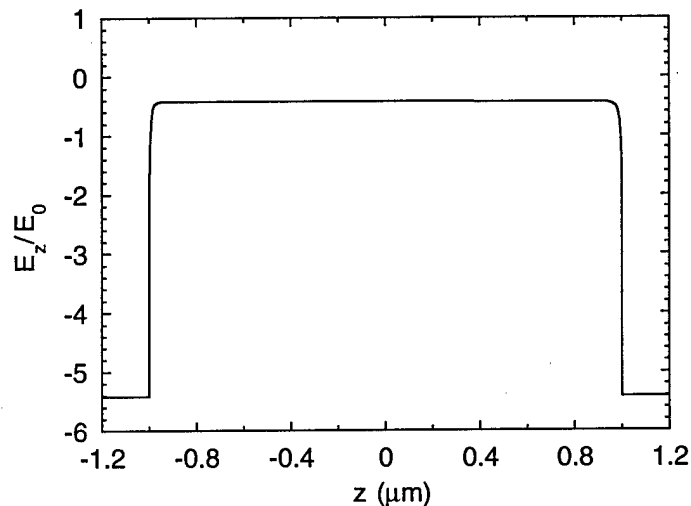


Figure 4-6 Interior field distribution showing good uniformity. Most of the variation occurs near the semiconductor-insulator interfaces in the surface-charge regions.

for quantum wells. These parameters were chosen from typical values for AlGaAs transport and quantum-well properties [70, 71], and from carrier escape calculations in Chapter 3.

We first examine the uniformity of the interior field. In Fig. 4-6, the vertical profile of E_z along the device length is shown midway through the screening process. The profile is quite uniform, with most of the variation occurring in the surface-charge regions near the interfaces. This supports the basic surface charge picture presented above.

To examine the validity of the screening results calculated using the injection model with equal surface-charge screening rates for electrons and holes, field screening using the device parameters above was computed using the injection model and simulated using direct numerical solutions to the transport equations. A comparison of the results in Figure 4-7 shows that the computed responses agree quite well, with the small discrepancy attributable to the different electron and hole parameters. For the injection model calculation, an electron/hole mobility-lifetime product of $2.0 \times 10^{-7} \text{ cm}^2/\text{Vs}$ was used. The agreement in Fig. 4-7, especially at short times, indicates that Eq. (4-24) is indeed a good estimate of the screening rate for typical parameters.

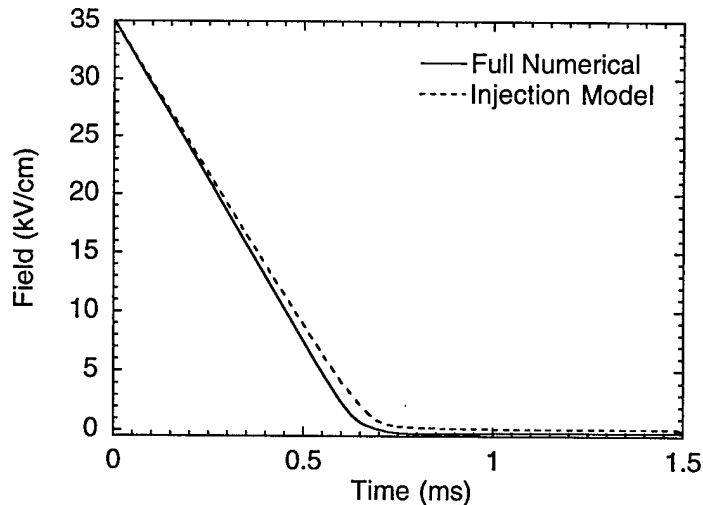


Figure 4-7 Comparison of the screening responses calculated using the injection model and full numerical solutions to the transport equations. The discrepancy as the field decays to zero is attributed to the different electron and hole transport parameters which the injection model does not consider.

4.6 Semiconductor and Quantum-Well Effects

There are a number of unique effects that occur in semiconductor and quantum-well materials that we have neglected up to this point but which can have a large impact on transport behavior. These effects include velocity saturation, resonant absorption, QCSE absorption, and field dependent carrier emission from the quantum wells. The impact of each of these effects can be considered within the framework of the injection model.

The saturation of the drift velocity of electrons in bulk GaAs in fields above 4 kV/cm is a well known phenomenon [66]. Holes also display drift velocity saturation at larger fields. Drift velocity saturation describes the crossover of the drift velocity from linear behavior at low fields to a saturated value at high fields. In bulk GaAs at room temperature, this saturation effect is caused by increased phonon scattering as the carriers gain kinetic energy from the field and from k -space transfers to different parts of the Brillouin

$\mu_{nz} = \frac{\mu_{nz}^0}{1 + \mu_{nz}^0 E_z / v_{sat}^n}$	$\mu_{pz} = \frac{\mu_{pz}^0}{1 + \mu_{pz}^0 E_z / v_{sat}^p}$
$\mu_{nz}^0 = 2000 \text{ cm}^2/\text{Vs}$	$\mu_{pz}^0 = 150 \text{ cm}^2/\text{Vs}$
$v_{sat}^n = 1.0 \times 10^7 \text{ cm/s}$	$v_{sat}^p = 1.0 \times 10^7 \text{ cm/s}$

Table 4-2 Velocity-saturated mobilities. The low field mobilities and saturation velocities are typical of AlGaAs alloys. The simple functional dependence of the mobilities is typical of velocity-saturated mobilities for holes in bulk GaAs.

zone that have lower mobilities. The exact form of velocity saturation in MQW materials, however, is not so well understood. Recent studies at moderate fields ($< 30 \text{ kV/cm}$) show no clear signs of velocity saturation [72] while studies at higher fields show clear evidence of velocity saturation [50]. For vertical transport, velocity saturation serves to limit the vertical drift length. Depending on the quantum-well escape rates and the carrier lifetimes, the screening response can be pushed into the transport-limited regime if the saturated drift velocity is small enough.

The simplest way to incorporate velocity saturation into the drift-diffusion model is to use a field dependent mobility [64]. As an example, Table 4-2, gives a relatively simple velocity saturation model in which the low field mobilities are constant while the high field mobilities go like $1/E$ where E is the field. The values for the low field mobilities and the saturated drift velocities are typical of bulk GaAs [70, 76]. The functional dependence of the hole mobility on the field is also typical of bulk GaAs. The electric field dependence of the electron mobility, however, is a simplification of the bulk GaAs mobility, and while it does not include negative differential resistance at low fields, the high field behavior is similar to that of the bulk GaAs mobility.

Figure 4-8 shows the screening response calculated using the mobilities from Table 4-2 and the device parameters from Table 4-1. For comparison, the screening

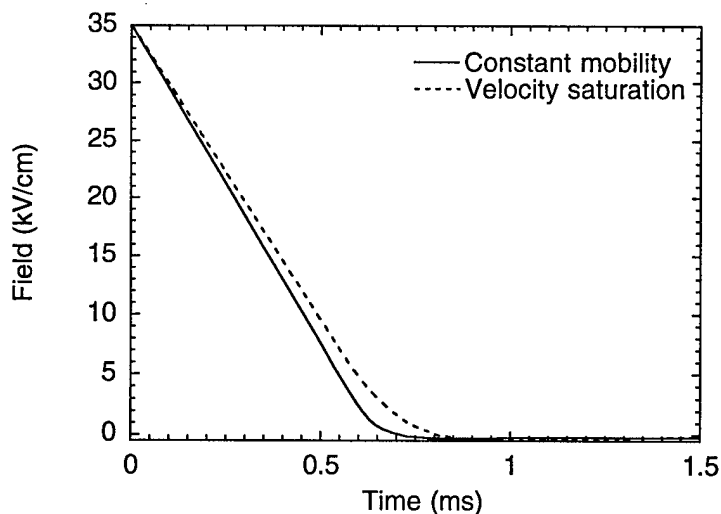


Figure 4-8 Comparison of field screening calculated using constant mobilities and velocity-saturated mobilities. In this example, the long carrier lifetimes and large effective mobilities keep the velocity-saturated response in the photogeneration-limited regime.

response calculated using constant mobilities is also shown. Since the effective carrier lifetimes are sufficiently long and the effective carrier mobilities are sufficiently high in this example, the velocity-saturated screening response still follows the basic photogeneration-limited behavior. As long as the vertical drift lengths remain much longer than the device length, the initial screening response will be fairly insensitive to the actual mobility values. We will see in later chapters that the main effect of velocity saturation is on the resolution performance.

The presence of quantum wells presents a number of new transport properties in addition to those of bulk transport. We have already considered the effective carrier lifetimes and mobilities due to the escape from and capture by the wells. Another property of quantum-well transport is the ability to photogenerate well carriers through resonant absorption between valence and conduction subbands. The injection model can be straightforwardly modified to include resonant absorption instead of non-resonant absorption across the barrier bandgap. This requires moving the photogeneration term from the free-carrier continuity equations to the well-carrier continuity equations. The field screening results found

with these modifications are actually the same as those found for non-resonant absorption, except that the effective photogeneration rate for free electrons is

$$\tilde{g}_n = \left(\frac{\beta_N \tau_N}{1 + \beta_N \tau_N} \right) g_0 \quad (4-26)$$

(The result for holes is similar.) This is essentially the resonant photogeneration rate multiplied by the escape probability of a well-confined electron. For small escape rates, this reduces the generation of free electrons and hence the screening rate.

Another unique quantum-well property is the quantum confined Stark effect, which is used primarily as an electro-optic effect as discussed in Chapter 3. However, since it produces a field dependent absorption coefficient for resonant illumination, it directly affects the photogeneration rate. The effect on the actual screening rate, however, depends on the absorption length. For low absorption, the screening rate given from Eq. (4-25) is directly proportional to the absorption coefficient, and thus the changing QCSE absorption will result in a constantly changing response rate. For high absorption, however, the screening rate is independent of the absorption coefficient, and as long as the absorption remains high throughout the screening process, device operation will be unaffected by the QCSE.

The final quantum-well property we consider is the field dependence of the carrier escape rates from the quantum wells. As discussed in Chapter 3, the thermionic emission and tunneling rates depend strongly on the field. For example, the electron escape rate shown in Fig. 3-9 decreases by almost two orders of magnitude as the field is reduced from 100 kV/cm to 40 kV/cm. For typical parameters, the effective carrier mobilities depend linearly on the carrier escape rates as shown in Eq. (4-11). Therefore, a drastic reduction in the escape rate could plunge the device into the transport-limited regime and slow down the screening response.

4.7 Summary

In summary, we have developed a one-dimensional drift-diffusion model to simulate the screening of the internal electric field in a MQW-OASLM. Quantum wells were included explicitly using a shallow trap model and were shown to partly determine the operating regime through the effective free-carrier mobilities and lifetimes. Analytical calculations of the quasi-steady state carrier distributions were shown to justify the often used surface-charge picture of device operation. The separation of the carrier distributions into relaxation and thin accumulation regions was used to develop an injection model of device operation. In this model, screening occurs through the injection of interior carriers into thin surface-charge regions near the semiconductor-insulator interfaces. Using this model, two screening regimes were identified: transport-limited and photogeneration-limited. For vertical drift lengths shorter than the device length (transport-limited), screening proceeds via dielectric relaxation. The maximum screening rate, however, is obtained for long vertical drift lengths (photogeneration-limited) where the field screens down at a constant rate.

Chapter 5

Transmission and Photocurrent Response

The most common technique used to investigate screening behavior in quantum-well devices is the measurement of the optical transmission at wavelengths resonant with the quantum confined Stark effect. Assuming the field dependence of the QCSE is known, the internal field can be extracted from the measured transmission through an inversion process. Variations of this technique has been used to study a number of interesting topics in quantum-well devices including carrier escape from wells [65], short-pulse screening [73], and the speed response of optical modulators [74].

The primary advantage of measuring the optical transmission is that it provides a simple, indirect way of determining the behavior of the internal field, which is typically the quantity of interest when designing optical modulators. One of the main drawbacks of this technique, however, is that, to lowest order, the QCSE is quadratic in the field and therefore has poor differential sensitivity at low fields. In the MQW-OASLM this can be problematic since the internal field is expected to be fully screened. The transmission is not the only means of characterizing screening behavior, however. During the screening process, a transient photocurrent flows as the internal space charge is created. This photocurrent is a displacement type of current and is linear in the time derivative of the internal field, providing better sensitivity at low fields.

In this chapter we compare experimentally measured screening behavior to the screening response calculated using the device model presented in the previous chapter. Both the

transmission and photocurrent are used to determine the electric field screening rate, examine the polarity dependence of device operation, and demonstrate the characteristic responses of the photogeneration-limited and transport-limited regimes described in the previous chapter. For the device simulation, realistic device parameters from the literature and the carrier escape calculations in Chapter 3 are used. In general, very good qualitative agreement is found. In addition, a number of more subtle transport effects, including the relative contribution of each of the carriers to the screening process and the effect of velocity-saturated carrier mobilities on the photocurrent, are examined.

5.1 Experiment

The only experimental investigation of the response of a MQW-OASLM under uniform illumination has been presented by Partovi *et al.* [6] who measured the transmission as a function of the frequency of an applied square wave voltage. The response at only one voltage amplitude was measured. In addition, comparing frequency dependent measurements to intensive time-domain simulations is not very convenient. In this section we summarize time dependent measurements that we have performed on the sample described in Fig. 2-5. The experiments involved applying a bipolar square wave voltage to the sample and measuring the resonant transmission and photocurrent responses. Each transition of the square wave initiated a new screening processes as photogenerated carriers were driven to the opposite interface. This presented a convenient way of studying the screening response for both polarities as well as for various amplitudes of the applied voltage.

The photocurrent that flows during the screening process is a displacement type of current. It can be viewed as the residual charging current that is required to maintain a constant voltage across the device as the internal space charge is created. Assuming the device structure is symmetric, this photocurrent is related to the internal voltage created by the screening charge, V_{scr} as

$$I = -\frac{C_b \partial V_{scr}}{2 \partial t} \quad (5-1)$$

where C_b is the capacitance of the insulating layers. This capacitance is determined by the illuminated area of the sample. The photocurrent is linearly proportional to the time derivative of the screening-induced voltage and thus provides extra sensitivity to the screening dynamics.

5.1.1 Setup

Figure 5-1 shows the experimental setup used to simultaneously measure the transmission and photocurrent. The sample was illuminated with a HeNe laser operating at a wavelength of 632.8 nm. The HeNe beam was spatially filtered and expanded to provide a uniform beam profile. A square aperture with an area of 7 mm^2 was placed in front of the sample to give a well defined area for the photocurrent calculations. HeNe at 632.8 nm was chosen as the photogenerating wavelength since its absorption coefficient of $3 \times 10^4 \text{ cm}^{-1}$ is quite high and thus useful for separating the relative contributions of the carriers in the screening process. The modeling is also simplified since this wavelength is not resonant with the QCSE, and the stability and low drift of the intensity allow the direct comparison of results taken over several hours.

The sample was driven by a bipolar square wave applied voltage from a function generator with no DC offset. The drive frequency was set low enough to allow the screening process to run to completion during each half period. The polarity convention used in the experiment and in the analysis is indicated in Fig. 5-1 in which the front of the sample relative to the incident beam was connected to the ground path.

The transmission of the sample was measured with an IR probe beam from a lamp/monochromator arrangement. The quartz-halogen lamp and monochromator provided a convenient source of low power, tunable IR wavelengths. The lamp was also very stable which allowed for easy normalization of the transmission from run to run. To reduce stray light, a box was placed around the input path to the monochromator, and an IR passing filter was placed in front of the detector. A silicon photodiode/amplifier combination with a gain of $1.2 \times 10^7 \text{ V/W}$ and a bandwidth of 35 kHz was used to measure the transmitted IR beam. A schematic of the amplifier is shown in the appendix to this chapter.

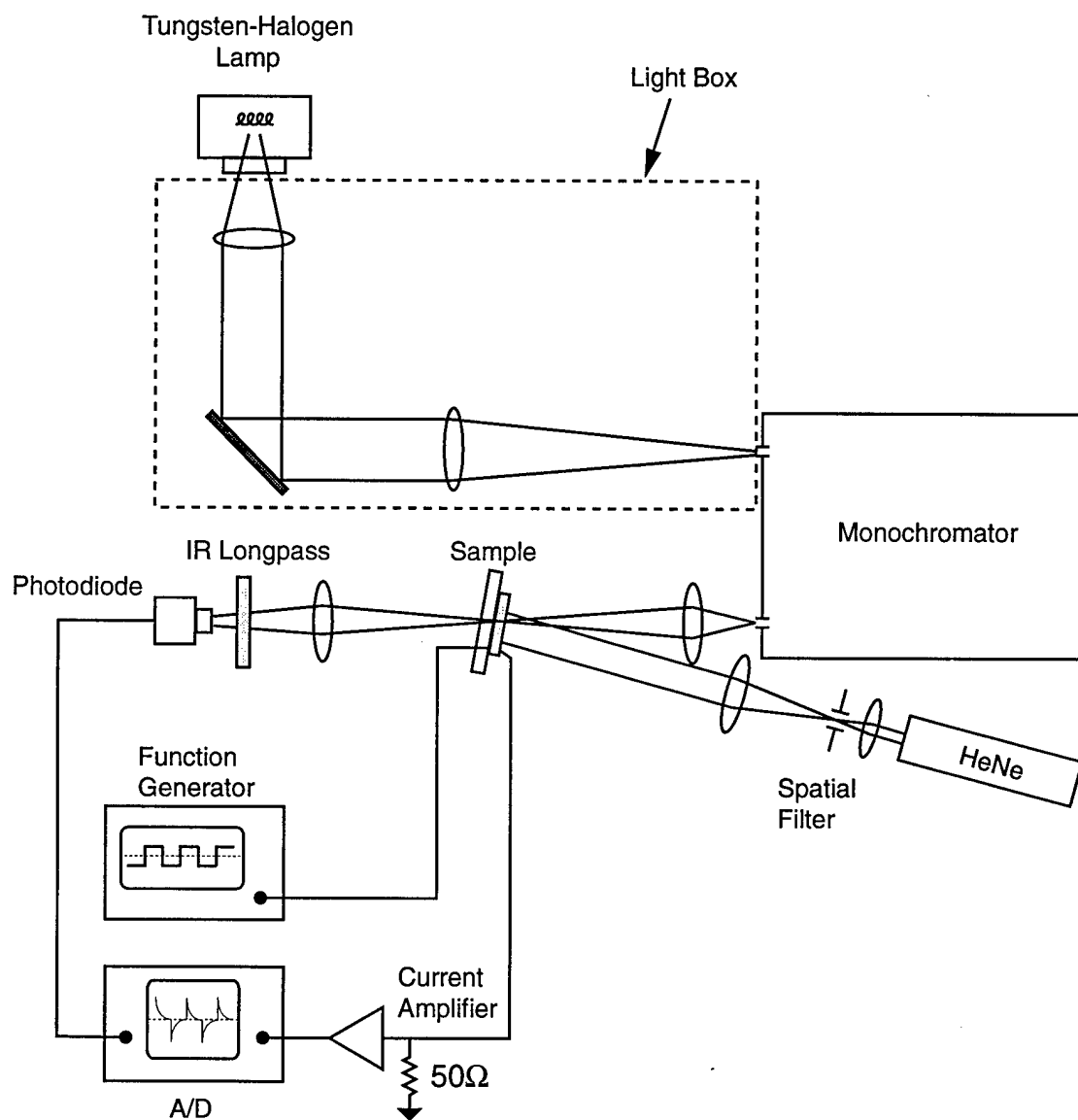


Figure 5-1 Experimental setup for measuring the transmission and photocurrent. The sample is illuminated by a spatially filtered and expanded HeNe beam to photogenerate carriers. The transmission of an IR probe beam from the lamp/monochromator arrangement is measured with a photodiode/amplifier combination. The sample is driven with a bipolar square wave voltage from the function generator, and the return path to ground is through a 50 Ω resistor through which the photocurrent is measured. As a polarity convention, the front of the sample relative to the incident HeNe beam is taken as the grounded side.

The photocurrent was measured through a $50\ \Omega$ series resistor in the return path to ground. Each half period of the applied square wave produced a current signal with two components. The first component is due to the charging of the total device capacitance immediately after the polarity is switched. The time constant for this charging process is given by the series resistance of the current measurement resistor and the output impedance of the function generator, and the device capacitance. The device capacitance was $1.2\ \text{nF}$, and for the parameters used in this setup, the RC time constant was $122\ \text{ns}$.

The charging component is followed by a much smaller and more slowly developing signal that is due to the displacement current produced during the screening process. The magnitude of this current component can be 100 times smaller than the charging transient. To measure the screening component without overloading the downstream electronics with the charging transient, output clamping amplifiers were used. The schematics for these amplifiers are also shown in the appendix to this chapter. The total current signal that was measured thus consisted of the sum of the screening current and a clamped version of the charging transient. To remove the charging transient and any background bias signal, the dark response measured without HeNe illumination was subtracted from the response measured with HeNe illumination. It should be noted that the resulting current signal during the period of the charging transient (the first $0.5\ \mu\text{s}$) cannot be reliably used as an indicator of the screening component since the voltage across the sample is constantly changing.

The outputs of the photodiode/amplifier combination and the current amplifier were sampled using a LeCroy Model 6810 Waveform Recorder. This is a 12 bit A/D system with a bandwidth of $2.5\ \text{MHz}$ and a maximum sampling rate of $2\ \text{Msamples/s}$. Typically, the average of 100 consecutive periods was calculated to improve the signal to noise ratio.

5.1.2 Transmission Results

In order to extract the screening behavior of the internal field from the transmission measurements, it is first necessary to calibrate the transmission change induced by the QCSE. This then allows the measured transmission values to be converted into internal field

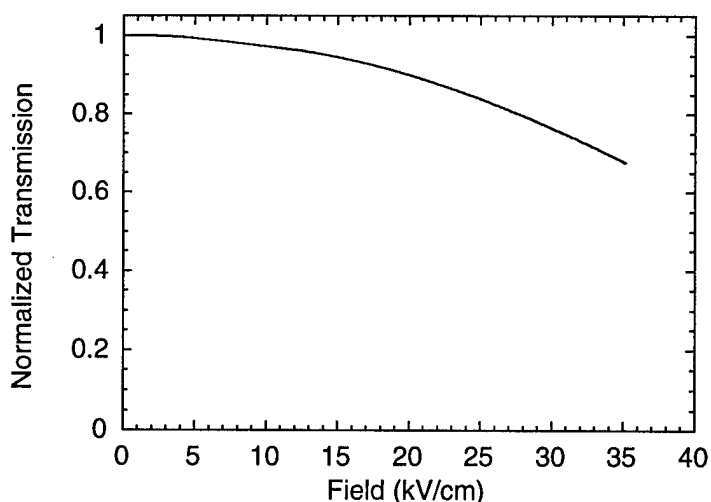


Figure 5-2 Transmission as a function of internal field due to the QCSE without screening. The transmission is normalized by the zero field value. This curve is used to convert the measured transmission during screening into internal field values.

values. This calibration was performed by measuring the transmission of the IR probe beam without HeNe illumination as a function of the applied voltage. The IR beam had a power of 100 nW and was tuned to the peak of the QCSE differential transmission at 852 nm with a monochromator resolution of 1 nm FWHM. For this measurement, the sample was driven by a bipolar sawtooth applied voltage at 200 Hz to provide a convenient means of scanning through the desired voltage range. An alternating applied voltage is required since a DC voltage would eventually become screened by thermal generation and by optical generation from the IR probe beam. A measurement of the transmission with a square wave applied voltage at 200 Hz showed no evidence of screening effects, indicating that any screening contributions from thermal or IR generation were negligible during the time scales of the experiment. The calibration of the QCSE obtained after converting the applied voltage to electric field and normalizing the transmission by the zero field value is shown in Fig. 5-2.

For the actual screening measurements, the transmission under HeNe illumination at an intensity of 1.6 mW/cm^2 was measured for both polarities and various amplitudes of the applied square wave voltage at a drive frequency of 200 Hz. The IR probe wavelength

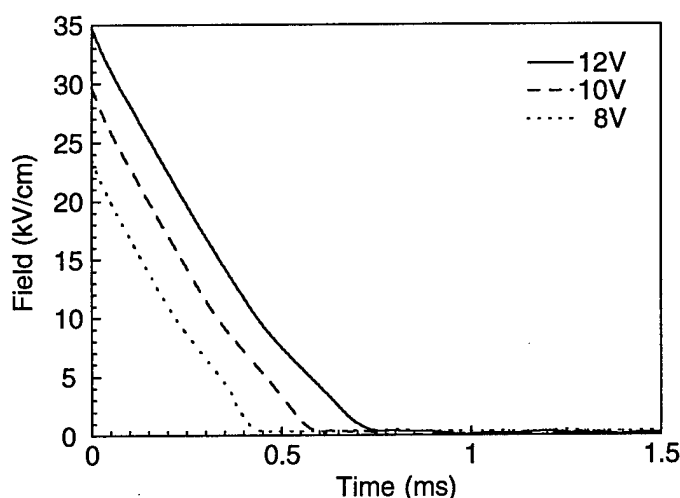


Figure 5-3 Screening of the internal electric field as determined from the measured transmission for the indicated peak-to-peak applied voltages during the positive half-period of the applied voltage. The time origin occurs at the switching of the applied voltage from negative to positive polarity.

and power were the same as used is the QCSE calibration. The transmission under short circuit conditions was used to normalize the resulting transmission curves, and the QCSE transmission calibration from Fig. 5-2 was then used to find the corresponding field values.

The results for three applied voltage amplitudes during the half period of positive polarity of the driving voltage are shown in Fig. 5-3. For all applied voltages, the initial decay is very linear at a rate of 55 kV/cm·ms. Also, for all applied voltages the internal field is completely screened down to zero. This indicates that the insulating barriers are confining the carriers to the interior region as desired. If there were significant and continuous leakage through the barriers, the screening would be incomplete since the voltage drop across the device would be divided between the semiconductor and insulator regions in proportion to their effective resistivities [14]. As the photocurrent response will show, however, there does appear to be a small amount of leakage current flowing at larger applied voltages. The transmission measurements, however, indicate that this current is not large enough to prevent complete screening.

The completeness of the screening also indicates that the trap density at the semiconductor-insulator interfaces is sufficient to hold the screening charge without saturating. If the traps were saturated or there were significant bulk charge, the screening could not run to completion, and the field would not decay in a linear fashion.

The initial screening rate was also measured as a function of incident intensity from 1 mW/cm^2 to 10 mW/cm^2 and was found to be linear. This is in general agreement with the results of Chapter 4.

Implicit in the conversion process from transmission to internal field is the assumption that the internal field is uniform within the quantum-well region. The extreme linearity of the field decay, the completeness of the screening process, and the surface-charge modeling results from Chapter 4 indicate that this is an accurate assumption.

5.1.3 Photocurrent Results

As indicated in Eq. (5-1), the photocurrent is proportional to the time derivative of the internal voltage and thus provides better sensitivity than the transmission to the screening dynamics. This additional sensitivity is especially useful in examining the approach to full screening. The details of the screening behavior in this low field region are essentially lost in the transmission measurements.

The photocurrent response under the same illumination conditions as for the transmission results are shown in Fig. 5-4 for a more complete set of applied voltages at positive polarity. For low voltages, the response decays quickly. For large voltages, the response consists of three regions: a fast initial transient, a plateau, and finally a decay. The fast initial transient was not seen in the transmission data and may be due to some form of transient leakage current. In the plateau region, the initial photocurrent saturates for large voltages. From Eq. (5-1), this indicates that the decay of the internal voltage, and hence field, is linear. This agrees with the results of the transmission measurement. The time for the onset of the photocurrent decay depends approximately linearly on the applied voltage while the time scale for the actual decay appears to be independent of the applied voltage.

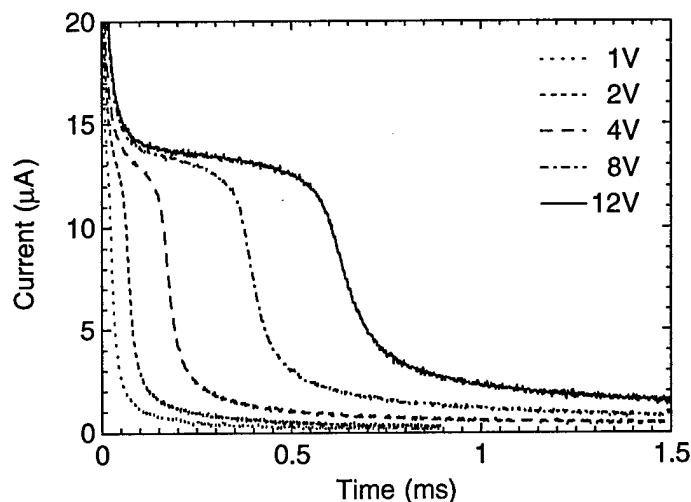


Figure 5-4 Measured photocurrent for the indicated peak-to-peak applied voltages, positive polarity. The time origin occurs at the switching of the applied voltage to positive polarity.

At longer times, the photocurrent response shows an offset which may also be due to leakage currents.

The photocurrent response also depends on the polarity of the applied voltage as shown in Fig. 5-5 where the photocurrent for positive and negative half-periods of the applied voltage are shown for two peak-to-peak voltages. In Fig. 5-5a, the response with a relatively low peak-to-peak applied voltage of 4 V is shown. The photocurrent responses for the two polarities are asymmetric with a slightly faster response obtained for positive polarity. This polarity draws electrons to the back of the device relative to the incident beam. This can be compared to the result for a larger peak-to-peak voltage of 12 V, shown in Fig. 5-5b, for which the negative polarity displays an initially faster response.

Similar differences in the transmission results were also seen as a function of polarity, although they were not as pronounced as those seen in the photocurrent results. This suggests that, although there may be some leakage current present in the photocurrent measurements, the differences in the photocurrent responses as a function of polarity are due to screening effects and not to excess leakage current. We have also examined one sample in which no initial fast transients were seen, yet similar asymmetries due to polarity were still present.

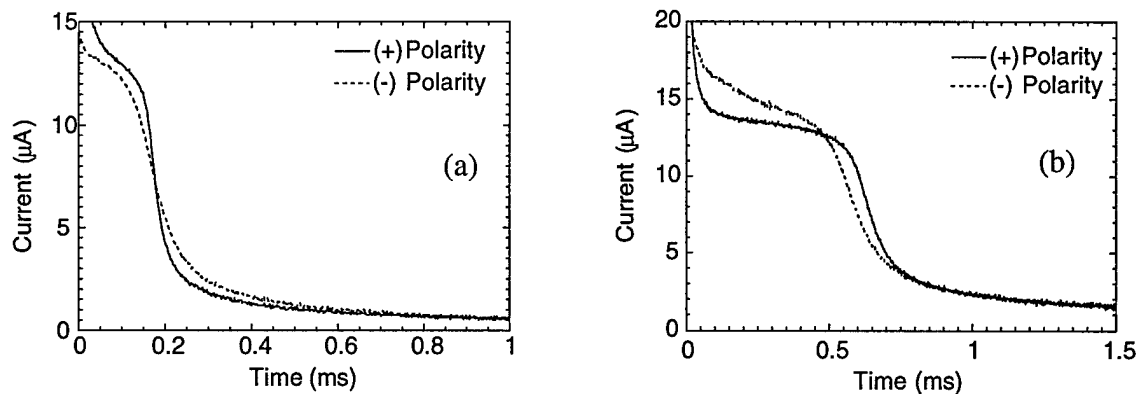


Figure 5-5 Measured photocurrent response for both polarities of the applied voltage for a peak-to-peak voltage of (a) 4 V and (b) 12 V. The negative polarity response has been inverted for comparison.

5.2 Simulation

The transient decay of the internal field and the displacement photocurrent can be calculated using the device model presented in the previous chapter. In order to consider the complete screening response and also nonlinear transport effects such as velocity saturation, we use direct numerical solutions to the transport equations. The field decay is used to compare simulated and measured screening rates, and the photocurrent response is used to examine some of the more subtle transport behavior. Of particular interest is the asymmetry of the photocurrent response for various polarities and amplitudes of the applied voltage.

5.2.1 Device Model

Field screening was simulated using the 1D device model described in Chapter 4 with the parameters listed in Table 5-1. These parameters were taken from the literature, from the results of the carrier escape calculations in Chapter 3, and from the device geometry shown in Fig. 2-5. In the simulation, the device geometry consisted of a 2.09 μm quantum-well region, a bulk-like 1500 Å etch stop region, and 50 nm surface-charge regions

	<p>Constant mobilities:</p> $\mu_{nz}^0 = 2000 \text{ cm}^2/\text{Vs}$ $\mu_{pz}^0 = 150 \text{ cm}^2/\text{Vs}$
$I_0 = 1.6 \text{ mW}/\text{cm}^2 \quad \alpha = 3.0 \times 10^4 \text{ cm}^{-1}$ $N_D^i = 2 \times 10^{16} \text{ cm}^{-3} \quad N_A^i = 1 \times 10^{16} \text{ cm}^{-3}$ $N_D^s = 2 \times 10^{19} \text{ cm}^{-3} \quad N_A^s = 1 \times 10^{19} \text{ cm}^{-3}$ $\tau_n = 1 \text{ ps} \quad \tau_p = 1 \text{ ps}$ $\tau_N = 3 \text{ ns} \quad \tau_P = 3 \text{ ns}$ $\beta_N = 2.5 \times 10^{10} \text{ s}^{-1} \quad \beta_P = 1.3 \times 10^{11} \text{ s}^{-1}$	<p>Velocity saturated mobilities:</p> $\mu_z = \frac{\mu_z^0}{1 + \mu_z^0 E_z / v_{sat}}$ $\mu_{nz}^0 = 2000 \text{ cm}^2/\text{Vs}$ $\mu_{pz}^0 = 150 \text{ cm}^2/\text{Vs}$ $v_{sat}^p = v_{sat}^n = 1.0 \times 10^7 \text{ cm/s}$

Table 5-1 Parameters used in the simulations. The absorption and intensity values are from experimental results, the emission rates from calculations in Chapter 3, and the remaining parameters are from literature values described in the text.

near the semiconductor-PSG interfaces to model interface traps and traps created from low temperature quantum-well growth. The dielectric permittivities were those of PSG and a spatial average of the permittivities for the GaAs/Al_{0.29}Ga_{0.71}As quantum-well region. The well emission rates, β_N and β_P , were calculated for a 100 Å-GaAs/35 Å-Al_{0.29}Ga_{0.71}As quantum-well system, and are the same as the results in Chapter 3. The lifetimes, τ_N and τ_P , for well carriers being trapped by the midgap traps were taken from short pulse experiments on similar devices [71]. The 1 ps trapping times of carriers into the wells, τ_n and τ_p , are typical values obtained from quantum-well trapping experiments and are often used in other transport models [59, 57]. The trap density in the interior was taken from the fabrication specification for this device [29], and the trap density in the surface-charge regions was taken from typical results for low temperature grown

AlGaAs [75]. The acceptor compensation ratio was set to 0.5 since trap saturation was not a concern in the operating regime being considered.

Simulations using constant mobilities and simulations using velocity-saturated mobilities were both performed. The values of the low field mobilities and the saturated drift velocities are typical for AlGaAs [70]. The field dependence of the mobilities was the same as that used in section 4.6. The effective low field mobility-lifetime products for electrons and holes were $1.5 \times 10^{-7} \text{ cm}^2/\text{V}$ and $6.0 \times 10^{-8} \text{ cm}^2/\text{V}$, respectively. The absorption coefficient and incident intensity were measured experimentally. The intensity in the interior, however, is reduced by the reflectivity of the front gold/PSG layers. The reflectivity was estimated using a stacked-slab dielectric model to be approximately 80%.

The simulations were started from dark, neutral space-charge initial conditions and run using the following sequence of applied voltages: $+V_0$, $-V_0$, $+V_0$. This models the bipolar square wave applied voltage used in the experiments. The time for each voltage segment was long enough to allow the simulation to reach steady-state before the polarity was switched. The displacement photocurrent through the insulating barriers was calculated for comparison to the photocurrent measurements.

5.2.2 Field Screening Results

The screening of the internal field was simulated using constant mobilities and the same applied voltages used in the measurements summarized in Fig. 5-3. The results are shown in Fig. 5-6. As with the experimental results, the initial screening behavior is linear with all voltage cases decaying at the same rate. The time scales for complete screening also agree well with the experimental results. The approach to full screening is more gradual than in the experimental results, but the transmission measurement is not very sensitive at such low fields. The approach to full screening will be examined more carefully using the photocurrent measurements.

The screening behavior seen in the experimental and simulation results is indicative of the large drift length regime described in Chapter 4. In this regime, a saturated internal photocurrent produces a constant screening rate. For large vertical drift lengths, the

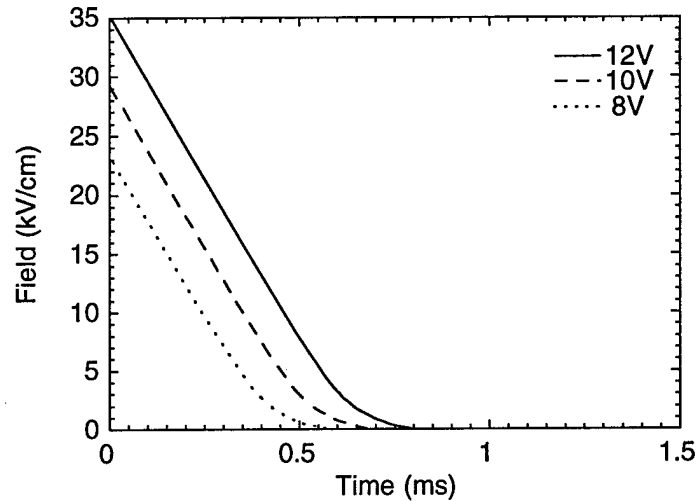


Figure 5-6 Simulated field screening using constant mobilities for the indicated peak-to-peak voltages at positive polarity. The initial linear behavior and screening rate agree well with experimental results.

screening rate can be estimated from the injection model result in Eq. (4-25) with the parameters in Table 5-1. The calculated rate of 50 kV/cm-ms agrees well with the experimental results.

5.2.3 Photocurrent Results

As discussed in Chapter 4, the initial screening behavior in the large vertical drift length regime is not very sensitive to the mobility. The simulated approach to full screening, however, does depend on the mobility model through the dielectric relaxation time. We therefore consider two different models, one with constant mobilities and one with velocity-saturated mobilities.

The simulated photocurrent response using the constant mobilities listed in Table 5-1 is shown in Fig. 5-7. The photocurrent was simulated for positive polarity using the same applied voltages used in the experiments. The behavior agrees qualitatively with the experimental results. The initial photocurrent saturates when the applied voltage reaches approximately 8 V. The initial photocurrent values, however, are slightly different than the experimental values in Fig. 5-4. This discrepancy may be due to small leakage currents

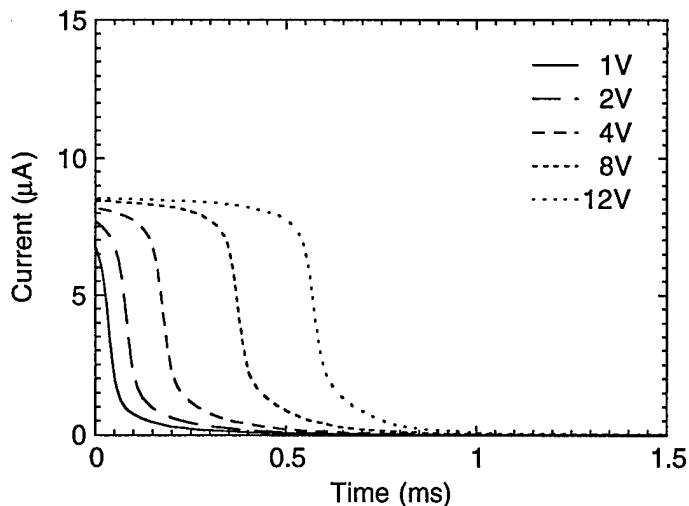


Figure 5-7 Simulated photocurrent response using constant mobilities for the indicated peak-to-peak voltages at positive polarity. The decay of the current signal is due to the transition from the long drift length regime to the dielectric relaxation regime.

and/or slight errors in some device parameters, such as the dielectric permittivity of PSG which depends upon the details of the fabrication process.

From the results of the injection model described in Chapter 4, the decay of the photocurrent for large applied voltages at positive polarity occurs when the electron drift length approaches the device length, or, equivalently, when the mean transit time of electrons across the interior, as given by $L/\tilde{\mu}_{nz}E$, becomes longer than the effective electron lifetime. As the transit time becomes longer than the effective lifetime, the photocurrent transitions from the saturated regime into the dielectric relaxation regime. When the transit time is much shorter than the lifetime, electrons quickly drift to the back interface without being trapped in the interior and contribute efficiently to the screening process. For long transit times, electrons are trapped many times in midgap traps before reaching the back. In fact, for high absorption, the electron current in the back of the device is greatly reduced since electrons trap in regions of reduce optical intensity. A similar effect has been seen in the photocurrent of MQW p-i-n photodiodes when the carrier transit times across the intrinsic region become greater than the carrier lifetimes [72].

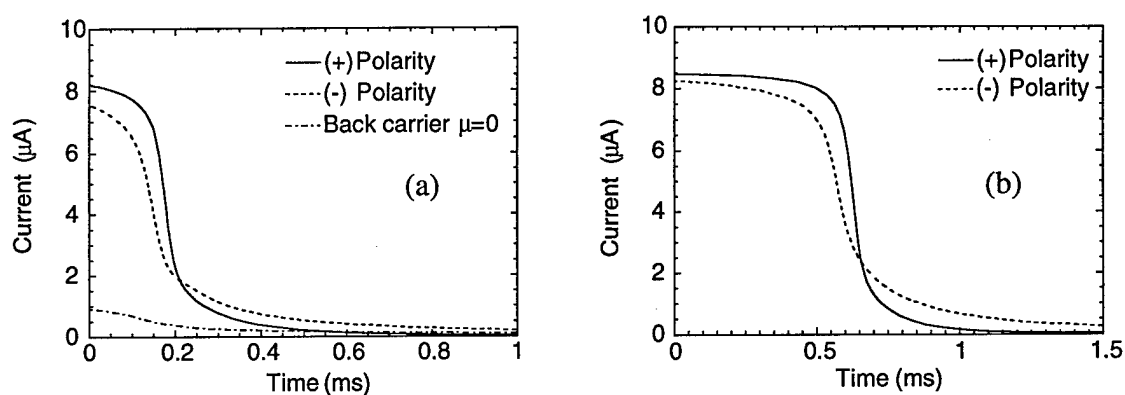


Figure 5-8 Simulated photocurrent response for both polarities using constant mobilities at peak-to-peak voltages of (a) 4 V and (b) 12 V. In (a) the dotted-dashed curve shows the effect of suppressing the mobility (μ) of the back carrier and is the same for both polarities.

The effect of the carrier transit time across the MQW region on the photocurrent response can be seen in Fig. 5-8a which shows the simulated photocurrent for a moderate applied voltage (4 V peak-to-peak) for both polarities. The asymmetry in the response is qualitatively similar to the experimental result in Fig. 5-5 and shows how the photocurrent depends on which carrier is drawn to the back. Drawing the carrier with the largest mobility-lifetime product (electrons) to the back produces a slightly faster response since this pushes the device more into the saturated photocurrent regime. This produces a larger initial current and a slightly faster decay. The sensitivity of the photocurrent to the back-drifting carrier is also seen in Fig. 5-8a. The photocurrent response was simulated with the mobility of the back-drifting carrier set to zero for either polarity. For this case, the photocurrent is drastically reduced. This emphasizes the sensitivity of the response to the back-drifting carrier and provides convincing evidence for bipolar transport.

The simulated photocurrent response using constant mobilities and a large peak-to-peak voltage (12 V) is shown in Fig. 5-8b for both polarities. As in the simulated 4 V case, the photocurrent for positive polarity displays a slightly faster response. However, this does not agree with the experimental results in Fig. 5-5b. Also, the decay of the simulated responses is somewhat sharper than the experimental results. One possible explanation for these two discrepancies is velocity saturation. As discussed in Chapter 4, velocity

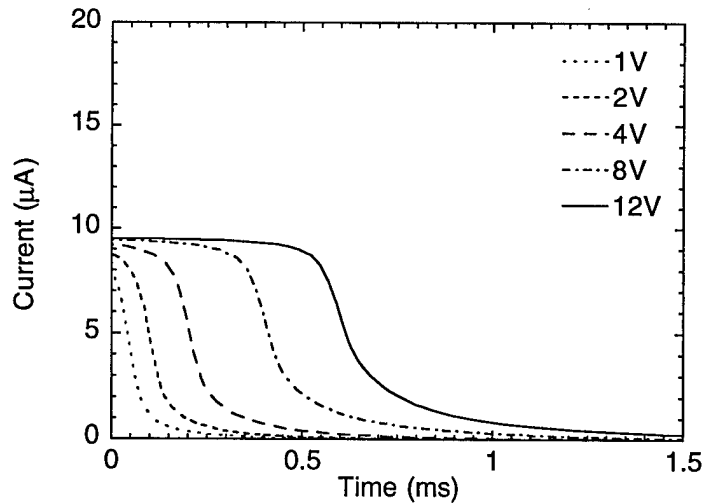


Figure 5-9 Simulated photocurrent response using velocity-saturated mobilities for the indicated peak-to-peak voltages at positive polarity. The decay of the current signal is more gradual than in the constant mobility case.

saturation is a prominent transport effect in bulk GaAs at high fields and is expected to also be so for MQW devices [52].

The velocity saturation of electrons and holes occurs at widely different fields (~ 4 kV/cm for electrons and ~ 30 kV/cm for holes), and this can lead to an unusual photocurrent response depending on the applied voltage and polarity. Here we investigate the effect of a simple velocity saturation model in order to qualitatively show how velocity saturation might affect the photocurrent response. Figure 5-9 shows the simulated photocurrent series for positive polarity using the velocity saturation model summarized in Table 5-1. The decay of the velocity-saturated photocurrent occurs at times similar to those found for the constant mobility case, but the decay is more gradual and more like that seen in the experiments.

As shown in Fig. 5-10, the polarity dependence of the photocurrent simulated using velocity-saturated mobilities also agrees better with the experiments. At low voltages, the ordering of the faster polarity is the same as for the constant mobility case: positive polarity produces a slightly faster response. At such low voltages, velocity saturation has not significantly reduced the electron mobility, leaving the electron mobility-lifetime product

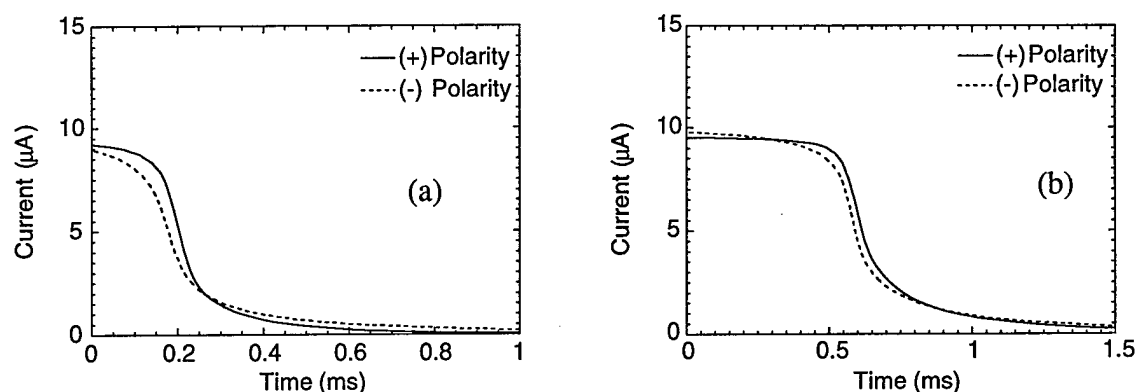


Figure 5-10 Simulated photocurrent response for both polarities using velocity-saturated mobilities at peak-to-peak voltages of (a) 4 V and (b) 12 V. Note that initially, the faster response in (a) occurs at positive polarity while the faster response in (b) occurs at negative polarity.

larger than the hole mobility-lifetime product. However, at larger voltages, as shown Fig. 5-10b, the faster polarity (i.e. carrier) changes as the reduction of the electron mobility by velocity saturation pushes the electron mobility-lifetime product below that of the holes.

The velocity-saturation model which produced Figs. 5-9 and 5-10 was chosen for simplicity. While the field dependence of the hole-mobility in Table 5-1 is actually similar to the field dependence of the hole mobility in bulk GaAs [76], the exact mobility models for vertical transport in GaAs/AlGaAs quantum wells are not known. The general trends of the experimental data, however, are explained by this simple velocity saturation model. In principle, other field dependent effects, most notably carrier escape from wells, could also produce an unusual photocurrent response as a function of field. In the case of carrier escape, however, the field dependence over the voltage range under consideration is too weak to explain the observed effects. As will be discussed in Chapter 7, the field dependence of the carrier escape rates will play an important role in determining device resolution.

5.3 Summary

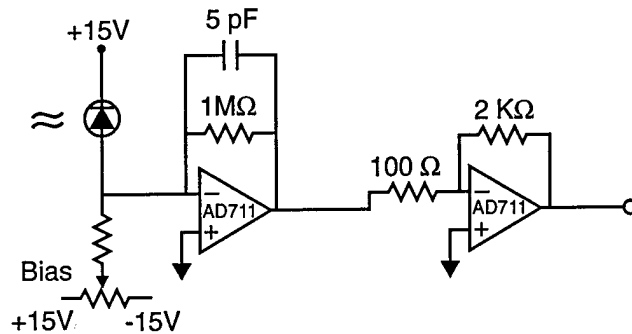
The frame rate of the MQW-OASLM is essentially determined by the screening response under uniform illumination. Accurate estimates of the screening rate are required to optimize trade-offs in device design. In this chapter, optical transmission and photocurrent measurements were used to verify the screening rate calculations in Chapter 4. In addition, the photocurrent measurement described in this chapter was shown to be a particularly sensitive probe of some of the more interesting transport dynamics, including the transition between photogeneration-limited and transport-limited regimes. Evidence for bipolar transport was found using the photocurrent measurement, and an asymmetric response to polarity under high absorption was attributed to the different mobility-lifetime products of the electrons and holes. Finally, a simple velocity-saturation model was used to explain an unusual photocurrent response at high voltages.

5.4 Appendix

In this appendix, the various homemade amplifiers used in the transmission and photocurrent experiments are described. These amplifiers were designed to meet the specific gain and bandwidth requirements for the particular time scales and intensity levels in the experiments. In the case of the current amplifiers, output clamping was an important feature to prevent overloading of the downstream A/D system.

The photodiode amplifier shown in Fig. 5-11a uses a Hamamatsu model S1223-01 silicon photodiode which has an area of 13 mm^2 and a responsivity of 0.6 A/W at 850 nm . It is reverse biased to maintain a small capacitance. The current from the photodiode is amplified by a two stage amplifier. The first stage consists of a transimpedance amplifier with a gain of 10^6 V/A . A 5 pF parallel capacitor is used to prevent ringing, and a DC current bias is provided at the input. This stage is followed by a simple inverting voltage amplifier with a gain of 20. The overall gain of the system is $1.2 \times 10^7 \text{ V/W}$ at 850 nm with a 3 dB bandwidth of 35 kHz.

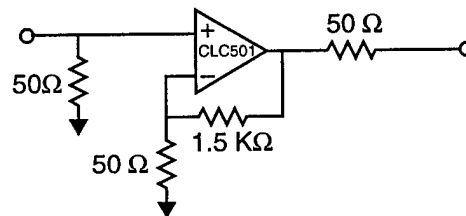
a) Photodiode amplifier



$$G = 2 \times 10^7 \text{ V/A}$$

$$f_{3\text{dB}} = 35 \text{ KHz}$$

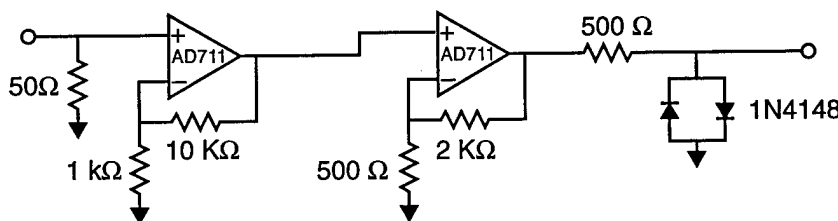
b) Low gain amplifier for current measurements



$$G = 757 \text{ V/A}$$

$$f_{3\text{dB}} > 20 \text{ MHz}$$

c) High gain amplifier for current measurements



$$G = 2.7 \times 10^3 \text{ V/A}$$

$$f_{3\text{dB}} = 340 \text{ KHz}$$

Figure 5-11 Schematic diagrams of the homemade amplifiers used in the transmission and photocurrent experiments. The photodiode amplifier in (a) was used in the calibration of the QCSE and in screening measurements. The low gain, large bandwidth amplifier in (b) was used to investigate large initial transients in the photocurrent response. The higher gain, smaller bandwidth amplifier in (c) was used for the majority of the photocurrent measurements presented in this chapter.

Two different amplifiers were constructed to amplify the current signal passing through the $50\ \Omega$ resistor in series with the sample. The circuit shown in Fig. 5-11b consists of a fast, output clamping Comlinear 501 amplifier in a simple non-inverting configuration. A $50\ \Omega$ output impedance was used, and during measurement the input to the A/D was $50\ \Omega$ terminated to prevent ringing from the cable capacitance. The circuit was laid out on a PC board provided by Comlinear which included a large ground plane to minimize stray capacitance. The gain of this amplifier is $757\ \text{V/A}$ into $50\ \Omega$ with a 3 dB bandwidth greater than 20 MHz. This amplifier was used to investigate the fast transients in the current signal.

The second amplifier, shown in Fig. 5-11c, was used for amplify the current signal in most of the current measurements. It consists of two non-inverting amplifier stages using AD711's with gains of 11 and 5, respectively. The output is clamped using a symmetric diode clamp. The overall gain is $2.7 \times 10^3\ \text{V/A}$ with a bandwidth of 340 kHz. All circuits were enclosed in metal boxes to minimize noise.

Chapter 6

Grating Formation

The simplest example of image formation in optically addressed spatial light modulators is elementary grating formation due to the interference between two plane waves. The resulting sinusoidal intensity distribution can be straightforwardly handled in device models, and it provides a convenient means of characterizing the resolution response through the modulation transfer function discussed in Chapter 2. Assuming a linear response, the performance of an OASLM in an optical system can then be analyzed using a Fourier optics approach [30].

In this chapter, we extend the 1D, uniform-illumination model developed in Chapter 4 to two dimensions. Carrier transport along the applied field direction (vertical) and along the grating (transverse) direction, shown schematically in Fig. 6-1, are both considered. From the results in Chapter 4, it is clear that there are four main elements that must be considered in constructing a 2D MQW-OASLM device model: 1) the electrostatics are determined primarily by the surface charge at the semiconductor-insulator interfaces, 2) dynamic screening requires that vertical transport and the field decay be handled self-consistently, 3) transport along the transverse dimension occurs in the device interior and near the semiconductor-insulator interfaces, and 4) well-carriers, while confined vertically, are free to transport along the transverse direction.

A number of device models have been developed to handle various combinations of these elements, but not all the elements have been considered together. For example, early

PROM models considered the role of field fringing due to the space-charge distribution in determining device resolution [7, 8], and some PROM models considered the effects of 1D and 2D carrier transport [9, 10]. However, the characteristic transport lengths of early PROM's made with oxide materials placed them in a bulk charge regime. In contrast, the MQW-OASLM relies on the screening produced by surface, not bulk, charges. More recent device models have considered ad-hoc surface-charge models along with carrier transport along the grating direction. Nolte has presented a steady-state model for leaky insulators which considered interior drift [14]. Wang *et al.* have presented a transient model that included transverse transport in both the interior and surface-charge regions, but vertical transport was not handled in a self-consistent manner [16]. None of these models has explicitly considered the role of quantum wells.

In this chapter, we present a 2D device model incorporating all the elements mentioned above. Sinusoidal grating formation is simulated using direct numerical solutions to the transport equations. Simplified numerical and analytical solutions are found when possible. In particular, a small signal approximation for small intensity modulations is used to calculate the free-carrier distributions under transverse drift and diffusion. The injection of free-carriers into the surface-charge regions is then used to determine the transient buildup and decay of the electric field grating. A brief review of field-fringing effects due to the surface-charge distribution is also presented. The main results of the small signal model are verified using full numerical solutions to the transport equations. Finally, the dependence of the grating formation process on the intensity modulation is analyzed.

6.1 Device Model

The device model we use for modeling grating formation is similar to the 1D model developed in Chapter 4, except that here we must consider transport along the applied field direction and along the transverse direction as shown in Fig. 6-1. As described in Chapter 4, we consider both free electron and hole transport, as well as the transport of carriers in the quantum wells. The primary modifications to the 1D transport equations

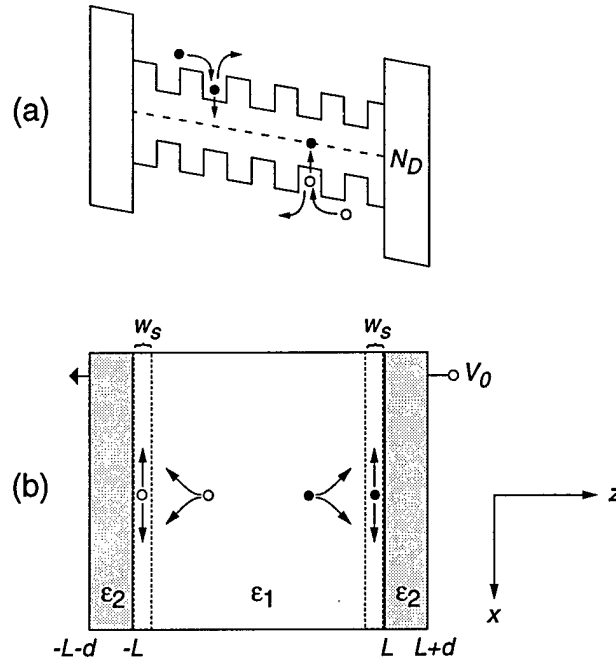


Figure 6-1 2D device geometry. (a) Band diagram showing quantum wells and emission/capture processes. (b) 2D device structure showing transport of carriers in the interior and in the surface-charge regions near the semiconductor-insulator interfaces. Both vertical transport (z) and transverse transport (x) are considered.

involve adding transverse current terms to the continuity equations for free carriers and for well carriers. A 2D Poisson equation is also used. The 2D transport equations are summarized below:

$$\frac{\partial N}{\partial t} = \frac{1}{e} \frac{\partial j_N}{\partial x} + \frac{n}{\tau_n} - (\beta_N + \gamma_N N_D^+) N \quad (6-1)$$

$$\frac{\partial P}{\partial t} = -\frac{1}{e} \frac{\partial j_P}{\partial x} + \frac{p}{\tau_p} - (\beta_P + \gamma_P (N_D - N_D^+)) P \quad (6-2)$$

$$\frac{\partial N_D^+}{\partial t} = \gamma_P (N_D - N_D^+) P - \gamma_N N_D^+ N \quad (6-3)$$

$$\frac{\partial n}{\partial t} = \frac{1}{e} \nabla \cdot \mathbf{j}_n + g(x, z) - \frac{n}{\tau_n} \quad (6-4)$$

$$\frac{\partial p}{\partial t} = -\frac{1}{e} \nabla \cdot \mathbf{j}_p + g(x, z) - \frac{p}{\tau_p} \quad (6-5)$$

$$\nabla \cdot (\epsilon \nabla V) = -e(N_D^+ - N_A + p - n + P - N) \quad (6-6)$$

The continuity equations for free carriers now contain 2D current densities given by

$$\mathbf{j}_n = e\mu_n(n\mathbf{E} + V_T\nabla n) \quad (6-7)$$

$$\mathbf{j}_p = e\mu_p(p\mathbf{E} - V_T\nabla p) \quad (6-8)$$

where \mathbf{E} is the field. The electron and hole mobilities are taken to be anisotropic to account for transverse transport parallel to the quantum wells, μ_{nx} and μ_{px} , and for vertical transport along the applied field, μ_{nz} and μ_{pz} . Anisotropic mobilities are used for two reasons. First, it is expected that the mobilities along the growth direction will be smaller than the transverse mobilities due to alloy scattering and scattering from the well-barrier interfaces [77]. Second, in determining the relative contributions of various transport mechanisms on the screening process, it is convenient to selectively suppress some mechanisms by setting the appropriate transverse mobility to zero in the simulation.

The transverse current terms in the well-carrier continuity equations are given in Chapter 3 as

$$j_N = e\mu_N \left(NE_x + V_T \frac{\partial N}{\partial x} \right) \quad (6-9)$$

$$j_P = e\mu_P \left(PE_x - V_T \frac{\partial P}{\partial x} \right) \quad (6-10)$$

The boundary conditions for the free-carrier current densities and the applied voltage are the same as those used for the 1D model in Chapter 4. The generation term is given for an elementary grating formed by beams incident from the left in Fig. 6-1 as

$$g(x, z) = \frac{\alpha I_0}{h\nu} (1 + m \cos Kx) e^{-\alpha(z+L)} \quad (6-11)$$

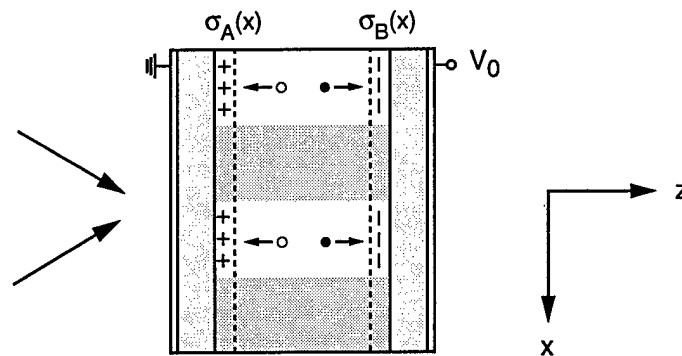


Figure 6-2 Illustration of surface-charge grating formation under sinusoidal illumination conditions indicated by the light and dark fringes. This intensity pattern could be produced, for example, by the interference between two plane waves. Electrons and holes are injected into the surface-charge regions and accumulate. The net surface charge at the interfaces is given by σ_A and σ_B .

where m is the intensity modulation, and $K=2\pi/\Lambda$ is the spatial frequency with Λ the grating spacing. Periodic boundary conditions are used along the grating direction. When full numerical solutions to the above system are required, they are computed using the techniques described in Appendix A.

6.2 Small Signal Injection Model

In Chapter 4 a picture of 1D device operation was presented that described the screening of the applied voltage as occurring through the accumulation of carriers in traps near the semiconductor-insulator interfaces. As illustrated in Fig. 6-2, interior carriers inject and accumulate in a thin surface-charge region near the interfaces. Since the screening rate due to this buildup is proportional to the intensity, a sinusoidal illumination pattern produces a variation in the screening rate across the device. During the initial stages of grating formation, this creates a spatially modulated surface charge that mimics the intensity pattern. The grating formation is transient, however, since the applied voltage eventually becomes fully screened across the entire device.

In this section, a number of issues related to the transient buildup and decay of the screening charge are examined. First, various aspects of the electrostatic solutions for sinusoidal surface-charge patterns are examined, including the resolution limitation

imposed by field fringing. The free-carrier distributions are then calculated in a small signal model developed for intensity modulations much less than unity. In this approximation, the carrier continuity equations are linearized in the intensity modulation for easier analysis. This model is used to determine the effects of transverse transport on the carrier modulations. Finally, the transient buildup and decay of the electric field grating produced by the modulated surface charge is calculated in both the short and long vertical drift length regimes.

6.2.1 Electrostatics

Assuming the grating response is linear in the intensity modulation, the surface charge at each interface can be expanded as

$$\begin{aligned}\sigma_A &= \sigma^{(0)} + m \hat{\sigma}_A^{(1)} \cos Kx \\ \sigma_B &= -\sigma^{(0)} + m \hat{\sigma}_B^{(1)} \cos Kx\end{aligned}\tag{6-12}$$

where σ_A and σ_B refer to the left and right interfaces in Fig. 6-2, respectively, and all the components are real. Charge neutrality has been used to write the zeroth-order components. The corresponding expansions for the field components are

$$E_z(x, z) = E_z^{(0)} + m \hat{E}_z^{(1)}(z) \cos Kx\tag{6-13}$$

$$E_x(x, z) = -m \hat{E}_x^{(1)}(z) \sin Kx\tag{6-14}$$

where $E_z^{(0)}$, $\hat{E}_z^{(1)}$, $\hat{E}_x^{(1)}$ are all real. The “^” on top of the first-order components indicates that the linear-in- m dependence has already been taken into account. The field components can be calculated in terms of the surface charge components by direct solution of the Poisson equation. The resulting field distributions display fringing effects at small grating spacings. These effects have been considered in detail before and produce a lower limit on the device resolution of approximately twice the device length [7, 8]. There are two limiting cases of interest: $\sigma_B = -\sigma_A$ and $\sigma_B = 0$.

The optimum field pattern for efficient electro-optic modulation is produced when $\sigma_B = -\sigma_A$. The field components in the interior are then

$$\begin{aligned}\hat{E}_z^{(1)} &= \frac{\hat{\sigma}_A^{(1)}}{\epsilon_1} \left[1 + \left(\frac{\epsilon_2}{\epsilon_1} \right) \frac{\tanh(KL)}{\tanh(Kd)} \right]^{-1} \frac{\cosh(Kz)}{\cosh(KL)} \\ \hat{E}_x^{(1)} &= \frac{\hat{\sigma}_A^{(1)}}{\epsilon_1} \left[1 + \left(\frac{\epsilon_2}{\epsilon_1} \right) \frac{\tanh(KL)}{\tanh(Kd)} \right]^{-1} \frac{\sinh(Kz)}{\cosh(KL)}\end{aligned}\quad (6-15)$$

For long grating spacings such that $K \sim 0$, $\hat{E}_z^{(1)}$ is constant throughout the interior while $\hat{E}_x^{(1)} \sim 0$. This optimizes the electro-optic response and suppresses transverse drift. At smaller grating spacings, field fringing becomes significant, causing $\hat{E}_z^{(1)}$ to decay into the device center and $\hat{E}_x^{(1)}$ to increase near the interfaces. This reduces the electro-optic effect and increases transverse drift near the interfaces. As can be determined from Eq. (6-15), the resolution limit imposed by field fringing is approximately twice the device length for typical dielectric permittivities.

In some devices, one of the interfaces may have a particularly weak trap density that allows the carrier modulation and the surface charge to become completely washed out. This could happen, for example, if the carrier lifetime in one of the interface regions is not reduced through low-temperature growth or other techniques. In this situation, the grating component of one of the surface-charge patterns, say σ_B , vanishes. In this situation, the field components are given by

$$\begin{aligned}\hat{E}_z^{(1)} &= \frac{\hat{\sigma}_A^{(1)}}{2\epsilon_1} \left\{ \left[1 + \left(\frac{\epsilon_2}{\epsilon_1} \right) \frac{\tanh(KL)}{\tanh(Kd)} \right]^{-1} \frac{\cosh(Kz)}{\cosh(KL)} - \left[1 + \left(\frac{\epsilon_2}{\epsilon_1} \right) \frac{\coth(KL)}{\tanh(Kd)} \right]^{-1} \frac{\sinh(Kz)}{\sinh(KL)} \right\} \\ \hat{E}_x^{(1)} &= \frac{\hat{\sigma}_A^{(1)}}{2\epsilon_1} \left\{ \left[1 + \left(\frac{\epsilon_2}{\epsilon_1} \right) \frac{\tanh(KL)}{\tanh(Kd)} \right]^{-1} \frac{\sinh(Kz)}{\cosh(KL)} - \left[1 + \left(\frac{\epsilon_2}{\epsilon_1} \right) \frac{\coth(KL)}{\tanh(Kd)} \right]^{-1} \frac{\cosh(Kz)}{\sinh(KL)} \right\}\end{aligned}\quad (6-16)$$

For this case, both the x and z components contain terms that are symmetric and anti-symmetric in z . For $\hat{E}_z^{(1)}$, the $\sinh(Kz)$ term effectively plays no role in the electro-optic phase modulation since the net phase change, after integrating over the device length,

vanishes. The $\cosh(Kz)$ term, however will contribute, producing a net phase change that is one-half that of the $\sigma_B = -\sigma_A$ case. Thus, losing the surface-charge modulation at one interface cuts the phase modulation in half for the same amount of surface charge.

6.2.2 Carrier Distributions

To determine the free-carrier distributions, all variables are expanded in the following form, using the free-electron concentration as an example: $n = n_0(z) + m\hat{n}_1(z)\cos Kx$. Using the quasi-steady state approximation and plugging these Fourier expansions into the free- and well-carrier continuity equations, effective continuity equations for the first Fourier components of the free-carrier densities can be found. The zeroth-order components of the free-carrier densities are given in Chapter 4. The free-carrier distributions are best characterized in terms of the various transport lengths, i.e. the vertical and transverse drift and diffusion lengths. For computing the first-order components, we consider here two different cases: transport lengths much shorter than the device length, and transport lengths much longer than the device length.

Short Transport Lengths

For transport lengths much shorter than the device length, transverse drift and diffusion can be neglected since field fringing dominates the device performance at small grating spacings before transverse transport becomes significant. In this regime, the first-order components of the free-carrier densities are the same as the zeroth-order densities, Eq. (4-14). For small absorption, the interior densities are uniform and given by $\hat{n}_1 = g_0\tilde{\tau}_{Rn}$ and $\hat{p}_1 = g_0\tilde{\tau}_{Rp}$ where $\tilde{\tau}_{Rn}$ and $\tilde{\tau}_{Rp}$ are the effective recombination times for electrons and holes, respectively.

Since transverse transport is negligible, the surface-charge rate equations for the first-order components are also similar to the rate equations for the zeroth-order components. For the electron surface-charge region, for example, the rate equation is given by

$$\frac{\partial \sigma_B^{(1)}}{\partial t} = j_{pz}^{(1)} \Big|_{z_0} + j_{nz}^{(1)} \Big|_{z_0} \quad (6-17)$$

Long Transport Lengths

For transport lengths much longer than the device length, it is necessary to consider transverse drift and diffusion when calculating the free-carrier densities. Transverse diffusion drives carriers from regions of high concentration to regions of low concentration, thereby reducing the modulation of the carrier densities. Due to the phase of $\hat{E}_x^{(1)}$ from Eq. (6-15), transverse drift also drives carriers from regions of high to regions of low concentration.

Including transverse transport in the continuity equations complicates the quasi-steady state equations for the first-order free-carrier densities. For example, the first-order component of the free-electron density is given by the solution to

$$\begin{aligned} -L_D^2 \frac{\partial^2 \hat{n}_1}{\partial z^2} + L_E \frac{\partial \hat{n}_1}{\partial z} + (1 + \tilde{\mu}_{nx} \tilde{\tau}_n V_T K^2) \hat{n}_1 \\ = g_0 \tilde{\tau}_{Rn} - \tilde{\mu}_{nx} \tilde{\tau}_n \hat{E}_x^{(1)} K n_0 + \tilde{\mu}_{nz} \tilde{\tau}_n \frac{\partial (n_0 \hat{E}_z^{(1)})}{\partial z} \end{aligned} \quad (6-18)$$

where $\tilde{\mu}_{nx}$ is the effective transverse mobility due to transport above the barriers and in the wells. The vertical diffusion length, L_D , the vertical drift length L_E , and the effective carrier lifetime, $\tilde{\tau}_n$, are the same as those used in Chapter 4. The solution of this equation requires the zeroth-order component of the free-electron density as well as the first-order field components.

The effective transverse mobility is given in terms of the well-electron and free-electron mobilities. Since Eq. (6-18) is derived for the long vertical drift length regime, in this section we therefore only consider devices with good carrier escape rates and long carrier lifetimes. Under these conditions $\beta_N \tau_N \gg 1$, and $\tilde{\mu}_{nx}$ is given by

$$\tilde{\mu}_{nx} = \left(\frac{\beta_N \tau_n}{1 + \beta_N \tau_n} \right) \mu_{nx} + \left(\frac{1}{1 + \beta_N \tau_n} \right) \mu_N \quad (6-19)$$

This is the weighted sum of the free-carrier transverse mobility and the well-confined mobility in which the weighting factors are given by the relative time spent in the conduction band above the barriers and in the well, respectively. Transport in the wells thus increases the anisotropic nature of carrier transport, and for moderate escape rates and fast carrier capture times, the effective transverse mobility is determined by the well mobility.

The buildup of the surface charge is calculated from the trapping of free carriers by traps in the surface-charge regions. As discussed in Chapter 4, the buildup of the surface charge in the electron surface-charge region is given by

$$\frac{\partial \sigma_B}{\partial t} \equiv e \int_{z_0}^L \frac{\partial N_D^+}{\partial t} dz \approx -e \int_{z_0}^L \frac{n}{\tilde{\tau}_n^s} dz \quad (6-20)$$

for long vertical drift lengths.

Using the electron continuity equation and the current boundary conditions, Eq. (6-20) can be rewritten as

$$-e \frac{n_s}{\tilde{\tau}_n^s} = j_{nz} \Big|_{z_0} - \frac{\partial}{\partial x} \int_{z_0}^L j_{nx} dz \quad (6-21)$$

where $n_s = \int_{z_0}^L n(z) dz$ is the net surface density of electrons, and $j_{nz} = e\mu_{nz}nE_z$ is the injecting current from the interior, neglecting diffusion. This current is evaluated at the interior edge of the surface-charge region, z_0 in Fig. 4-1, and only uses the relaxation term of the electron density. The transverse current in the surface-charge region is given by j_{nx} .

To proceed, $E_x^{(1)}$ is assumed to be independent of z in the surface-charge region. This can be verified by considering that $\nabla \times \mathbf{E} = 0$, and has also been verified in direct numerical calculations. The resulting free-electron surface densities in the surface-charge region are given in terms of the Fourier cosine components of n_s and j_{nz} as

$$n_s^{(0)} = j_{nz}^{(0)} \Big|_{z_0} \tilde{\tau}_{Rn}^s \quad (6-22)$$

$$\hat{n}_s^{(1)} = \left. \frac{\hat{j}_{nz}^{(1)} \tilde{\tau}_{Rn}^s - \tilde{\mu}_{nx}^s \tilde{\tau}_n^s K n_s^{(0)} \hat{E}_x^{(1)}}{1 + \tilde{\mu}_{nx}^s \tilde{\tau}_n^s V_T K^2} \right|_{z_0} \quad (6-23)$$

where $\tilde{\mu}_{nx}^s$ is the effective transverse mobility in the surface-charge region.

Equations (6-22) and (6-23) describe the development of the electron distribution in the surface-charge region as arising from two sources. The first source is the injection of electrons from the interior into the surface-charge region. The second source is the transverse drift and diffusion of electrons within the surface-charge region. A similar analysis for hole transport at the opposite interface produces analogous results. Equations (6-22) and (6-23) can be used in Eq. (6-20) to compute the surface charge.

6.2.3 Grating Formation

The time dependence of the first-order vertical field component, $\hat{E}_z^{(1)}$, can now be computed by considering the buildup of the trapped surface charge. The solutions for the zeroth-order component, $\hat{E}_z^{(0)}$, are the same as in Chapter 4. We consider here the long grating spacing limit ($\Lambda \gg L$) in which all transverse transport is negligible and in which all field components are independent of z . The rate equations for the surface charge components then contain only injection from the interior carriers. For the long transport length case, the transverse drift and diffusion terms in the continuity equations for interior carriers, Eq. (6-18), are neglected. This simplifies the analysis and allows the calculation of the basic time dependence of grating formation. The effect of transverse transport at smaller grating spacings will be examined in the following chapter. We assume that the electron and hole response is symmetric so that $\hat{\sigma}_A^{(1)} = -\hat{\sigma}_B^{(1)}$. As discussed in Chapter 4, it can be shown that this approximation is valid for very short vertical drift lengths and very long vertical drift lengths. However, this approximation is inaccurate for intermediate cases, but it does simplify the analysis.

Short Vertical Drift Lengths

For short vertical drift lengths, the complete time dependence of the first-order field component can be solved analytically. Expanding the first-order current in the surface-charge rate equation, Eq. (6-17), and using Eq. (6-15) to write the surface charge in terms of the field, the rate equation for the first-order field component is

$$\frac{\partial \hat{E}_z^{(1)}}{\partial t} + \frac{\hat{E}_z^{(1)}}{\tau_0} = \frac{E_z^{(0)}}{\tau_0} \quad (6-24)$$

where τ_0 is the screening time from Eq. (4-22). The buildup of $\hat{E}_z^{(1)}$ is driven by the zeroth-order component on the right-hand-side and damped by itself on the left-hand-side.

Using the zeroth-order result, Eq. (4-23), and the initial conditions $E_z^{(0)} = -E_0$ and $\hat{E}_z^{(1)} = 0$, the solution to Eq. (6-24) is

$$\hat{E}_z^{(1)} = E_0 \left(\frac{t}{\tau_0} \right) e^{-\frac{t}{\tau_0}} \quad (6-25)$$

For times short compared to the screening time, τ_0 , the grating builds up in a linear fashion from the injection of the modulated carriers by the zeroth-order field component. The growth slows, however, as the field becomes screened in the more illuminated regions. At time τ_0 the grating peaks at a value of $e^{-1}E_0$ and then decays slowly as the interior field becomes screened even in the darker regions.

Long Vertical Drift Lengths

For long vertical drift lengths, the complete buildup and decay of the first-order component cannot be solved analytically. After expanding the injection current components, the rate equation for the first-order field component is

$$\frac{\partial \hat{E}_z^{(1)}}{\partial t} = -e\mu_{nz}\chi_0(n_0 \hat{E}_z^{(1)} + \hat{n}_1 E_z^{(0)}) \Big|_{z_0} \quad (6-26)$$

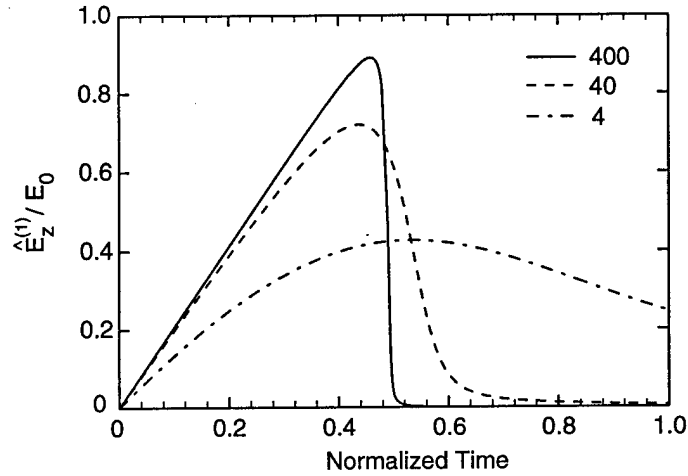


Figure 6-3 Buildup and decay of the first-order field component during grating formation for the indicated values of L_E/L .

where χ_0 is given by Eq. (4-19). From Eqs. (4-14) and (6-18), the electron Fourier components are themselves functions of the field components. The resulting nonlinear system is solved numerically with the following initial conditions: $E_z^{(0)} = -E_0$ and $\hat{E}_z^{(1)} = 0$. The solutions can be characterized in terms of the absorption coefficient, α , and the initial value of the drift length, L_E , at the start of the screening process.

Solutions to Eq. (6-26) are shown in Fig. 6-3 for various values of the initial vertical drift length at $\alpha = 2.0 \times 10^4 \text{ cm}^{-1}$. To compare time scales, E_0 is held constant, and the vertical mobility-lifetime product is varied to obtain different vertical drift lengths. As demonstrated by the $L_E/L = 400$ curve in Fig. 6-3, for long initial vertical drift lengths the first-order component builds up linearly in time in a manner similar to the zeroth-order component, but then decays rapidly as the bias voltage becomes fully screened. For $L_E/L \rightarrow \infty$, the peak value of $\hat{E}_z^{(1)}$ approaches E_0 .

For smaller values of the initial drift length, the initial buildup of $\hat{E}_z^{(1)}$ slows. In addition, the peak value decreases, and for very short drift lengths, it approaches $e^{-1}E_0$ as previously discussed. The fall time also increases dramatically as shown in Fig. 6-3 for the $L_E/L = 4$ curve. In general, longer vertical drift lengths produce a faster rise, a larger peak grating amplitude, and a shorter fall time, all of which are desirable for optimum device performance.

6.3 Numerical Results

In this section, we examine some of the details of the screening process using direct numerical solution of the transport equations and assess the validity of the main approximations used in the development of the small signal injection model described previously. Three main approximations were made in the development of the small signal injection model: 1) the space charge is dominated by surface charge, 2) the response is linearly proportional to m , and 3) the grating spacing was restricted to values much greater than the device length. To investigate the validity of these approximations, grating formation was simulated in a device with the parameters listed in Table 4-1 and the following transport parameters: equal electron and hole parameters with effective vertical mobilities of $180 \text{ cm}^2/\text{V}\cdot\text{s}$, effective transverse mobilities of $2000 \text{ cm}^2/\text{V}\cdot\text{s}$, effective interior free-carrier lifetimes of 1 ns, and effective surface-carrier lifetimes of 10 ps. These effective parameters are appropriate for electron transport in AlGaAs using the shallow trap model. Equal electron and hole parameters were used to simplify the analysis of the results. These parameters place the device in the long transport length regime which is optimal for speed and peak grating amplitude. To compare the results with the small signal model, the first-order Fourier component of the vertical field is computed numerically and then normalized by the intensity modulation to give $\hat{E}_z^{(1)}$.

6.3.1 Field Uniformity

In Fig. 6-4 the vertical profile of $\hat{E}_z^{(1)}$ along the device length for $m = 1.0$ is shown at the peak of the grating amplitude and for long grating spacing ($\Lambda \gg L$). The profile is quite uniform, with most of the variation occurring in the surface-charge regions near the interfaces as was the case for the zeroth-order component in Figure 4-6. This also supports the surface-charge model of field screening.

The field profile in Figure 6-4 was computed for long grating spacings where transverse transport is not significant. The surface-charge components at both interfaces were found to have approximately the same modulation. However, at smaller grating spacings,

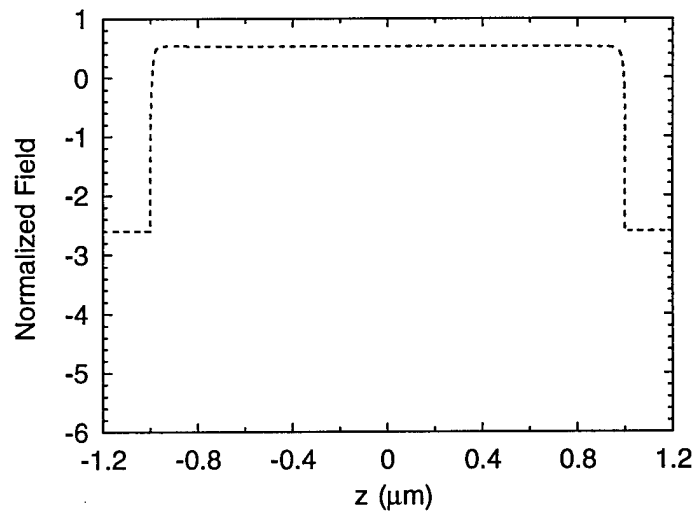


Figure 6-4 Distribution of the first-order field component along the device length. As for the zeroth-order component in Fig. 4-6, good uniformity is maintained in the interior.

when transverse transport is significant, the first-order surface charge components at one or both of the interfaces can be washed out. As indicated by Eq. (6-16), this produces a non-uniform field profile. In addition, bulk charge can become significant compared to the washed out surface-charge component, invalidating the surface-charge picture altogether. These issues will be addressed further in the next chapter when transverse transport is examined in more detail.

6.3.2 Intensity Modulation Dependence

Another basic assumption of the small signal injection model is that the grating response is proportional to the intensity modulation, m . This assumption is examined in Fig. 6-5a in which the buildup and decay of the normalized first-order vertical field component, $\hat{E}_z^{(1)}$, is shown for various values of the intensity modulation. The field component is evaluated at the device center. For small values of the intensity modulation, $\hat{E}_z^{(1)}$ is approximately independent of the intensity modulation, indicating that the overall grating response is, in fact, linear in m . For larger values of m , however, the approximation that the grating response is linear in m breaks down. The peak of $\hat{E}_z^{(1)}$ decreases and moves to shorter

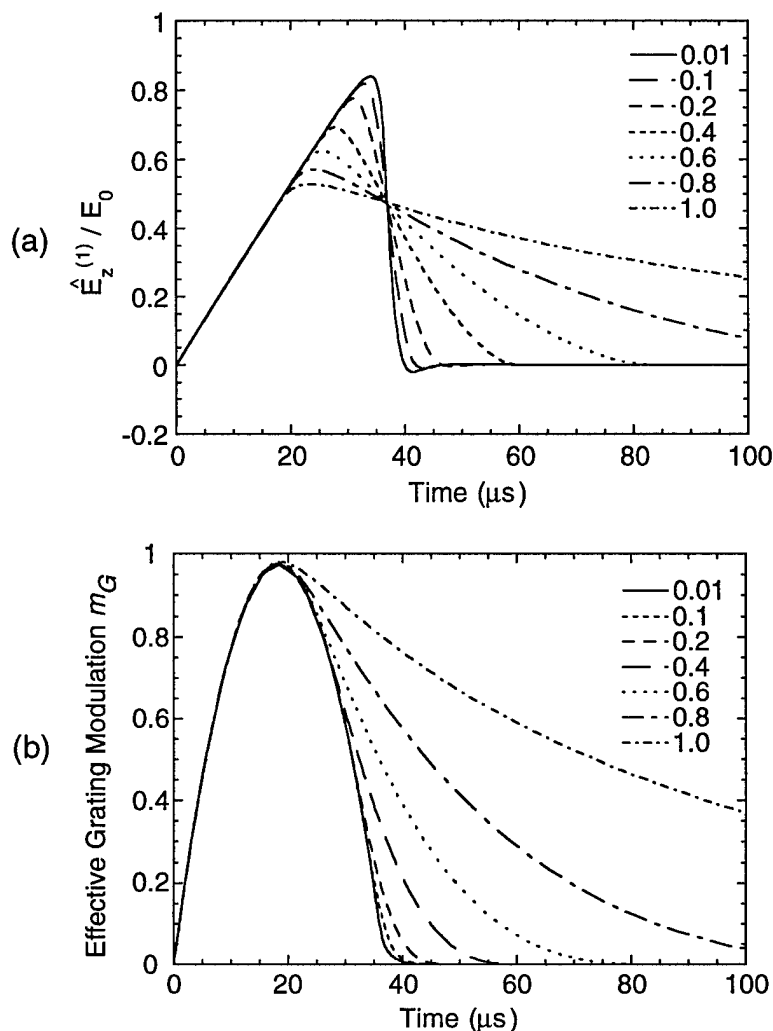


Figure 6-5 Dependence of the grating response on the intensity modulation. (a) Vertical first-order field component for the indicated values of the intensity modulation. (b) Corresponding effective grating modulation, m_G , defined in Eq. 6-30.

times, and the fall-time increases dramatically. The latter effect is due to the large difference in screening times in the light and dark fringes at large m . The small signal injection model, therefore, really is a small signal model, limited to values of m less than about 0.2.

As discussed in Chapter 2, the linearity of the overall diffraction process is characterized by the linearity of the transmission of the first-order diffracted beam. The transmission of the first-order diffracted beam is determined by the dielectric grating produced by

the first-order vertical field component and the electro-optic effect which, in this case, is the QCSE. The QCSE produces changes in both the index of refraction and the absorption coefficient. These changes are, to lowest order, quadratic in the vertical field component and can be written as $\Delta n = -\frac{1}{2}n_0^3 s_1 E_z^2$ and $\Delta\alpha = -\frac{2\pi}{\lambda_0} n_0^3 s_2 E_z^2$, where n_0 is the unmodulated index of refraction, λ_0 is the free-space wavelength, and s_1 and s_2 are the quadratic electro-optic coefficients [46]. The complex index grating with grating vector K produced by the field expansion from Eq. (6-13) will then be $\Delta n' \cos Kx$, where

$$\Delta n' = -\frac{1}{2}n_0^3(s_1 + is_2)G(z) \quad (6-27)$$

and $G(z) = 2m E_z^{(0)} \hat{E}_z^{(1)}$. As discussed in Chapter 2, the readout of such a grating produces Raman-Nath diffraction with the small signal transmission into the first diffracted order given by

$$T_1 \approx -i\frac{\delta}{2} \quad (6-28)$$

where the phase shift, δ , is given by

$$\delta = -\frac{\pi n_0^3}{\lambda_0 \cos \theta'}(s_1 + is_2) \int_{-L}^L G(z) dz \quad (6-29)$$

The dependence of the transmission on the grating formation process is thus contained in $G(z)$.

To characterize the dielectric grating response for various intensity modulations and grating spacings, we normalize the integral of $G(z)$ and define an effective grating modulation function, m_G , as

$$m_G = \frac{\int_{-L}^L G(z) dz}{mLE_0^2} \quad (6-30)$$

The normalization value used here is the maximum value of the integral of $G(z)$ calculated from the small signal injection model for long vertical drift lengths.

The plots of m_G corresponding to the same values of the intensity modulation used in Fig. 6-5a are shown in Fig. 6-5b. The responses for all values of the intensity modulation are nearly identical during the initial formation of the grating up to the peak amplitude. The peak values for all intensity modulations are approximately unity, in good agreement with the results from the small signal injection model. The decay of m_G , however, depends strongly on the intensity modulation, and very asymmetric rise and fall times are produced for large values of m .

These results indicate that the transmission linearity of the first-order diffracted beam should be quite good during the initial stages of grating formation up to the grating peak. Linearity during decay, however, appears very poor. In an application such as an optical correlator where linearity is important, it might therefore be necessary to read out the grating only during the initial stages of grating formation.

6.3.3 Transverse Transport

The last major approximation used in the development of the small signal injection model is the restriction to long grating spacings. As the grating spacing is reduced, transverse transport increases because the transverse diffusion gradient and the transverse field component increase. This is illustrated in Fig. 6-6 in which the peak amplitude of $\hat{E}_z^{(1)}(z=0)$ for $m = 0.1$ is plotted versus grating spacing for two cases: the geometric case in which transverse transport is suppressed, and the nominal case in which transverse transport is included. The artificial suppression of transverse drift and diffusion in the simulation allows for a convenient analysis of the relative contributions of various transport mechanisms to the screening process. Both curves in Fig. 6-6 are normalized by the long grating spacing value. While the resolution in the geometric case falls off at around twice the device length, the resolution in the nominal case falls off at a much longer grating spacing. Using a 50% decrease in the amplitude of $\hat{E}_z^{(1)}$ from the long grating spacing value as a resolution criterion, the geometric resolution limit is $3.7 \mu\text{m}$ while the nominal resolution limit is only $22 \mu\text{m}$. As we will see in the following chapter, this precipitous roll-off is due primarily to transverse drift.

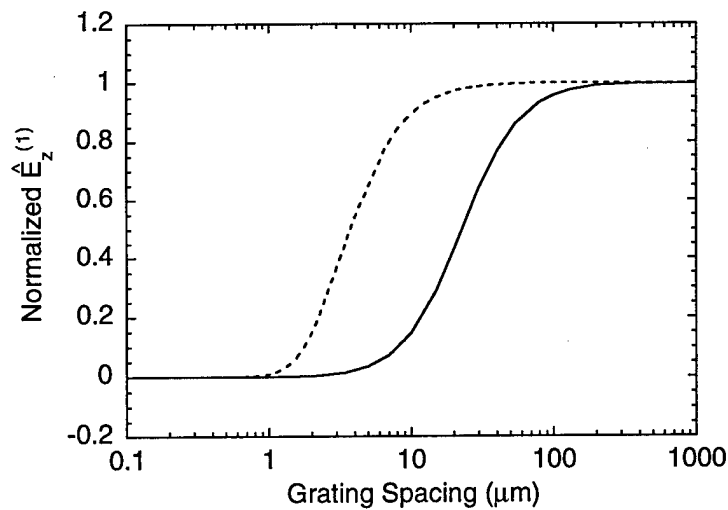


Figure 6-6 Geometric (dotted) and nominal (solid) resolution curves. The nominal resolution curve rolls off at longer grating spacings due to transverse transport. The geometric resolution curve rolls off due to field fringing.

6.4 Summary

In the previous chapter it was found that the screening rate under uniform illumination was optimized for vertical drift lengths much longer than the device length. In this chapter, a small signal analysis of grating formation under sinusoidal illumination showed that long vertical drift lengths optimize not only the initial rise time of the grating, but also the fall time and the peak grating amplitude. These results, however, were limited to long grating spacings in which transverse transport was negligible. A cursory examination of the impact of transverse transport on resolution indicated that, in the long transport length regime, a severe degradation of resolution can occur. It remains to be seen if all three performance criteria- speed, peak grating amplitude, and resolution- can be simultaneously optimized through appropriate device design. A detailed analysis of various techniques to optimize overall device performance will be presented in the next chapter.

In addition to speed, peak grating amplitude, and resolution another important criterion for OASLM performance is linearity, characterized in this chapter by the dependence

of the dielectric grating on the intensity modulation. Full numerical solutions to the transport equations established that the complex phase modulation created by screening and subsequent QCSE modulation is in fact linear in the intensity modulation, at least for short times. This implies that the transmission of the first-order diffracted beam is also linear for small phase modulations. For long times, however, the grating response was found to be very nonlinear, especially at large intensity modulations. In some applications, this may constrain the readout of the grating to the initial stages of grating formation in order to assure a linear response.

Chapter 7

Resolution Performance

As discussed in the previous chapter, for typical MQW-OASLM device designs the resolution performance is limited by the transverse transport of electrons and holes. Transverse transport washes out the modulation in the carrier densities and causes the modulation transfer function to roll off at grating spacings much longer than the geometric, field-fringing limit. Some of the first experimentally demonstrated devices displayed this type of behavior, with resolutions worse than 30 μm . Recently, there have been several experimental efforts to optimize various aspects of device performance including resolution, speed, and diffraction efficiency. Diffraction efficiency is determined primarily by the strength of the quantum confined Stark effect and can be increased through different well-barrier designs [78] and the use of asymmetric Fabry-Perot etalon structures [79]. The optimization of speed and the optimization of resolution are in fact linked and have been pursued along two different approaches. One approach has concentrated on optimizing resolution performance by using semi-insulating, short lifetime quantum-well material in the interior region to suppress interior transport [80]. While this technique appears successful in improving resolution performance, devices fabricated with this design suffer a relatively slow frame rate. Another approach has attempted to optimize speed by using an intrinsic interior region to reduce the carrier transit times [62]. Initial results indicate that this technique can improve the frame rate while still maintaining good resolution as long as the semiconductor-insulator interface region is made strongly semi-insulating. In this

chapter we investigate the trade-offs and limitations involved in simultaneously optimizing both the speed and resolution performance

To calculate the resolution performance, we use the device model described in the previous chapter. The roles of drift and diffusion in both the interior and surface-charge regions in determining the resolution performance are examined. The results of full numerical solutions, as well as analytical estimates of the transport-limited resolution, are presented. A brief discussion of nonlinear transport effects specific to semiconductor and quantum-well materials is also given, focusing on the relevance to resolution performance. An example of device optimization in which experimentally accessible device parameters are modified to optimize both speed and resolution performance is also presented.

7.1 Transverse Transport

Transverse transport along the grating direction washes out the carrier modulation, reduces the grating amplitude, and pushes the resolution limit to longer grating spacings. This is exacerbated by the presence of quantum wells which allow the transport of confined, as well as free, carriers. In the small signal injection model developed in the previous chapter, the device was modeled as consisting of an interior region and two surface-charge regions near the semiconductor-insulator interfaces. As a carrier in the interior drifts towards one of the interfaces, it also drifts and diffuses along the grating vector, washing out the carrier modulation. Once injected into the surface-charge region, the carrier undergoes further drift and diffusion along the interface before being trapped, which also reduces the carrier modulation. The carrier densities in the interior and in the surface-charge regions can be estimated from Eqs. (4-14), (6-18), (6-22), and (6-23). The calculation of the full time dependence of the resulting screening behavior, however, requires direct numerical solution of the original transport equations. To isolate the effects of drift and diffusion in the two device regions, each transport process can be selectively activated in the simulation. Simulations were performed using the device parameters in Table 4-1, using equal electron and hole parameters. The mobilities, well escape rates, and carrier

lifetimes were adjusted to examine transverse transport for various vertical and transverse transport lengths. The grating spacing at which the peak value of $\hat{E}_z^{(1)}(z=0)$ was reduced by 50% from the value at long grating spacings was used as a resolution criterion to compare the various transport effects. As mentioned above, we are primarily interested in the long vertical drift length regime in which the speed response is optimized.

7.1.1 Interior Transport

The initial buildup of screening charge due to the injection of interior electrons into the surface-charge region is given by Eqs. (6-20) and (6-21). In the long vertical drift length regime, the surface-charge rate equation is

$$\frac{\partial \hat{\sigma}_B^{(1)}}{\partial t} = e\mu_{nz}\hat{n}_1 E_z^{(0)} \Big|_{z_0} \quad (7-1)$$

Using the zeroth-order electron component from Eq. (4-14) in the limit of $L_E/L \gg 1$, the surface-charge rate equation can be approximated as

$$\frac{\partial \hat{\sigma}_B^{(1)}}{\partial t} = e g_0 \frac{\hat{n}_1}{n_0} \Big|_{z_0} \times \begin{cases} 1/\alpha & \alpha L \gg 1 \\ 2L & \alpha L \ll 1 \end{cases} \quad (7-2)$$

where the upper factor is for high absorption and the lower factor is for low absorption. The initial buildup of the surface-charge grating component is thus proportional to the effective electron modulation, \hat{n}_1/n_0 , at the interior edge of the surface-charge region.

Transverse diffusion acts to transport carriers from lighter to darker regions. For long vertical drift lengths, the effective electron modulation at low absorption ($\alpha L \ll 1$) is calculated from Eq. (6-18) as

$$\frac{\hat{n}_1}{n_0} = 1 - \left(\frac{L}{L_E}\right) K^2 L_{D_x}^2 \quad (7-3)$$

where the transverse diffusion length in the interior is given in terms of the effective transverse mobility and lifetime as $L_{D_x} = \sqrt{\tilde{\mu}_{nx}^i \tilde{\tau}_n^i V_T}$. For high absorption ($\alpha L \gg 1$), the

effective electron modulation depends on whether the electrons are drawn to the front or the back of the device relative to the incident beam:

$$\frac{\hat{n}_1}{n_0} = \begin{cases} 1 - \left(\frac{2L}{L_E}\right) K^2 L_{D_x}^2 & \text{back} \\ 1 & \text{front} \end{cases} \quad (7-4)$$

where the upper result is for electrons drawn to the back and the lower result is for electrons drawn to the front. For low absorption, the response is the same whether the electrons are drawn to the back or to the front. The L/L_E factor in Eq. (7-3) can be interpreted as the mean transit time, given by $L/\tilde{\mu}_{nz}^i E_0$, divided by the interior electron lifetime, $\tilde{\tau}_n^i$. The high absorption case can be interpreted similarly. For high absorption, back-drifting carriers are generated only at the front of the device and must transport a distance of $2L$ to the back. For carriers drawn to the front, there is essentially no transport in the interior at all.

The results in Eqs. (7-3) and (7-4) indicate that improving vertical transport can suppress transverse diffusion. The subsequent effect on the screening of the electric field is shown in Fig. 7-1 in which the simulated resolution limit imposed by transverse interior diffusion is plotted versus the effective vertical mobility-lifetime of the free carriers. Results for two values of the effective transverse mobility-lifetime product are shown. The best resolution that can be achieved is given by the geometric limit due to field fringing. For both values of the transverse mobility-lifetime product, the resolution performance improves dramatically as the vertical transport behavior improves. For a transverse mobility-lifetime product of $1.0 \times 10^{-6} \text{ cm}^2/\text{V}$, the effects of transverse diffusion are almost fully suppressed below the geometric resolution limit at a vertical mobility-lifetime product of $1.0 \times 10^{-6} \text{ cm}^2/\text{V}$.

Due to the phase of E_x , given by Eqs. (6-14) and (6-15), transverse drift also drives carriers from light to dark regions, washing out the carrier modulation. Although the effect of transverse drift is difficult to consider analytically due the z dependence and the dynamic buildup of $\hat{E}_x^{(1)}$, a simplified model in which $E_z = -E_0$ and $\hat{E}_x^{(1)} = E_0 \sinh KL$

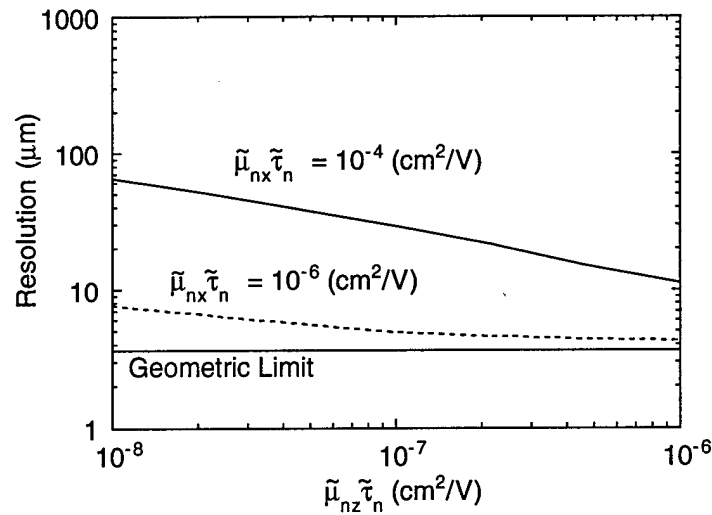


Figure 7-1 Resolution limit imposed by interior diffusion versus the effective vertical mobility-lifetime product of the free carriers. Results for two values of the effective transverse mobility-lifetime products of the free carriers are shown. The geometric limit due to field fringing is also shown.

can be used to indicate the effect of vertical drift. Using these field values in Eq. (6-18), the effective electron modulation for low absorption is found to be

$$\frac{\hat{n}_1}{n_0} = 1 - \left(\frac{L}{L_E}\right)KL_{E_x} \quad (7-5)$$

while the result for high absorption is

$$\frac{\hat{n}_1}{n_0} = \begin{cases} 1 - \left(\frac{2L}{L_E}\right)KL_{E_x} & \text{back} \\ 1 - \left(\frac{1}{\alpha L_E}\right)KL_{E_x} & \text{front} \end{cases} \quad (7-6)$$

where $L_{E_x} = \tilde{\mu}_{nx}^i \tilde{\tau}_n^i \hat{E}_x^{(1)}$ is the transverse drift length in the interior due to $\hat{E}_x^{(1)}$. As was the case for interior diffusion, the effect of transverse drift is suppressed by the ratio of the vertical transit time divided by the effective carrier lifetime. This is demonstrated in Fig. 7-2 where the simulated resolution limit imposed by transverse interior drift is plotted versus the effective vertical mobility-lifetime product for two values of the effective

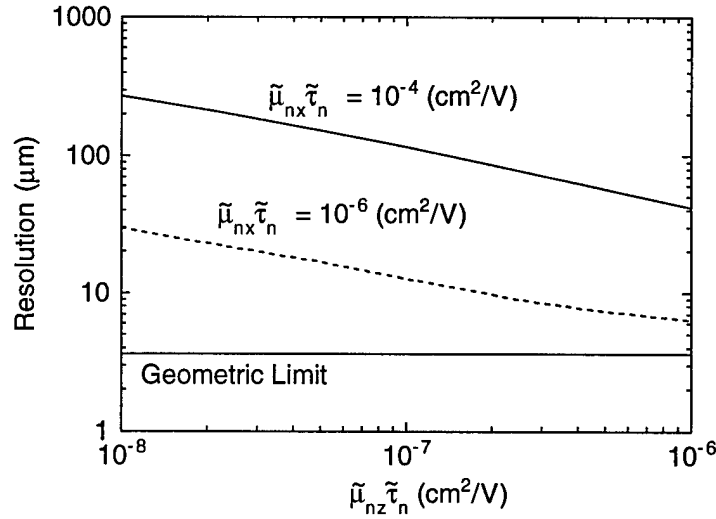


Figure 7-2 Resolution limit imposed by interior drift versus the effective vertical mobility-lifetime product of the free carriers. Results are shown for the indicated effective transverse mobility-lifetime products of the free carriers.

transverse mobility-lifetime product. As in the diffusion case, the resolution performance improves as the effective vertical mobility-lifetime product increases. For the applied voltage used to generate Figs. 7-1 and 7-2, 20 V, transverse drift produces a resolution limit that is a factor of four worse than that produced by transverse diffusion.

The results above indicate that to suppress transverse transport in the interior, it is necessary to reduce the anisotropy between vertical transport and transverse transport. In practice, this can best be achieved by increasing the escape rate of well carriers. This can be seen by considering that transverse drift and diffusion can be characterized by an effective drift length $(L/L_E)\tilde{L}_{E_x}$, where $\tilde{L}_{E_x} = \tilde{\mu}_{nx}^i \tilde{\tau}_n^i \tilde{E}_x$, and $\tilde{E}_x = \hat{E}_x^{(1)}$ for drift and $\tilde{E}_x = KV_T$ for diffusion. For weak absorption, for example, the effective free-electron modulation is given in terms of the transit time, $t_{tr} = L/\tilde{\mu}_{nz}^i E_0$, as

$$\frac{\hat{n}_1}{n_0} = 1 - K(\tilde{\mu}_{nx} t_{tr} \tilde{E}_x) \quad (7-7)$$

This result indicates that the actual transverse transport length is determined by the transit time and not by the carrier lifetime. The transit time can be reduced by improving the well escape rates through the use of wells with lower barriers. This technique increases the

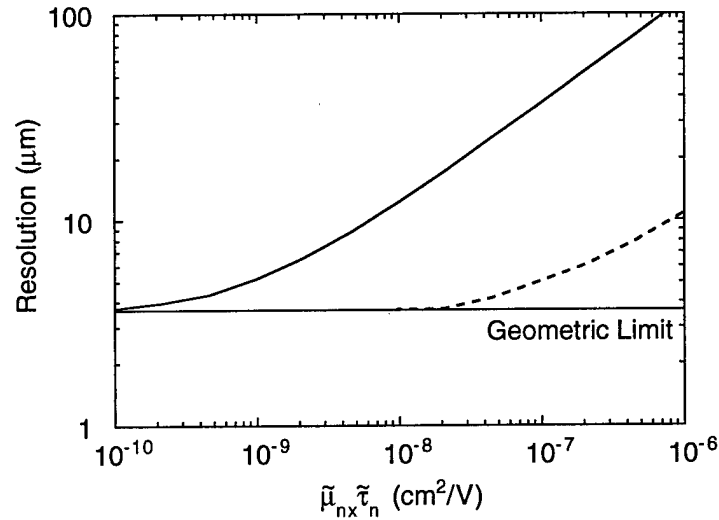


Figure 7-3 Resolution limits imposed by surface diffusion (dashed) and drift (solid) versus the effective transverse mobility-lifetime product of the free carriers in the surface-charge regions.

effective vertical mobility while actually weakly reducing the effective transverse mobility by suppressing the contribution of the typically larger well mobility, as seen in Eq. (6-19).

7.1.2 Surface Transport

Once injected into the surface-charge regions, the carriers drift and diffuse along the interfaces as described by Eq. (6-23). As in the interior, the phase of E_x causes carriers to drift into low intensity regions, reducing or even inverting the modulation. Unlike interior transport, however, there is no suppression of transverse transport due to fast vertical transport. Figure 7-3 shows the simulated resolution limit imposed by surface diffusion and drift as a function of the effective surface-carrier transverse mobility-lifetime product. Diffusion and especially drift significantly degrade the resolution. For typical, moderately doped material with $\tilde{\mu}_{nx}\tilde{\tau}_n = 1 \times 10^{-7} \text{ cm}^2/\text{V}$, the resolution performance is quite poor. To suppress transport at the interfaces, the transverse mobilities and/or the carrier lifetimes in the surface-charge regions must be reduced through such techniques as ion implantation or low temperature growth [29, 61, 63] which induce defects and create trapping centers. As in the interior, drift dominates for typical applied voltages. For the applied voltage

considered here, 20 V, the resolution limit imposed by carrier drift is over an order of magnitude larger than the resolution limit imposed by diffusion. The drift-limited response also degrades at higher applied voltages due to the increased transverse field.

Another important parameter to consider in addition to transverse mobility and carrier lifetime, when attempting to suppress transverse transport at the interfaces, is the width, w_s , of the high-density trap regions near the interfaces. In our analysis so far, we have taken this width to be wide enough, 50 nm, to accommodate the accumulated carriers. If the width of this region is made too small, then carriers will undergo transport along the interfaces with lifetimes given by the smaller, interior trap densities. These relatively long lifetimes could lead to significant transverse transport and degrade the resolution.

7.1.3 Resolution Estimates

An estimate of the resolution limits imposed by various transport mechanisms can be obtained by finding the grating spacing, Λ_{res} , at which the expressions for the carrier modulations at the start of the screening process, Eqs. (7-3), (7-5), and Eq. (6-23), vanish. These results are summarized in Table 7-1. Since only the initial applied field is used to estimate the carrier modulations, and the drift estimates are based on a simple field model, the absolute values predicted by these estimates do not agree completely with the numerical results which consider the full transient solution. The power law dependencies on the various transport parameters, however, do agree well with the results in Figs. 7-1, 7-2, and 7-3. For interior transport, the importance of the transport anisotropy is reflected in the dependence of the resolution limit on the ratio of the effective transverse to effective vertical mobilities. For surface transport, the resolution limits are essentially determined by the effective transverse mobility-lifetime product.

7.1.4 Intensity Modulation Dependence

The resolution curves shown in Figs. 7-1, 7-2, and 7-3 were all computed using the same value of the intensity modulation ratio, $m = 0.1$. The dependence of grating formation on

Transport Effect	Λ_{res}
Interior Diffusion	$2\pi L \sqrt{\frac{\tilde{\mu}_{nx}^i V_T}{\tilde{\mu}_{nz}^i E_0 L}}$
Interior Drift	$2\pi L \sqrt{\frac{\tilde{\mu}_{nx}^i}{\tilde{\mu}_{nz}^i}}$
Surface Diffusion	$2\pi \sqrt{\tilde{\mu}_{nx}^s \tilde{\tau}_n^s V_T}$
Surface Drift	$2\pi \sqrt{\tilde{\mu}_{nx}^s \tilde{\tau}_n^s E_0 L}$

Table 7-1 Estimated resolution limit, Λ_{res} , due to various transport effects. The diffusion estimates are for a constant field, E_0 . The drift estimates use a simple field model described in the text.

the intensity modulation was considered in the previous chapter, but only at long grating spacings. For the diffraction process to be truly linear, it is necessary that the grating amplitude depends linearly on the intensity modulation even at small grating spacings. To investigate the dependence of the grating amplitude on intensity modulation for various grating spacings, we computed resolution curves at $m = 0.1$ and $m = 1.0$ for a device with the following parameters: device structure as in Table 4-1, equal electron and hole parameters with an effective vertical mobility of $180 \text{ cm}^2/\text{V}\cdot\text{s}$, an effective transverse mobility of $2000 \text{ cm}^2/\text{V}\cdot\text{s}$, an effective interior lifetime of 1 ns , and an effective surface-region lifetime of 10 ps . The simulated resolution curves for $\hat{E}_z^{(1)}$ are shown in Fig. 7-4. The $m = 1.0$ curve actually shows slightly better resolution behavior (by about 23 %) than the $m = 0.1$ curve. This implies that the linearity of the grating formation process degrades slightly at smaller grating spacings.

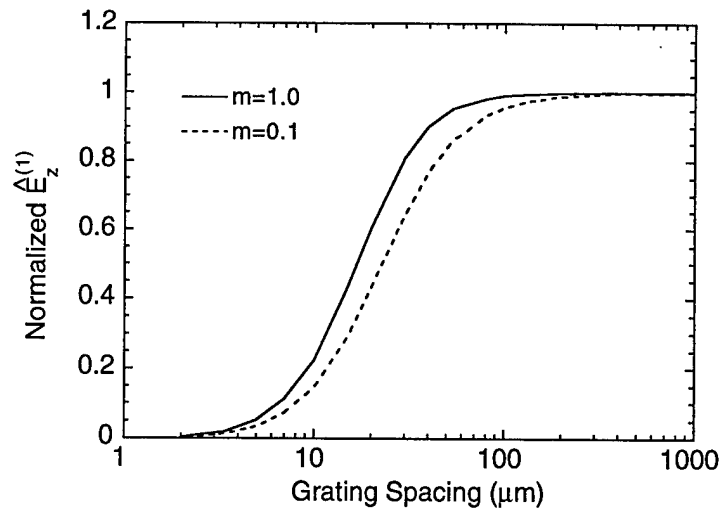


Figure 7-4 Resolution curve for the peak of the first-order field component. Each curve is normalized by its long grating spacing value for comparison. The $m = 1.0$ case has an approximately 23% better resolution limit than the $m = 0.1$ case.

7.2 Semiconductor and Quantum-Well Effects

As discussed in the previous chapter, there are a number of unique effects that occur in semiconductor materials and quantum well structures that can have a large impact on the vertical transport behavior. Since vertical transport plays an important role in determining the interior transport behavior, effects such as velocity saturation, resonant absorption, and field dependent carrier escape from the wells will also impact the resolution performance. The general impact of each of these effects can be considered within the framework of the small signal injection model.

The transit time for carrier drift is an important parameter in determining resolution. Any adverse effect on the transit time will impact the resolution performance. Velocity saturation and slow escape from quantum wells are two such effects. As discussed in Chapter 4, velocity saturation produces a field-dependent mobility that degrades at high fields. The resulting drift velocity saturates at a constant value and limits the transit time.

This means that increasing the applied voltage will not decrease the transit time and may actually degrade the resolution performance by increasing transverse drift.

The rate of carrier escape from the quantum wells has the opposite field dependence. For moderate electric fields, carrier escape from the wells is dominated by thermionic emission which, for electrons, is not very fast. Small escape rates produce poor effective vertical mobilities which increase the transit time. As the field is increased, however, the escape rates generally increase, which improves the vertical mobilities and reduces the transit time.

Velocity saturation and well-escape have a somewhat indirect, although very significant, effect on resolution performance. Resonant absorption, on the other hand, has a very direct influence on resolution performance. It was shown in Chapter 4 that resonant absorption essentially produces an effective generation rate for the zeroth-order carrier components that is reduced by the escape probability of a well-confined carrier. A similar analysis for the first-order component also produces an effective generation rate, given by

$$\tilde{g}_n^{(1)} = \left(\frac{\beta_N \tau_N}{1 + \beta_N \tau_N + \mu_N \tau_N V_T K^2} \right) \left(1 - \frac{\mu_N \tau_N K E_x^{(1)}}{1 + \beta_N \tau_N} \right) g_0 \quad (7-8)$$

For this component, the nominal generation rate is reduced by two factors. The first factor is essentially the escape probability, similar to the factor in the zeroth-order term. The second factor describes the reduction in the effective free-carrier generation rate due to photo-generated well-carriers transporting along the well before escaping. This reduced photogeneration rate for the first-order carrier components degrades the resolution performance by reducing the carrier modulation. This can be avoided by using non-resonant absorption. Non-resonant absorption prevents this reduction of the first-order photogeneration rate, as well as producing a larger zeroth-order generation rate and a larger absorption coefficient, both of which improve the screening rate.

$\mu_N = \mu_{nx} = 4000 \text{ cm}^2/\text{Vs}$	$\mu_P = \mu_{px} = 300 \text{ cm}^2/\text{Vs}$
$\mu_{nz} = \frac{\mu_{nz}^0}{1 + \mu_{nz}^0 E_z / v_{sat}^n}$	$\mu_{pz} = \frac{\mu_{pz}^0}{1 + \mu_{pz}^0 E_z / v_{sat}^p}$
$\mu_{nz}^0 = 4000 \text{ cm}^2/\text{Vs}$	$\mu_{pz}^0 = 300 \text{ cm}^2/\text{Vs}$
$v_{sat}^n = 1.0 \times 10^7 \text{ cm/s}$	$v_{sat}^p = 1.0 \times 10^7 \text{ cm/s}$
$\tau_n = 1 \text{ ps}$	$\tau_p = 1 \text{ ps}$
$s_2 = 3.2 \times 10^{-13} \text{ cm}^2/\text{V}^2$	$n_0 = 3.5$
$\lambda_0 = 850 \text{ nm}$	

Table 7-2 Carrier mobilities and other parameters used in the optimization example.

7.3 Optimization Example

To examine some of the semiconductor and quantum well effects mentioned previously, and to demonstrate the effectiveness of adjusting experimentally accessible parameters for optimization, we performed simulations for two different devices with parameters listed in Table 4-1 and Table 7-2. Both devices were similar except for differences in the quantum-well escape rates and carrier lifetimes in the surface-charge regions. The device labeled as ‘non-optimized’ used parameters typical of early fabricated devices [29], while the device labeled as ‘optimized’ used realistic device parameters to implement the optimization techniques described previously.

Grating formation was simulated for resonant absorption at an incident intensity of 10 mW/cm^2 with a zero bias absorption coefficient of $2 \times 10^4 \text{ cm}^{-1}$ and a quadratic QCSE absorption coefficient of $s_2 = 3.2 \times 10^{-13} \text{ cm}^2/\text{V}^2$. In the interior, the trapping time of well carriers into impurities was chosen to be 1 ns to place the optimized device into the long vertical drift length regime. This trapping time is easily achieved using moderate

doping [71]. A simple velocity saturation model was used for free-carrier vertical transport, and the values of the low field mobilities and saturated drift velocities were taken for bulk $\text{Al}_{0.1}\text{Ga}_{0.9}\text{As}$ [70]. Since drift velocity saturation for electrons occurs at relatively low fields, the important parameter in the velocity saturation model for resolution calculations is the saturated drift velocity, rather than the field dependence of the mobility. The simulations were performed for +20 V applied voltage at an intensity modulation of 0.1.

The thickness of the surface-charge regions was taken to be 50 nm to fully contain the carrier accumulation layers. In the non-optimized device, the effective carrier-lifetimes in the surface-charge regions were taken as 100 ps, which is appropriate for weakly semi-insulating material and clearly shows the effects of surface transport. The well escape rates in the non-optimized device were taken from the results presented in Chapter 3 for the 100 Å-GaAs/35 Å- $\text{Al}_{0.29}\text{Ga}_{0.71}\text{As}$ system. As shown in Fig. 3-9, the field dependent escape rates for this system are dominated by thermionic emission at low fields and by tunneling at high fields.

In the optimized device, the effective surface lifetimes were taken to be 1 ps, which can be achieved using low temperature growth [75]. The well escape rates for the optimized device were calculated using the Moss model for a shallow well system of 100 Å- $\text{Al}_{0.1}\text{Ga}_{0.9}\text{As}$ /100 Å- $\text{Al}_{0.16}\text{Ga}_{0.84}\text{As}$ which has been demonstrated to exhibit good electro-optic performance [54]. As discussed in Chapter 3, the resulting escape rates for this system are approximately $1 \times 10^{12} \text{ s}^{-1}$ for both electrons and holes.

The resolution curves for the peak value of the effective grating modulation, m_G , for both devices are shown in Fig. 7-5. The grating amplitude of the optimized device is approximately 50% larger than that of the non-optimized device. This is the result of using faster well-escape rates to increase the effective free-carrier vertical mobilities. The larger effective mobilities push the optimized device further into the long vertical drift length regime and increase the peak first-order field amplitude as shown, by example, in Fig. 6-3. The resolution performance of the optimized device is also dramatically improved, 7 μm compared to 35 μm for the non-optimized device.

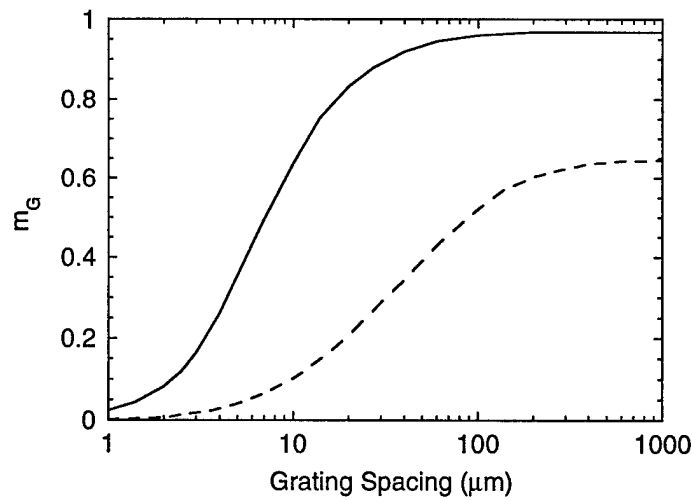


Figure 7-5 Grating spacing dependence of the effective grating modulation, m_G , for the non-optimized (dashed) and optimized (solid) devices described in the text. The optimized device displays a larger grating amplitude and better resolution.

A breakdown of the resolution limits imposed by the various transverse transport mechanisms is shown in Fig. 7-6. These resolution limits are obtained by finding the grating spacing that reduces the peak value of the effective grating modulation, m_G , to 50% of its value at long grating spacings (m_G is defined in Eq. (6-30)). These results are obtained by selectively suppressing all transverse transport mechanisms except the mechanism in question. For both devices, drift dominates the resolution limits, with interior drift slightly worse than surface drift. For the non-optimized device, the large transverse mobility-lifetime products in the surface-charge regions, $4 \times 10^{-7} \text{ cm}^2/\text{V}$ for electrons and $3 \times 10^{-8} \text{ cm}^2/\text{V}$ for holes, produces a large resolution limit. This effect is suppressed in the optimized device in which the corresponding surface-charge region mobility-lifetime products are $4 \times 10^{-9} \text{ cm}^2/\text{V}$ and $3 \times 10^{-10} \text{ cm}^2/\text{V}$.

For interior drift in the non-optimized device, velocity saturation and the relatively small well escape rate for electrons of $1 \times 10^{10} \text{ s}^{-1}$ for fields less than 50 kV/cm combine to produce an initial transit time of 1 ns. This relatively long transit time leads to significant transverse drift. In the optimized device, however, transverse drift is suppressed by a reduction of the transit times via larger effective free-carrier vertical mobilities. As

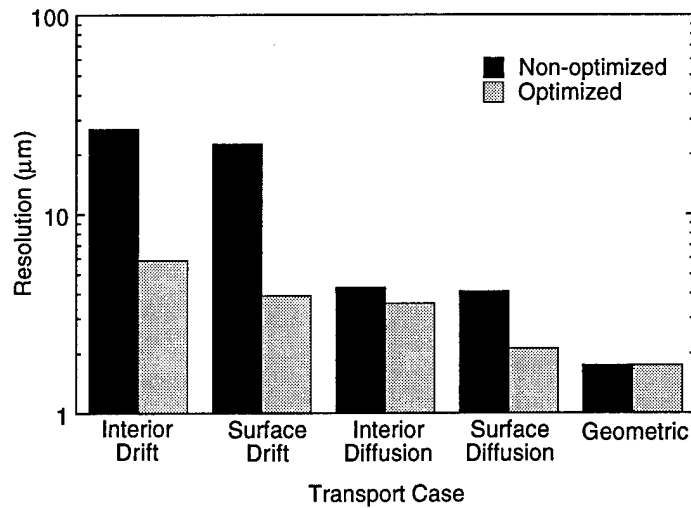


Figure 7-6 Comparison of the resolution limits obtained from m_G due to the indicated transport mechanisms. Drift clearly dominates the resolution limit in the non-optimized device, but is greatly suppressed in the optimized device.

indicated in Fig. 7-6, transverse diffusion plays only a minor role in determining the resolution performance, and, in the optimized case, its resolution limit is nearly suppressed below the geometric limit.

The results above indicate that resolution performance can be optimized while operating in the fast response regime. In fact, the speed response in the optimized device is quite good. The 10-90% rise times and fall times, obtained from the time dependence of m_G , are 11 μs and 12 μs , respectively.

7.4 Summary

When the first MQW-OASLM's were fabricated, conventional wisdom held that it was necessary to make the interior region strongly semi-insulating with short carrier lifetimes in order to suppress transverse drift and diffusion [6]. While this approach is certainly effective in suppressing transverse transport, it produces devices with slow response rates. In this chapter we have shown by device simulation that it is, in fact, possible to optimize both resolution and speed performance by designing devices with long carrier lifetimes

and shallow quantum wells in the interior, and by constraining the strongly semi-insulating material to regions near the semiconductor-insulator interfaces. An analysis of the transport mechanisms responsible for limiting the resolution showed that transverse drift was clearly the dominant effect. We found that extremely short-lifetime material in the surface-charge regions was required to suppress transverse drift at the interfaces, while shallow quantum wells in the interior were necessary to reduce the transit times and, consequently, transverse drift. Using realistic device parameters, resolutions down to 7 μm and frame rates of 100 kHz were obtained.

Chapter 8

Conclusions

Optical processing holds the promise of producing very high throughput computing systems by taking advantage of the inherent parallelism of optics. Fast, compact systems require high speed, high resolution optically addressed spatial light modulators to perform multiplication and other operations. In addition, a number of other device features such as convenient operating wavelength, low optical and electrical power, low applied voltage, and simple fabrication are required for any practical implementation. The multiple quantum well optical addressed spatial light modulators analyzed in this thesis exhibit many of these features. However, the realization of their full potential has been hampered by a lack of detailed understanding of device operation, and, specifically, of the role of quantum wells and vertical and transverse carrier transport in limiting device performance. The previous chapters have presented a number of modeling and experimental characterization results to address these issues.

8.1 Summary of Contributions

- A fully self-consistent, two-dimensional, drift-diffusion model that includes vertical and transverse quantum well transport, velocity saturation, field dependent carrier escape from quantum wells, and resonant absorption was developed to simulate transient grating formation in multiple quantum well optically addressed spatial light

modulators. Solutions to the transport equations were computed using analytical, simplified numerical, and full nonlinear numerical techniques.

- A combined analytical/simplified-numerical model of electric field screening was developed for uniform illumination conditions. This model established the surface-charge picture of field screening and allowed the calculation of the quasi-steady state carrier distributions. Two screening regimes were identified: dielectric relaxation (transport-limited) and saturated rate (photogeneration-limited). An estimate of the initial field screening rate was given, and device optimization techniques to obtain over 100 kHz frame rates at 10 mW/cm^2 intensity were discussed.
- A GaAs/AlGaAs MQW-OASLM was characterized under uniform illumination using optical transmission and photocurrent measurements. The photocurrent measurement was shown to be a more sensitive probe of the screening dynamics and demonstrated the transition between the saturated rate and dielectric relaxation regimes. The measured screening behavior agreed well with the predictions of the device model.
- A small signal model for small intensity modulations was developed to allow simplified numerical calculation of the transient grating formation and decay at large grating spacings. It was shown that long vertical transport lengths optimize the initial grating rise time, peak grating amplitude, and fall time. A discussion of the effect of field fringing from the surface-charge distributions on device resolution was also presented. A calculation of the quasi-steady state carrier distributions was given, including the impact of transverse transport in both the interior and surface-charge regions. Finally, the grating response at various intensity modulations was simulated. During the first half of grating formation for the first diffracted order, the dielectric grating produced by the QCSE was shown to display good linearity in the intensity modulation. Grating decay, however, was shown to be nonlinear in the intensity modulation.

- The role of transverse transport in limiting the resolution performance was investigated. Analytical estimates of the resolution limits imposed by drift and diffusion in the device interior and in the surface-charge regions were given. Simulations were used to calculate the resolution limits over a wide range of transport parameters, demonstrating that the resolution performance is dominated by transverse drift and can be improved via the optimization of the vertical transport behavior. An example of device optimization showed that both the resolution and frame rate can be optimized together. Resolutions down to 7 μm and frame rates up to 100 kHz at 10 mW/cm^2 intensity were obtained using experimentally accessible device parameters.

8.2 Suggestions for Future Research

There are several experimental and theoretical extensions and clarifications of the work presented in this thesis that would be quite useful to pursue. On the experimental side, the problem of leakage current in the photocurrent measurements presents some difficulty in interpreting the screening results. While the photocurrent measurements demonstrate good sensitivity to the screening dynamics, the initial transient and offset in the measurements present some problems in making direct comparison to modeling results. Since these problems appear to be sample dependent, a larger number of samples and better fabrication techniques should be investigated to see if these effects can be reduced.

An interesting project using the photocurrent measurement would be to compare the uniform illumination screening behavior of a sample with an interior bulk-like semiconductor region to the screening behavior produced by the MQW devices used in this work. While transmission measurements would be useless on a 2 μm bulk material, the photocurrent measurements could still be used to sort out some of the vertical transport effects such as field dependent carrier emission from the wells and velocity saturation.

On the theoretical side, there are a number of interesting issues that could be pursued. One issue which we briefly covered in this work was the intensity modulation dependence

of the grating response. Initial results indicated that the modulation dependence is rather weak, but this should be investigated over a wider range of operating conditions.

Another very important and interesting project would be the simulation of modified device designs. Recent fabrication efforts have examined the use of all-semiconductor structures to reduce fabrication complexity [80]. These devices typically involve heterostructure *p-i-n* diodes which should display device operation very similar to that described here. However, the presence of small bandgap barriers may lead to larger leakage currents and complicate device analysis and optimization. These devices could be modeled by including heterostructure regions in the device model presented in this thesis [81].

In addition to investigating new device designs, recent experimental efforts have examined device response under non-CW illumination conditions [82]. In particular, femtosecond short-pulse illumination has been used for device characterization and offers some possibilities for interesting applications [2]. Short-pulse screening could be straightforwardly simulated using the device model in this thesis by including the time dependence of the illumination pulse, or by starting the simulation with appropriate initial conditions on the carrier densities.

Finally, the 2D device model and solver that we have developed to simulate the MQW-OASLM could be applied to a wider range of quantum well devices such as hetero-n-i-p-i's and other modulators. Hetero-n-i-p-i's in particular display somewhat similar 2D transport behavior, and as of this date, no full 2D device simulation of their device operation has been performed.

Appendix A

Numerical Methods

The development of numerical methods to solve the semiconductor drift-diffusion transport equations has occurred primarily over the past 30 years, beginning with the first numerical simulation of a bipolar transistor by Gummel in 1964 [83]. The device model developed in this work required a two-dimensional, time-dependent solver capable of handling a set of tightly coupled, stiff equations and a wide variety of boundary conditions. To meet these requirements, several of the more successful techniques that have been developed by the device modeling community over the past several years were adopted. In this appendix, these techniques are summarized and some examples of typical computational grids and execution performance are presented. A very complete description of many of these techniques can be found in Pinto [64].

Any one of the drift-diffusion transport equations from Chapter 7 can be written in the general form

$$\frac{\partial n}{\partial t} + \nabla \cdot \mathbf{F} = U(\mathbf{x}, t) \quad (\text{A-1})$$

where n is some density, \mathbf{F} is some flux of that density, and U is some scalar source. In the case of the continuity equations, for example, n is the carrier concentration, \mathbf{F} is the current density, and U is the net generation and recombination rate. In the Poisson equation there is no time derivative, while in the trap rate equation there is no flux density.

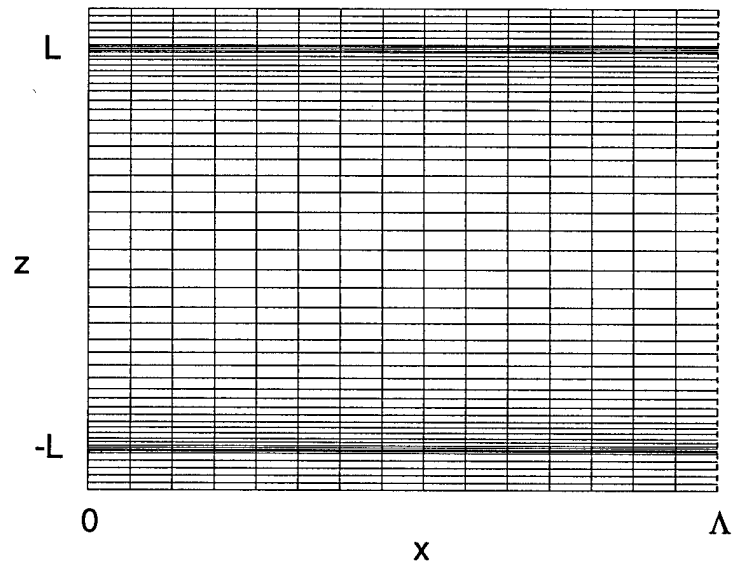


Figure A-1 Typical grid used in device simulations. The grid spacing along x is uniform, and periodic boundary conditions are used to wrap the dotted line, $x = \Lambda$, back to $x = 0$. The grid spacing along z is non-uniform to capture the carrier accumulation regions near $z = \pm L$.

To discretize Eq. (A-1), a spatial grid over the device area of interest must first be constructed. Under uniform illumination conditions, only a 1D grid along the growth direction is needed to simulate vertical transport. To simulate grating formation, a 2D grid is required in which one grating period with periodic boundary conditions is used. A typical grid used in the simulations presented in this work is shown in Fig. A-1. The grid is uniform in x but non-uniform in z to capture carrier accumulation near the interfaces at $z = \pm L$.

To discretize Eq. (A-1) onto a spatial grid, a variant of the finite difference method known as generalized box discretization was used [64]. This technique is essentially the application of Gauss' Law to Eq. (A-1) over a small region around each grid point. This method has a number of advantages over a direct finite difference approach [44], including inherent charge conservation and the straightforward treatment of periodic, Dirichlet, and Neumann boundary conditions. The local truncation error (LTE), or leading order error, in this approximation is second order in the grid spacing; this strikes a good balance between accuracy and complexity. In addition to box discretization, the Sharfetter-Gummel

formulation of the carrier currents was used [84]. This upwind approximation to the carrier currents produces a numerically stable solution even for large grid spacings.

Time discretization of Eq. (A-1) was performed using an implicit method. Explicit methods, while easier to implement, place a severe restriction on step size. Initially, a second order implicit method known as the trapezoidal rule (TR), or Crank-Nicholson, was implemented [44]. However, it produced unacceptable oscillations in the quasi-steady state regime due to the extreme stiffness of the transport equations. Better results were obtained using a hybrid method known as TRBDF2 which combines both the trapezoidal rule and a second order backward difference approximation (BDF2) [85]. In TRBDF2, each time step is subdivided into two smaller steps; TR is used for the first of these sub-steps, and then BDF2 is used to reach the end of the time step. This method has a number of advantages over straight TR, including good stability, suppression of oscillations near quasi-steady state, and a small LTE. It is also a one-step method which allows the simulation to be easily restarted from a given point in time.

For each time step, the discretization of the complete set of transport equations produces a nonlinear algebraic equation for each unknown at each grid point. To solve this nonlinear system, an iterative technique known as Gummel's method was implemented. This method attempts to solve each equation separately [83]. Each equation is solved in turn, and the process is repeated until the solution converges for all equations. Due to the tight coupling among the equations for our problem, however, this method gave poor convergence. Better performance was obtained by using a one-parameter damped Newton's method to solve the fully coupled nonlinear system [64]. Each iteration of the Newton algorithm requires the calculation, or approximation, of the Jacobian of the nonlinear system and a linear solve. In our implementation, the Jacobian was recomputed explicitly on each iteration, and the linear solve was performed using a sparse matrix package called SLAP which implemented an iterative biconjugate gradient method with incomplete LU preconditioning [86]. The convergence criterion was set using the relative change in the Newton updates to 10^{-5} , which is considered quite adequate [64]. Using these techniques, Newton convergence was usually achieved in only 3 or 4 iterations.

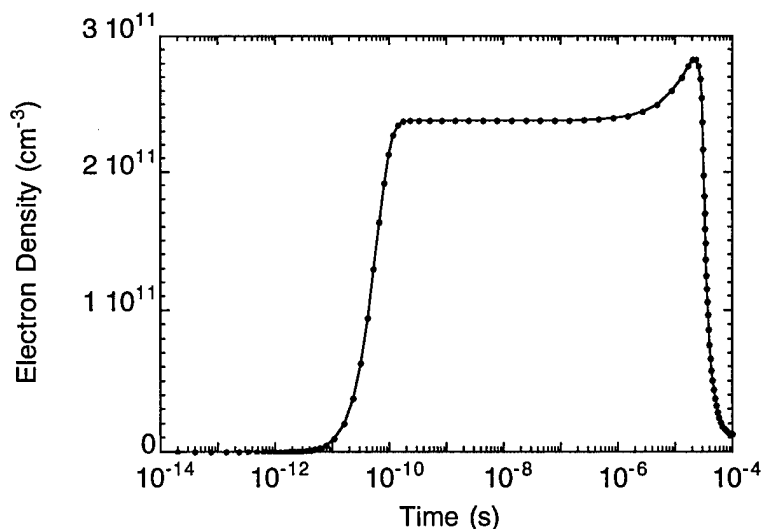


Figure A-2 Example of time steps determined via the adaptive time step control algorithm. The time steps follow the evolution of the electron density, starting with an initial time step of 20 fs and finishing with a time step of 20 μ s.

An important requirement for obtaining accurate results is the choice of appropriate spatial and temporal grids to faithfully follow the solution. For our case, a static spatial grid was quite satisfactory since most of the variation in the solution occurs at the semiconductor-insulator interfaces for both short and long times. The temporal evolution of the solution, however, follows several time scales, from carrier capture into the wells which is on the order of picoseconds, to the carrier lifetimes which are on the order of nanoseconds, as well as the screening time which is on the order of microseconds. To follow all these time scales accurately, an adaptive time step control algorithm based on the LTE of the electron continuity equation was implemented [64]. This algorithm uses an estimate of the LTE to choose a time step that will, in principle, bring the error to within a specified limit. While this algorithm does not guarantee that the actual error will be constrained, it worked well in practice and provided a convenient means of controlling the step size over many orders of magnitude. A typical set of time steps is shown in Fig. A-2. The time steps in this example follow the evolution of the electron density, varying 9 orders of magnitude from 20 fs up to 20 μ s.

Most of the simulations in this work were run on a Sun Microsystems SPARCstation20 rated at 25 Mflops. Typical execution times for the spatial and temporal grids shown previously were approximately 3 minutes for a 1D solution and approximately 1 hour for a 2D solution.

Appendix B

Publications

The majority of the work discussed in this dissertation has been presented in the following publications:

S. L. Smith and L. Hesselink, "Transport modeling of multiple-quantum-well optically addressed spatial light modulators," *J. Appl. Phys.*, submitted for publication.

S. L. Smith, L. Hesselink, and A. Partovi, "Electric field screening in a multiple-quantum-well optically addressed spatial light modulator," *Appl. Phys. Lett.* **68**, 3117 (1996).

S. L. Smith and L. Hesselink, "Analytical model for grating dynamics in surface-charge dominated Pockels readout optical modulator devices," *J. Opt. Soc. Am. B* **11**, 1878 (1994).

Bibliography

1. A. Partovi, A. M. Glass, T. H. Chiu, and D. T. H. Liu, "High-speed joint-transform optical image correlator using GaAs/AlGaAs semi-insulating multiple quantum wells and diode lasers," *Opt. Lett.* **18**, 906-908 (1993).
2. M. C. Nuss, M. Li, T. H. Chiu, A. M. Weiner, and A. Partovi, "Time-to-space mapping of femtosecond pulses," *Opt. Lett.* **19**, 664-666 (1994).
3. R. Jones, N. P. Barry, S. C. W. Hyde, J. C. Dainty, P. M. W. French, K. M. Kwolek, D. D. Nolte, and M. R. Melloch, "Real-time depth resolved holographic imaging using photorefractive MQW devices," *Conference on Lasers and Electro-optics Technical Digest*, 188-189 (1996).
4. S. L. Hou and D. S. Oliver, "Pockels readout optical memory using $\text{Bi}_{12}\text{SiO}_{20}$," *Appl. Phys. Lett.* **18**, 325-328 (1971).
5. T. D. Beard, W. P. Bleha, and S.-Y Wong, "ac liquid-crystal light valve," *Appl. Phys. Lett.* **22**, 90-92 (1972).
6. A. Partovi, A. M. Glass, D. H. Olson, G. J. Zydzik, K. T. Short, R. D. Feldman, and R. F. Austin, "High sensitivity optical image processing device based on CdZnTe/ZnTe multiple quantum well structures," *Appl. Phys. Lett.* **59**, 1832-1834 (1991).

7. W. R. Roach, "Resolution of electrooptic light valves," *IEEE Trans. Electron Devices* **ED-21**, 453-459 (1974).
8. Y. Owechko and A. R. Tanguay, Jr., "Theoretical resolution limitations of electro-optic spatial light modulators. I. Fundamental considerations," *J. Opt. Soc. Am. A* **1**, 635-643 (1984).
9. R. A. Sprague, "Effect of bulk carriers on PROM sensitivity," *J. Appl. Phys.* **46**, 1673-1678 (1975).
10. J. Chen and T. Minemoto, "Numerical analysis of the modulation transfer function of a Pockels readout optical modulator," *J. Opt. Soc. Am. A* **6**, 1281-1291 (1989).
11. A. Partovi and E. M. Garmire, "Band-edge photorefractivity in semiconductors: Theory and experiment," *J. Appl. Phys.* **69**, 6885-6898 (1991).
12. D. A. B. Miller, D. S. Chemla, T. C. Damen, A. C. Gossard, W. Wiegman, T. H. Wood, and C. A. Burrus, "Novel hybrid optically bistable switch: The quantum well self-electro-optic effect device," *Appl. Phys. Lett.* **45**, 13-15 (1984).
13. D. A. B. Miller, D. S. Chemla, T. C. Damen, A. C. Gossard, W. Wiegmann, T. H. Wood, and C. A. Burrus, "Electric field dependence of optical absorption near the band gap of quantum-well structures," *Phys. Rev. B* **32**, 1043-1060 (1985).
14. D. D. Nolte, "Resolution of electro-optic spatial light modulators: the role of lateral transport," *Opt. Comm.* **92**, 199-204 (1992).
15. D. D. Nolte, in *Photorefractive Effects and Materials*, edited by D. D. Nolte (Klewer, Boston, 1995), Chap. 7.
16. L. Wang and G. Moddel, "Resolution limits from charge transport in optically addressed spatial light modulators," *J. Appl. Phys.* **78**, 6923-6935 (1995).

17. H. Fujikake, K. Takizawa, H. Kikuchi, J. Hirose, T. Kobayashi, and T. Matsumoto, "Infrared- and Visible-Light-Sensitive Spatial Light Modulator Using Pigment-Dispersed Organic Photoconductor," *Jap. J. Appl. Phys, Part 1* **34**, 4067-4072 (1995).
18. H. Iman, L. R. Linvold, and P. S. Ramanujam, "Photoanisotropic incoherent-to-coherent converter using a bacteriorhodopsin thin film," *Opt. Lett.* **20**, 225-227 (1995).
19. I. Biaggio, B. Ai, R. J. Knize, J. P. Partanen, and R. W. Hellwarth, "Optical correlator that uses cesium vapor," *Opt. Lett.* **19**, 1765-1767 (1994).
20. U. Efron, Ed. *Spatial Light Modulator Technology: Materials, Devices, and Applications* (Marcel Dekker, New York, 1995).
21. D. Armitage, J. I. Thackara, and W. D. Eades, "Photoaddressed liquid crystal spatial light modulators," *Appl. Opt.* **28**, 4763-4771 (1989).
22. W. Li, R. A. Rice, G. Moddel, L. A. Pagano-Stauffer, and M. A. Handschy, "Hydrogenated Amorphous-Silicon Photosensor for Optically Addressed High-Speed Spatial Light Modulator," *IEEE Trans. Electron Devices* **ED-36**, 2959-2964 (1989).
23. B. A. Horwitz and F. J. Corbett, "The PROM- Theory and Applications for the Pockels Readout Optical Modulator," *Opt. Eng.* **17**, 353-364 (1978).
24. D. A. B. Miller, "Quantum wells for optical information processing," *Opt. Eng.* **26**, 368-372 (1987).
25. A. L. Lentine, F. B. McCormick, R. A. Novotny, L. M. F. Chirovsky, L. A. D'asaro, R. F. Kopf, J. M. Kuo, G. D. Boyd, "A 2kbit Array of Self-Electrooptic Effect Devices," *Photonics Tech. Lett.* **2**, 51-53 (1990).

26. G. H. Döhler, "Doping Superlattices ("n-i-p-i Crystals")," *IEEE J. Quantum Electron.* **QE-22**, 1682-1695 (1986).
27. A. Kost, "Performance characteristics of hetero-nipi structures," *Opt. and Quant. Electr.* **22**, S187-S200 (1990).
28. D. Mahgerefteh and E. Garmire, "Band-transport model for field screening in multiple-quantum-well hetero-n-i-p-i's," *Opt. Lett.* **18**, 616-618 (1993).
29. A. Partovi, A. M. Glass, D. H. Olson, G. J. Zydzik, H. M. O'Bryan, T. H. Chiu, and W. H. Knox, "Cr-doped GaAs/AlGaAs semi-insulating multiple quantum well photorefractive devices," *Appl. Phys. Lett.* **62**, 464-466 (1993).
30. J. W. Goodman, *Introduction to Fourier Optics* (McGraw-Hill, New York, 1968).
31. A. Yariv and P. Yeh, *Optical Waves in Crystals* (John Wiley & Sons, New York, 1984).
32. A. D. Fisher, "Spatial light modulators: functional capabilities, applications, and devices," *Int. J. Optoelectron.* **5**, 125-167 (1990).
33. A. Vander Lugt, "Signal Detection By Complex Spatial Filtering," *IEEE Trans. Inf. Theory* **IT-10**, 139-145 (1964).
34. D. Williams, S. G. Latham, C. M. J. Powles, M. A. Powell, R. C. Chittick, A. P. Sparks, and N. Collings, "An amorphous silicon/chiral smectic spatial light modulator," *J. Phys. D: Appl. Phys.* **21**, S156-159 (1988).
35. P. Gunter and J. -P. Huignard, Eds., *Photorefractive Materials and Their Applications I: Fundamental Phenomena*, Chapter 7 (Springer-Verlag, Berlin, 1988).
36. G. Bastard, *Wave Mechanics Applied to Semiconductor Heterostructures* (Halsted Press, New York, 1988).

37. C. Kittel, *Introduction to Solid State Physics* (John Wiley & Sons, New York, 1986).
38. A. Cho, ed., *Molecular Beam Epitaxy* (American Institute of Physics, Woodbury, New York, 1994).
39. M. Razeghi, *The MOCVD Challenge: Volume 1: A Survey of GaInAsP-InP for Photonic and Electronic Applications* (IOP Publishing, Bristol, 1989).
40. D. J. Moss, T. Ido, and H. Sano, "Calculation of Photogenerated Carrier Escape Rates from GaAs/Al_xGa_{1-x}As Quantum Wells," *IEEE J. Quantum Electron.* **QE-30**, 1015-1026 (1994).
41. G. Bastard, E. E. Mendez, L. L. Chang, and L. Esaki, "Variational calculations on a quantum well in an electric field," *Phys. Rev. B* **28**, 3241-3245 (1983).
42. A. Harwit, J. S. Harris, Jr., and A. Kapitulnik, "Calculated quasi-eigenstates and quasi-eigenenergies of quantum well superlattices in an applied electric field," *J. Appl. Phys.* **60**, 3211-3213 (1986).
43. A. Ghatak, K. Thyagarajan, and M. R. Shenoy, "Novel Numerical Technique for Solving the One-Dimensional Schroedinger Equation Using Matrix Approach-Application to Quantum Well Structures," *IEEE J. Quantum Electron.* **QE-24**, 1524-1531 (1988).
44. S. Selberherr, *Analysis and Simulation of Semiconductor Devices* (Springer Verlag, Wien, 1984).
45. J. Y. Tang, "Two-Dimensional Simulation of MODFET and GaAs Gate Heterojunction FET's," *IEEE Trans. Electron Devices* **ED-32**, 1817-1823 (1985).
46. Q. Wang, R. M. Brubaker, D. D. Nolte, M. R. Melloch, "Photorefractive quantum wells: transverse Franz-Keldysh geometry," *J. Opt. Soc. Am. B* **9**, 1626-1641 (1992).

47. B. Deveaud, J. Shah, T. C. Damen, B. Lambert, A. Chomette, and A. Regreny, "Optical Studies of Perpendicular Transport in Semiconductor Superlattices," *IEEE J. Quantum Electron.* **QE-24**, 1641-1651 (1988).
48. T. Weil and B. Vinter, "Calculation of phonon-assisted tunneling between two quantum wells," *J. Appl. Phys.* **60**, 3227-3231 (1986).
49. R. F. Kazarinov and R. A. Suris, "Electric and Electromagnetic Properties of Semiconductors with a Superlattice," *Sov. Phys.-Semi.* **6**, 120-131 (1971).
50. A. M. Fox, D. A. B. Miller, G. Livescu, J. E. Cunningham, and W. Y. Jan, "Quantum Well Carrier Sweep Out: Relation to Electroabsorption and Exciton Saturation," *IEEE J. Quantum Electron.* **QE-27**, 2281-2295 (1991).
51. H. Schneider and K. v. Klitzing, "Thermionic emission and Gaussian transport of holes in a GaAs/Al_xGa_{1-x}As multiple-quantum-well structure," *Phys. Rev. B* **38**, 6160-6165 (1988).
52. J. A. Cavailles, D. A. B. Miller, J. E. Cunningham, P. L. K. Wa, and A. Miller, "Simultaneous Measurements of Electron and Hole Sweep-Out from Quantum Wells and Modeling of Photoinduced Field Screening Dynamics," *IEEE J. Quantum Electron.* **QE-28**, 2486-2497 (1992).
53. S. Gasiorowicz, *Quantum Physics* (John Wiley & Sons, New York, 1974).
54. I. Lahiri, M. Aguilar, D. D. Nolte, and M. R. Melloch, "High-efficiency Stark-geometry photorefractive quantum wells with intrinsic cladding layers," *Appl. Phys. Lett.* **68**, 517-519 (1996).
55. R. S. Muller and T. I. Kamins, *Device Electronics for Integrated Circuits*, 2nd ed. (John Wiley & Sons, New York, 1986).

56. N. Debbar and P. Bhattacharya, "Carrier dynamics in quantum wells behaving as giant traps," *J. Appl. Phys.* **62**, 3845-3847 (1987).
57. D. C. Hutchings, C. B. Park, and A. Miller, "Modeling of cross-well carrier transport in a multiple-quantum-well modulator," *Appl. Phys. Lett.* **59**, 3009-3011 (1991).
58. L. Thibaudeau and B. Vinter, "Phonon-assisted carrier capture into a quantum well in an electric field," *Appl. Phys. Lett.* **65**, 2039-2041 (1994).
59. B. Deveaud, J. Shah, T. C. Damen, and W. T. Tsang, "Capture of electrons and holes in quantum wells," *Appl. Phys. Lett.* **52**, 1886-1888 (1988).
60. C. S. Kyono, K. Ikossi-Anastasiou, W. S. Rabinovich, D. S. Katzer, and A.J. Tsao, "GaAs/AlGaAs multiquantum well resonant photorefractive devices fabricated using epitaxial lift-off," *Appl. Phys. Lett.* **64**, 2244-2246 (1994).
61. S. R. Bowman, W. S. Rabinovich, C. S. Kyono, D. S. Katzer, and K. Ikossi-Anastasiou, "High-resolution spatial light modulators using GaAs/AlGaAs multiple quantum wells," *Appl. Phys. Lett.* **65**, 956-958 (1994).
62. W. S. Rabinovich, S. R. Bowman, D. S. Katzer, and C. S. Kyono, "Intrinsic multiple quantum well spatial light modulators," *Appl. Phys. Lett.* **66**, 1044-1046 (1995).
63. A. Partovi, A. M. Glass, D. H. Olson, G. J. Zydzik, K. T. Short, R. D. Feldman, and R. F. Austin, "High-speed photodiffractive effect in semi-insulating CdZnTe/ZnTe multiple quantum wells," *Opt. Lett.* **17**, 655-657 (1992).
64. M. Pinto, *Comprehensive semiconductor device simulation for silicon ULSI*, PhD dissertation (Stanford University, 1990).
65. A. M. Fox, R. G. Ispasoiu, C. T. Foxon, J. E. Cunningham, and W. Y. Jan, "Carrier escape mechanisms from GaAs/Al_xGa_{1-x}As multiple quantum wells in an electric field," *Appl. Phys. Lett.* **63**, 2917-2919 (1993).

66. S. M. Sze, *Physics of Semiconductor Devices* (Wiley, New York, 1981).
67. J. Mort and D. M. Pai, eds., *Photoconductivity and Related Phenomena* (Elsevier, Amsterdam, 1976).
68. T. S. Hall, R. Jaura, L. M. Connors, and P. D. Foote, "The photorefractive effect- a review," *Prog. Quantum Electron.* **10**, 77-146 (1985).
69. C.M. Bender and S. A. Orszag, *Advanced Mathematical Methods for Scientists and Engineers* (McGraw-Hill, New York, 1978).
70. S. Adachi, *Properties of Aluminum Gallium Arsenide* (INSPEC, London, 1993).
71. D. Mahgerefteh, E. Canoglu, C.-M. Yang, E. Garmire, A. Partovi, T. H. Chiu, A. M. Glass, and G. J. Zyzik, "Picosecond response of a Cr-doped GaAs/AlGaAs semi-insulating multiple-quantum-well photorefractive device," *Conference on Lasers and Electro-optics Technical Digest*, 269-270 (1994).
72. R. P. Leavitt, J. L. Bradshaw, J. T. Pham, and M. S. Tobin, "Quantitative model for photocurrent spectroscopy of quantum-well diodes including transit-time and background-doping effects," *J. Appl. Phys.* **75**, 2215-2226 (1994).
73. T. H. Wood, J. Z. Pastalan, C. Burrus, Jr., B. C. Johnson, B. I. Miller, J. S. deMiguel, U. Koren, and M. G. Young, "Electric field screening by photogenerated holes in multiple quantum wells: A new mechanism for absorption saturation," *Appl. Phys. Lett.* **57**, 1081-1083 (1990).
74. G. D. Boyd, A. M. Fox, D. A. B. Miller, L. M. F. Chirovsky, L. A. D'Asaro, J. M. Kuo, R. F. Lopf, and A. L. Lentine, "33 ps optical switching of symmetric self-electro-optic effect devices," *Appl. Phys. Lett.* **57**, 1843-1845 (1990).
75. G. L. Witt, "LTMBE GaAs: present status and perspectives," *Materials Science and Engineering* **B22**, 9-15 (1993).

76. C. M. Hurd and W. R. McKinnon, "Modeling the behavior of photogenerated charge in semi-insulating GaAs," *J. Appl. Phys.* **75**, 596-603 (1994).
77. A. Fraenkel, E. Finkman, S. Maimon, and G. Bahir, "Vertical drift mobility of excited carriers in multi quantum well structures," *J. Appl. Phys.* **75**, 3536-3543 (1994).
78. S. Nojima and K. Wakita, "Optimization of quantum well materials and structures for excitonic electroabsorption and effects," *Appl. Phys. Lett.* **53**, 1958-1960 (1988).
79. D. D. Nolte and K. M. Kwolek, "Diffraction from a short-cavity Fabry-Perot: application to photorefractive quantum wells," *Opt. Comm.* **115**, 606-616 (1995).
80. I. Lahiri, K. M. Kwolek, D. D. Nolte, and M. R. Melloch, "Photorefractive p-i-n diode quantum well spatial light modulators," *Appl. Phys. Lett.* **67**, 1408-1410 (1995).
81. M. S. Lundstrom and R. J. Schuelke, "Numerical Analysis of Heterostructure Semiconductor Devices," *IEEE Trans. Electron Devices* **ED-30**, 1151-1159 (1983).
82. E. Canoglu, C. Yang, E. Garmire, D. Mahgerefteh, A. Partovi, T. H. Chiu, and G. J. Zydzik, "Carrier transport in a photorefractive multiple quantum well device," *Appl. Phys. Lett.* **69**, 316 (1996).
83. H. K. Gummel, "A self-consistent iterative scheme for one-dimensional steady state transistor calculations," *IEEE Trans. Electron Devices* **ED-11**, 455 (1964).
84. D. L. Scharfetter and H. K. Gummel, "Large-signal analysis of a silicon Read diode oscillator," *IEEE Trans. Electron Devices* **ED-16**, 66 (1969).
85. R. E. Bank, W. M. Coughran, Jr., W. Fichtner, E. H. Grosse, D. J. Rose, and R. K. Smith, "Transient simulation of silicon devices and circuits," *IEEE Trans. Electron Devices* **ED-32**, 1992 (1985).

86. A. Greenbaum and M. K. Seager, *SLAP: Sparse Linear Algebra Package*, (Lawrence Livermore National Laboratory, Livermore, CA, 1989).